博士論文

Study on Distributed Anisotropic Metamaterials for Transformation Electromagnetics

変換電磁気学のための分布定数異方性メタマテリアルに関する研究

March 2016

Tsutomu Nagayama

Graduate School of Science and Engineering,
Yamaguchi University

Table of Contents

Chapter 1 Introduction

1.1 Concept of Metamaterials

Metamaterials [1]–[63] are artificially constructed materials composed of sub-wavelength constituents. By determining material kinds, shapes, and arrangements of unit cells, metamaterials can exhibit unique properties that the original materials do not exhibit. Moreover, metamaterials can also exhibit electric or magnetic properties that conventional natural materials do not exhibit. For example, it is possible to realize negative refractive index materials [1], [5]–[24], cloaks of invisibility [27]–[55], illusion media mimicking scattered waves by arbitral objects [56]–[63], and the like with metamaterials.

In order to design metamaterials, we first need to select the material kinds for their constituents. Possible materials can be metals, dielectrics, magnetic materials, or any materials available. Secondly, in order to obtain unique properties, we need to determine the unit cell topology. As the unit cell, for example, spheres [7], wires [2], [3], [6], split-rings [4], [6], [22], and mushrooms [16], [20] shown in Figs. 1.1(a)–(d) have been proposed. For the cases with spheres and wires shown in Figs. 1.1(a) and (b), respectively, it is shown that the materials exhibit dielectric properties. For the case with split-rings shown in Fig. 1.1(c), the materials exhibit magnetic properties. In addition, for the case with mushrooms shown in Fig. 1.1(d), the materials show negative refractive index properties. Then, we determine arrangements the unit cells. The arrangement may be random as shown in Fig. 1.2(a), or we can control the band structures by arranging the unit cells periodically as shown in Fig. 1.2(b). Even with asymmetric unit cells, anisotropy and isotropy can be controlled by arrangements as

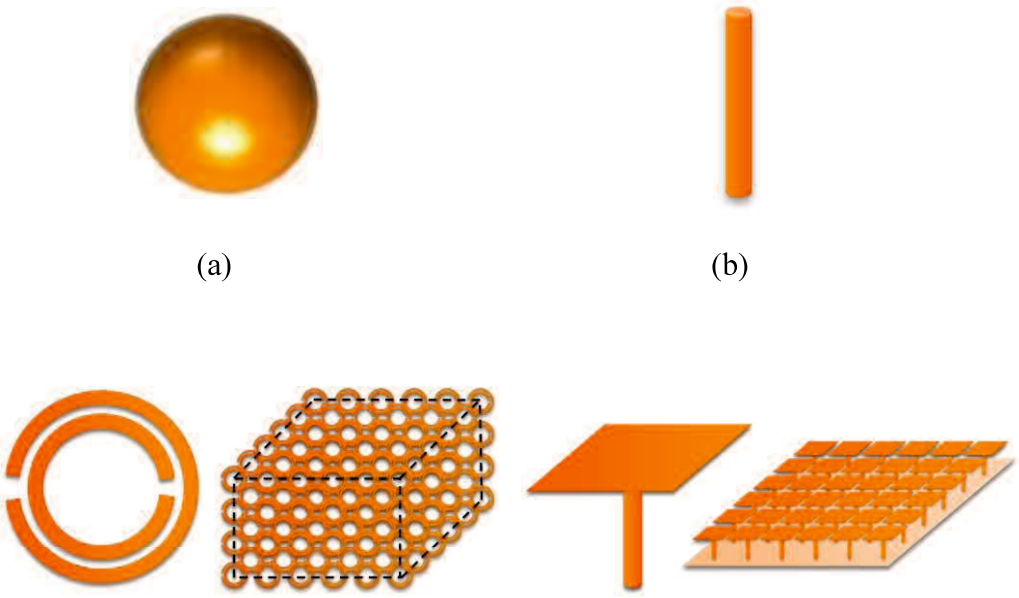

Fig. 1.1 Unit cells for metamaterials. (a) Sphere. (b) Wire. (c) Split-ring. (d) Mushroom.

shown in Fig. 1.3(a) and (b). In addition, inhomogeneity can be controlled with the arrangement as shown in Fig. 1.3(c).

By designing metamaterials according to the above manners, we can realize values of the relative permeability μ_r and permittivity ε_r which natural materials do not have. Fig. 1.4 shows μ_r and ε_r values on a μ_r–ε_r plane which metamaterials and natural materials (optical materials) can realize. For example, natural optical materials can take μ_r and ε_r values on the line shown in Fig. 1.4. In contrast, metamaterials can potentially realize any values on the plane with frequency dispersion controls. Moreover, we might be able to freely control all the μ and ε tensors components in the following constitutive relations including ζ and ξ tensors of the magnetoelectric effect:

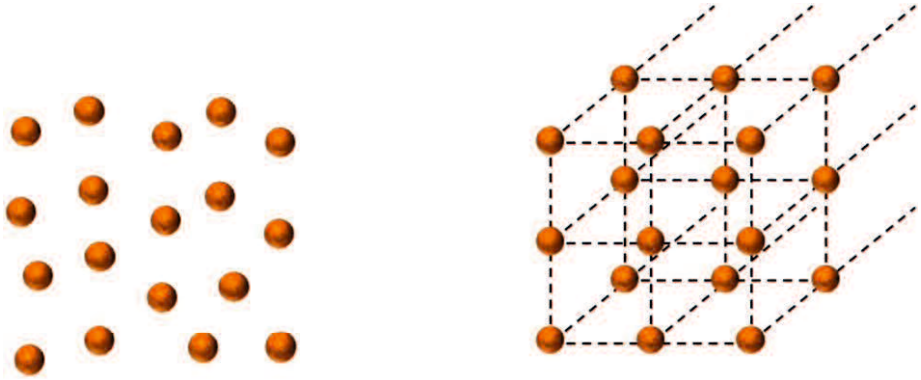

(a) (b)

Fig. 1.2 Arrangements of unit cells. (a) Random arrangement. (b) Periodical arrangement.

$$\begin{aligned} \boldsymbol{B} &= \bar{\mu}\boldsymbol{H} + \bar{\zeta}\boldsymbol{E} \\ &= \begin{pmatrix} \mu_{xx} & \mu_{xy} & \mu_{xz} \\ \mu_{yx} & \mu_{yy} & \mu_{yz} \\ \mu_{zx} & \mu_{zy} & \mu_{zz} \end{pmatrix} \boldsymbol{H} + \begin{pmatrix} \zeta_{xx} & \zeta_{xy} & \zeta_{xz} \\ \zeta_{yx} & \zeta_{yy} & \zeta_{yz} \\ \zeta_{zx} & \zeta_{zy} & \zeta_{zz} \end{pmatrix} \boldsymbol{E} \end{aligned} \tag{1.1}$$

$$\begin{aligned} \boldsymbol{D} &= \bar{\varepsilon}\boldsymbol{E} + \bar{\xi}\boldsymbol{H} \\ &= \begin{pmatrix} \varepsilon_{xx} & \varepsilon_{xy} & \varepsilon_{xz} \\ \varepsilon_{yx} & \varepsilon_{yy} & \varepsilon_{yz} \\ \varepsilon_{zx} & \varepsilon_{zy} & \varepsilon_{zz} \end{pmatrix} \boldsymbol{E} + \begin{pmatrix} \xi_{xx} & \xi_{xy} & \xi_{xz} \\ \xi_{yx} & \xi_{yy} & \xi_{yz} \\ \xi_{zx} & \xi_{zy} & \xi_{zz} \end{pmatrix} \boldsymbol{H}, \end{aligned} \tag{1.2}$$

where $\boldsymbol{B}$, $\boldsymbol{H}$, $\boldsymbol{D}$, and $\boldsymbol{E}$ are the magnetic flux density, the magnetic field, the electric flux density, and the electric field, respectively. Controlling all the elements of μ, ε, ζ, and ξ tensors would be an ultimate goal of metamaterial researches.

(a) (b) (c)

Fig. 1.3 Arrangements of unit elements for metamaterials. (a) Anisotropy by periodical arrangement of asymmetric unit cells. (b) Isotropy by random arrangement of the asymmetric unit cells. (c) Inhomogeneity by ununiform arrangement.

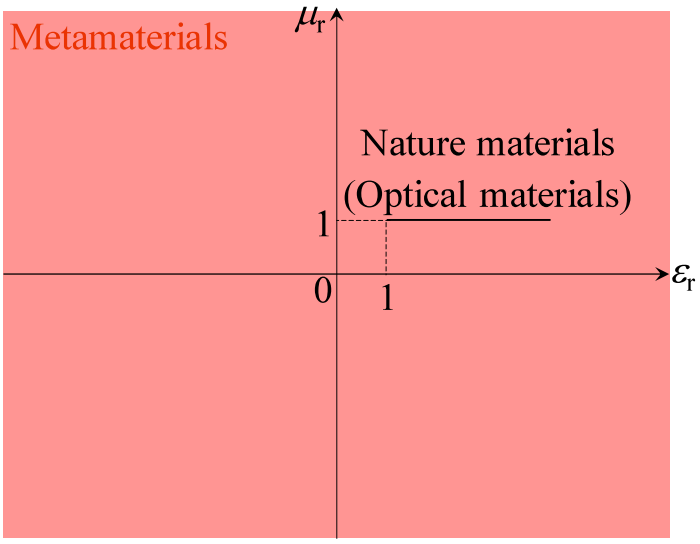

Fig. 1.4 Relative permeability μ_r and permittivity ε_r plane which can be realized with metamaterials or nature materials (optical materials).

1.2 History of Metamaterials and Transformation Electromagnetics

The concept of the negative refractive index media has been proposed in 1968 by V. G. Veselago [1], a physicist in the Soviet Union. However, the negative refractive index media have not been realized during about thirty years after 1968. In 2000, the negative refractive index have been demonstrated by D. R. Smith, a physicist in U.S.A., at microwave frequencies with a left-handed metamaterial [6] composed of metal wires [2], [3] and split-ring resonators [4]. Since 2000, various studies on metamaterials have been carried out extensively. In 2002, transmission-line metamaterials for the left-handed materials have been proposed by three individual researchers, T. Itoh, A. A. Oliner, and and G. V. Eleftheriades [8]–[10], based on the circuit theory. Besides, in 2004, the CRLH transmission-line model has been proposed by A. Sanada [16] as a generalized transmission-line left-handed metamaterials. These theories are deeply related to this research. After 2004, metamaterials have been studied even at higher frequencies [22], [23], or for practical applications [26].

In 2006, the concept of transformation electromagnetics has been proposed by J. B. Pendry [27], [28], a physicist in U. K., and a cloak of invisibility has been first implemented and demonstrated with split-ring resonators by D. R. Smith at microwave frequencies [29]. Since 2006, various studies on cloaks of invisibility based on transformation electromagnetics have been carried out extensively. In 2008, the concept of carpet cloaks, which are a kind of cloaks of invisibility, has been proposed by J. B. Pendry [31]. In 2009, a non-resonant carpet cloak has been implemented and demonstrated by X. Zhang at optical frequencies [32]. Thereafter, in addition to cloaks

of invisibility based on transformation electromagnetics [30], [33]–[44], surface cloaks [45]–[50] and other kinds of cloaks [51]–[55] have also been studied. Besides, applications to illusion media mimicking scattered waves by arbitrary objects [56]–[63] have been proposed.

In the following, the concept of transformation electromagnetics with additional histories is described in detail.

1.3 Concept of Transformation Electromagnetics

In the theory of general relativity, it has been shown that Maxwell's equations are invariant with coordinate transformations and rays of electromagnetic waves or lights are bent by gravity. On the other hands, Maxwell's equations can be invariant for arbitrary coordinate transformations with appropriate tensor transformation for the constitutive relations [28], in other words, arbitrary coordinate transformations can be realized by special materials with highly controlled constitutive parameters [27], [28], [31]. This concept is referred to as the material interpretation of coordinate transformations [27], [28], [31]. With the concept, high controllability of electromagnetic waves with enormously larger degrees of freedom is expected compared with conventional methods using mirrors, lenses, and the like. This whole concept of controlling electromagnetic fields based on the material interpretation of coordinate transformations is referred to as the *transformation electromagnetics* or *transformation optics* [27], [28], [31]. With this concept, for example, there are possibilities of realizing novel electromagnetic or optical materials such as cloaks of invisibility [27]–[44], illusion media mimicking scattered waves by arbitral objects [56]–[69], and the like. In order to realize these materials based on the transformation

electromagnetics, anisotropy and inhomogeneity of permeability and permittivity tensors have to be highly controlled. These controls cannot be realized with conventional natural materials, however, this can be realized by artificially constructed metamaterials.

Studies on realization of cloaks of invisibility or illusion media based on transformation electromagnetics [27]–[44], [56]–[63], surface cloak [45]–[50], and the like [51]–[55] have been carried out extensively. For example, a cylindrical cloak of invisibility, which is a medium for bending incident waves and hiding objects, has been first implemented with split-ring resonators and has been demonstrated experimentally at microwave frequencies [29]. However, its operation bandwidth is narrow and the loss is very high due to resonant properties of the split-ring resonators. On the other hand, non-resonant carpet cloaks of invisibility [31]–[38] have been proposed to overcome the disadvantages. The carpet cloaks of invisibility are media hiding objects under the carpet and mimicking a flat floor. Especially in 2009, by X. Zhang, a typical carpet cloak of invisibility has been implemented on a silicon substrate with cylindrical holes controlling the effective refractive indexes and its wideband and low-loss characteristics have been successfully demonstrated [32]. However, the implementation method is limited to cloaks based on quasi-conformal coordinate transformations [31]–[38] since the off-diagonal components of the permittivity tensor cannot be controlled essentially by the implementation method. As a result, the carpet cloak can hide only small objects comparable with the wavelength with negligible off-diagonal components of the permittivity tensor. Full controllability of anisotropy including the off-diagonal tensor components as well as wideband and low-loss properties are required to realize cloaks of invisibility based on transformation electromagnetics in general with non-conformal

coordinate transformation.

Table 1.1 summarizes features of the conventional cloak structures with a non-resonant type structure proposed in this research. So far, cloak structures which fulfill all the requirements of control of anisotropy, wideband property, and low-loss property have not been realized. Especially, for practical applications, it is important to simultaneously solve the problems. In this research, a novel metamaterial is proposed to control anisotropy including the off-diagonal tensor components and realize wideband and low-loss properties simultaneously based on the transmission-line approach. Rigorous design formulas are given theoretically based on an equivalent circuit. This

Table 1.1 Features of conventional cloaks and the proposed cloak in this research.

	Type of operation	Control of anisotropy	Wideband property	Low-loss property
D. R. Smith	Resonant type	Fair*	Bad	Bad
X. Zhang	Non-resonant type	Bad	Good	Good
Proposed	Non-resonant type	Good	Good	Good

*Anisotropy of the diagonal tensor components can be realized only by the orientation of the structure.

approach is shown in detail in Chapter 3.

1.4 Research Objectives and Goals

For overcoming the issues in Table 1.1, the objective of this research is to establish a novel method composing a medium for transformation electromagnetics. In addition, realizing a non-resonant type structure with full control of anisotropy including the off-diagonal tensor components, wideband property, and low-loss property is also another objective of this research.

In this thesis, research goals are set to 1) proposal of a theoretical model of anisotropic metamaterials based on the transmission-line approach [64]–[68], 2) proposal of a novel metamaterial based on the proposed theoretical model, and 3) experimental demonstrations of a cloak of invisibility with full control of anisotropy including the off-diagonal tensor components, wideband property, and low-loss property.

1.5 Academic Significance

There are three major academic significances in this research. The first significance is realizing anisotropy of the permeability tensor including the off-diagonal components by the proposed theoretical model. The conventional model cannot fully control anisotropy of the off-diagonal permeability tensor components shown in Fig. 1.5. On the other hand, the proposed theoretical model presented in this thesis can control all the components of the permeability tensor including controls of frequency dispersion. The second significance is a proposal of a novel metamaterial for implementing the theoretical model and establishing the design theory for composing a medium based on transformation electromagnetics. The third significance is showing the validity of the

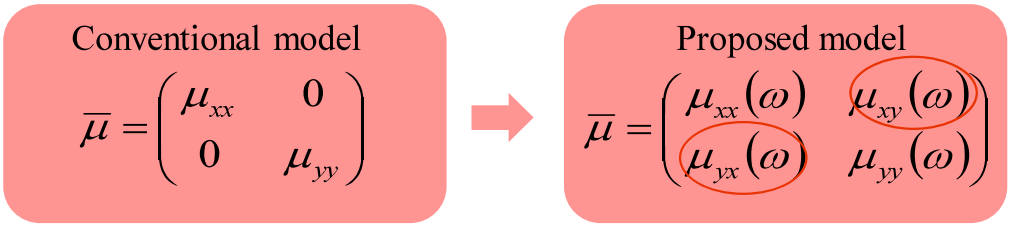

Fig. 1.5 Permeability tensor of the conventional model and the proposed model. By the proposed model in this research, anisotropy of the off-diagonal components can be controlled including the frequency dispersion.

theory by experimental demonstrations of cloaks of invisibility.

The field of the research of metamaterials and transformation electromagnetics discussed in this thesis are interdisciplinary academic field based on the electromagnetism, material science, computational science, science, nanotechnology, and the like, and developing this new academic area would open up a new scientific field of science.

1.6 Configuration of This Thesis

From the following chapters, results and outcomes in this research are presented. In Chapter 2, mathematical treatment and potentials of transformation electromagnetics are shown. Then, design formulas for a cylindrical cloak of invisibility are shown as an example [27], [28]. In Chapter 3, a theoretical model for transformation electromagnetics based on the transmission-line approach are proposed [69]–[73]. First, motivations of applying the transmission-line approach to transformation electromagnetics in this research are described. Secondly, the concept of transmission-line approach is shown from the point of view of duality of Maxwell's

equations and telegrapher's equations. Thirdly, an abstract equivalent circuit model for full-tensor anisotropic materials is presented with physical insights of their operation [70]. Fourthly, in order to confirm the validity of the theory, a carpet cloak of invisibility is designed with the circuit model. Finally, its operation is confirmed by circuit simulations. In Chapter 4, for implementing media based on the proposed circuit model, a novel metamaterial is proposed. First, distributed anisotropic metamaterials are proposed [74]. Secondly, equivalence to the proposed circuit model is studied. Thirdly, design formulas for structural parameters of metamaterial constituents are derived [74]. Fourthly, in order to confirm the validity of the theory, a carpet cloak of invisibility is designed with the proposed distributed anisotropic metamaterials. Finally, its operations and the validity of the theory are confirmed by circuit simulations. In Chapter 5, the designed carpet cloak is implemented, and experimental demonstrations are carried out [74]. The carpet cloak of invisibility designed in previous chapter is implemented with microstrip-line technology on the dielectric substrate. Then, by near-field measurements, its cloaking operations are demonstrated experimentally. In Chapter 6, in order to show further potentials of the proposed distributed anisotropic metamaterials, an illusion medium mimicking scattered waves of an arbitrary object is demonstrated numerically. First, the concept of the illusion media is shown. Secondly, an illusion medium mimicking a groove is designed with the proposed distributed anisotropic metamaterials. In addition, its operations are confirmed by circuit simulations. In Chapter 7, the results and outcomes as well as future prospects of this research are summarized.

Chapter 2 Theory of Transformation Electromagnetics

In this chapter, the theory and concept of transformation electromagnetics [27], [28], [31] is overviewed. First, mathematical treatment of transformation electromagnetics is shown [27], [28], [31]. Secondly, potentials of transformation electromagnetics are described by comparing with the conventional techniques for controlling electromagnetic waves. Finally, design formulas for a cylindrical cloak of invisibility are shown as an example [27], [28].

2.1 Material Interpretation of the Coordinate Transformation

Maxwell's equations can be invariant with arbitrary coordinate transformations. Let us consider a coordinate transformation from the area of $0 \le r \le b$ in Cartesian coordinate system shown in Fig. 2.1(a) to the area of $a \le r' \le b$ in another coordinate system shown in Fig. 2.1(b). Then, if the constitutive tensor $C^{\alpha'\beta'\mu'\nu'}$ has the following relations, Maxwell's equations can be invariant [28]:

$$C^{\alpha'\beta'\mu'\nu'} = \left|\det\left(\Lambda_{\alpha}^{\alpha'}\right)\right|^{-1} \Lambda_{\alpha}^{\alpha'} \Lambda_{\beta}^{\beta'} \Lambda_{\mu}^{\mu'} \Lambda_{\nu}^{\nu'} C^{\alpha\beta\mu\nu}, \tag{2.1}$$

where $\Lambda^{\alpha'}{}_{\alpha}$ is the Jacobian transformation matrix as:

$$\Lambda_{\alpha}^{\alpha'} = \frac{\partial x^{\alpha'}}{\partial x^{\alpha}}. \tag{2.2}$$

This is referred to as the topological interpretation of the coordinate transformation [28].

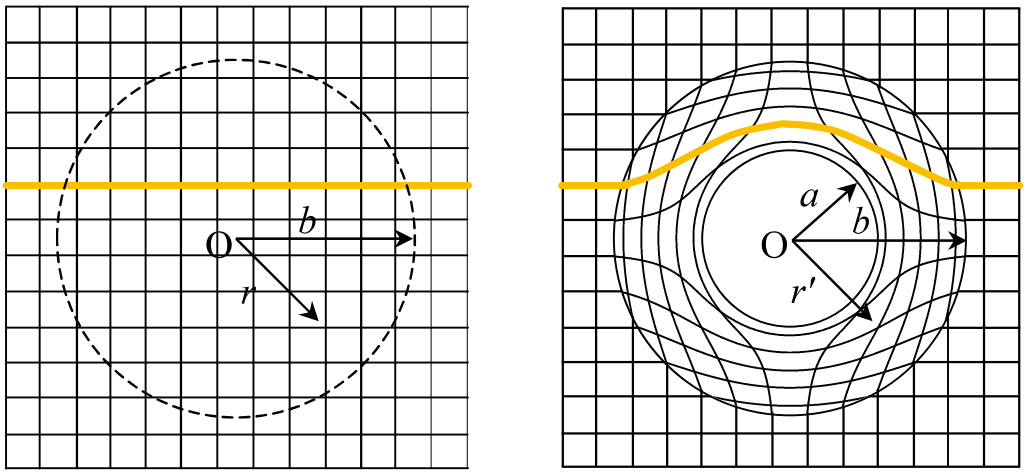

(a) (b)

Fig. 2.1 Conservation of Maxwell's equations based on the topological interpretation of the coordinate transformation [28]. (a) Original coordinate system. (b) Transformed coordinate system.

On the other hand, according to J. B. Pendry et al., Maxwell's equations can also be invariant [27], [28], [31] by interpreting the tensor conversions as operation to material parameters. Here, let us consider the coordinate system with the blank area of $0 \le r \le a$ as shown in Fig. 2.2. Then, if the area of $a \le r \le b$ is filled by inhomogeneous anisotropic materials with the permeability and permittivity based on the following relations, Maxwell's equations can also be invariant [27], [28], [31]:

$$\mu^{i'j'} = \left|\det\left(g^{i'j'}\right)\right|^{-1/2} g^{i'j'}\mu \tag{2.3}$$

$$\varepsilon^{i'j'} = \left|\det\left(g^{i'j'}\right)\right|^{-1/2} g^{i'j'}\varepsilon, \tag{2.4}$$

where μ and ε is the permeability and permittivity of the material filling the original area in Fig. 2.1(a). Besides, $g^{i'j'}$ is the metric given with $\Lambda^{i'}{}_{k}$ as:

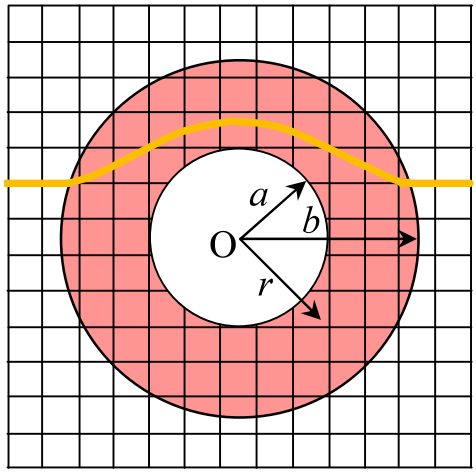

Fig. 2.2 Conservation of Maxwell's equations based on the material interpretation of the coordinate transformation [27], [28], [31]. The area of $a \le r \le b$ is filled by inhomogeneous anisotropic materials with the permeability and permittivity obtained from (2.3) and (2.4).

$$g^{i'j'} = \Lambda^{i'}_{k}\Lambda^{j'}_{l}\delta^{kl}. \tag{2.5}$$

This is referred to as material interpretation [27], [28], [31] and the concept of controlling electromagnetic waves by designing media based on the material interpretation is transformation electromagnetics.

2.2 Potentials of Transformation Electromagnetics

In order to control electromagnetic waves or lights, used reflection or refraction phenomena with mirrors, lenses, and the like have been used. For example, by using a prism, we can control rays of electromagnetic waves or lights as shown in Fig. 2.3(a). In this case, we have to design a system by considering reflections by impedance mismatching, incident angle dependencies, aberrations, and the like, simultaneously,

which tends to be complicated in a real electromagnetic or optical system.

On the other hand, for the case with the method using transformation electromagnetics as shown in Fig. 2.3(b), the situation is totally different. Based on this method, high controllability of electromagnetic waves or lights with enormously larger degree of freedom can be expected compared with conventional methods.

(a)

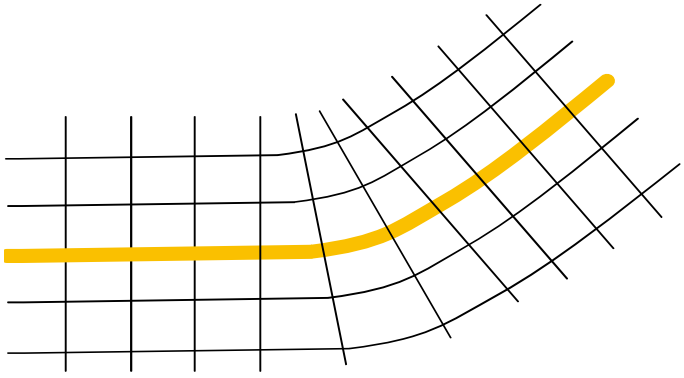

(b)

Fig. 2.3 Methods for controlling electromagnetic waves or lights. (a) Controlling lights by a prism. (b) Controlling lights by transformation electromagnetics.

2.3 Example of Cylindrical Cloaks

Here, design formulas for a cylindrical cloak of invisibility are shown as an example of transformation electromagnetics. As seen in Fig. 2.4, the cylindrical cloak can eliminate scattered waves from a cylindrical object by bending incident waves and mimic the free space. Therefore, the cylindrical object becomes invisible.

Now, let us consider the original area with radius b in the cylindrical coordinate system (r, θ, z) shown in Fig. 2.5(a). We also consider transforming the area into the area with inner radius a and outer radius b in the new cylindrical coordinate system (r', θ', z') of Fig. 2.5(b) by using the following relations [27], [28]:

$$r' = \frac{b-a}{b} r + a \tag{2.6}$$

$$\theta' = \theta \tag{2.7}$$

$$z' = z\,, \tag{2.8}$$

where $0 \le r \le b$, $0 \le \theta \le 2\pi$, $a \le r' \le b$, and $0 \le \theta' \le 2\pi$. From (2.3) and (2.4), we can obtain theoretical formulas of material parameters for the cylindrical cloak shown in the following [27], [28]:

$$\mu_{r'} = \varepsilon_{r'} = \frac{r'-a}{r'} \tag{2.9}$$

$$\mu_{\theta'} = \varepsilon_{\theta'} = \frac{r'}{r'-a} \tag{2.10}$$

$$\mu_{z'} = \varepsilon_{z'} = \left(\frac{b}{b-a}\right)^2 \frac{r'-a}{r'}\,. \tag{2.11}$$

A cylindrical cloak of invisibility can be realized by composing inhomogeneous anisotropic metamaterials according to (2.9)–(2.11) in the area of Fig. 2.5(b).

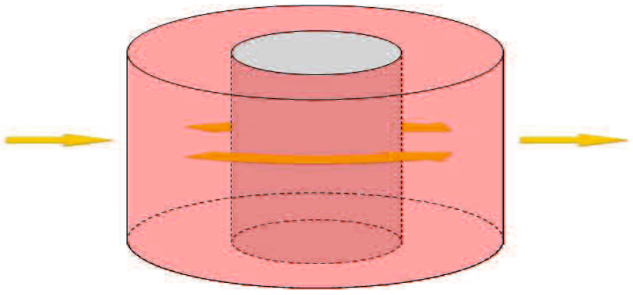

(a)

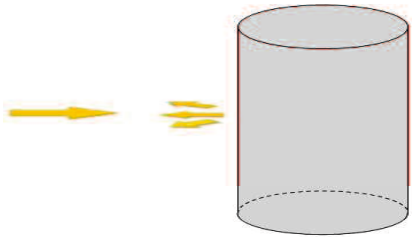

(b)

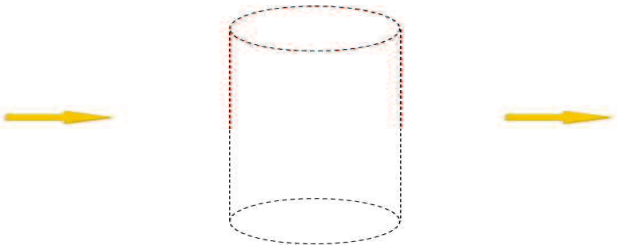

(c)

Fig. 2.4 The concept of a cylindrical cloak. (a) A cylindrical cloak of invisibility mimicking the free space. (b) Scattering from a cylindrical object to be eliminated. (c) Free space to be mimicked.

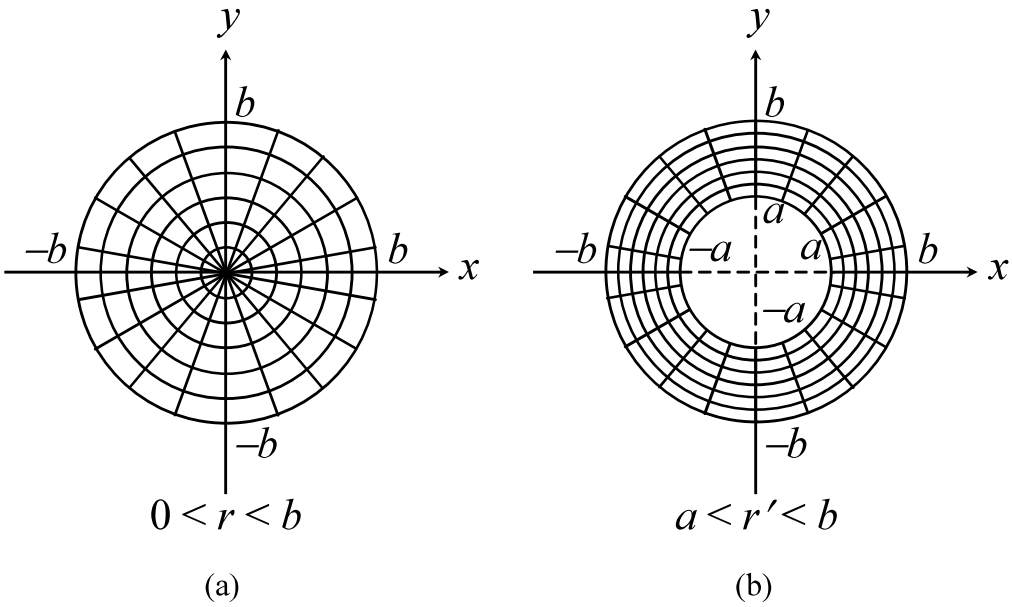

Fig. 2.5 Coordinate transformation for a cylindrical cloak. (a) Original coordinate system (r, θ). (b) Transformed coordinate system (r', θ').

Chapter 3 Transmission-Line Approach for Transformation Electromagnetics

In this chapter, the theoretical model for transformation electromagnetics is proposed based on the transmission-line approach [64]–[68]. First, a motivation for applying the transmission-line approach to transformation electromagnetics in this research is described with a background of left-handed metamaterials researches. Secondly, the concept of the transmission-line approach for designing metamaterials is shown. Thirdly, the equivalent circuit model for full-tensor anisotropic metamaterials is proposed [69]–[73]. Fourthly, a carpet cloak of invisibility is designed with the circuit model. Finally, in order to confirm operations and the validity of the design theory, circuit simulations are carried out with a SPICE simulator.

3.1 Transmission-Line Approach and Transformation Electromagnetics

Historically, the resonant type and the non-resonant type structures have been proposed for realization of left-handed metamaterials. The first resonant type left-handed metamaterial has been realized with metal wires and split-ring resonators [6]. However, due to its resonant property, its operation bandwidth is extremely narrow and the loss is very high. On the other hand, the transmission-line approach in which materials are expressed by small sections of circuit models as shown in Fig. 3.1. For example, let us consider the CRLH transmission-line model shown in Fig. 3.1(b) [19], [20]. Here, by increasing the coupling among unit cells, wideband and low-loss properties are realized simultaneously. In addition, the materials can be

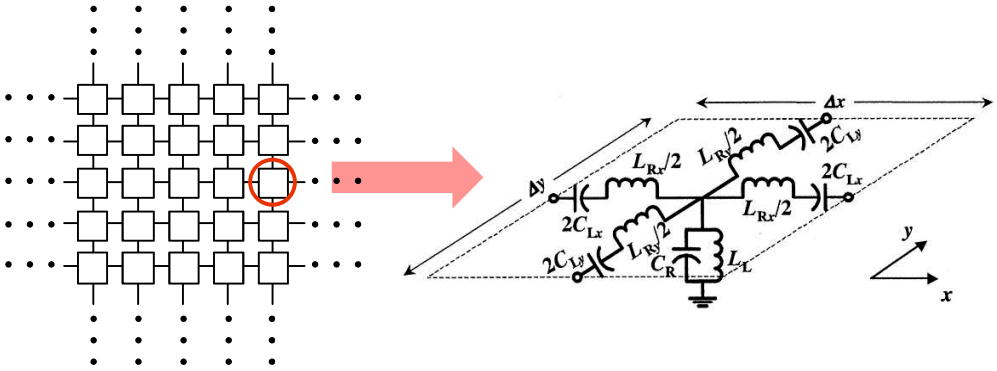

(a) (b)

Fig. 3.1 An example of circuit expression of materials by the transmission line approach. (a) Discretized material with the circuit sections. (b) CRLH transmission-line model [19], [20].

straightforwardly designed based on the circuit theory. Motivation of this research is to realize anisotropy, wideband properties, and low-loss properties, which are issues for transformation electromagnetics, by the transmission-line approach.

3.2 Concept of the Transmission-Line Approach

Generally speaking, it is known that there is a duality between telegrapher's equations and Maxwell's equations [64]–[68]. For example, voltage corresponds to electric field, and current corresponds to magnetic field. From this duality, we can express materials by using circuits.

Now, let us consider the 1-D circuit [68] with the series impedance $Z/2 = (Z'\Delta x)/2$ and the shunt admittance $Y = Y'\Delta x$ shown in Fig. 3.2. Defining the node voltages (V_x, V_{x+1}) and the currents (I_x, I_{x+1}) as shown in the figure, we can obtain the circuit equations

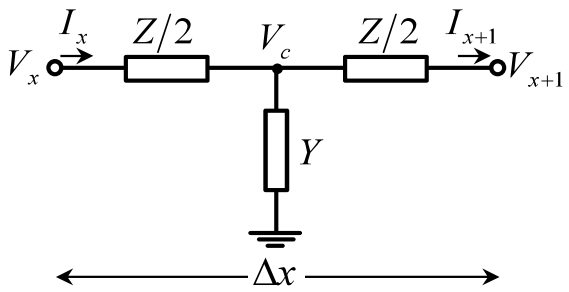

Fig. 3.2 Equivalent circuit model for 1-D materials [68].

from the Kirchhoff's voltage and current laws as:

$$\frac{V_{x+1}-V_x}{\Delta x} = Z'\left(-\frac{I_{x+1}+I_x}{2}\right) \tag{3.1}$$

$$\left(-\frac{I_{x+1}-I_x}{\Delta x}\right) = YV_c, \tag{3.2}$$

where V_c is the voltage at the center node. On the other hand, let us also consider the 1-D Maxwell's equations for z-polarized TE waves in the materials shown in the following:

$$\frac{\partial E_z}{\partial x} = j\omega\mu H_y \tag{3.3}$$

$$\frac{\partial H_y}{\partial x} = j\omega\varepsilon E_z, \tag{3.4}$$

where μ and ε are permeability and permittivity, respectively. Here, comparing (3.1) and (3.2) with (3.3) and (3.4) under the condition of the infinitesimal limit $\Delta x \to 0$, we can obtain the following relations among the circuit parameters and the material parameters [68]:

$$Z' = j\omega\mu \tag{3.5}$$

$$Y' = j\omega\varepsilon\,. \tag{3.6}$$

Therefore, materials can be expressed by using the circuit model. For example, 2-D isotropic materials and anisotropic materials without the off-diagonal components can be expressed by using the circuit models shown in Fig. 3.3(a) and Fig. 3.3(b), respectively [65], [66], [68]. However, a circuit model of 2-D full-tensor anisotropic materials is required to design media based on transformation electromagnetics. In the next section, the circuit model for 2-D full-tensor anisotropic materials is proposed.

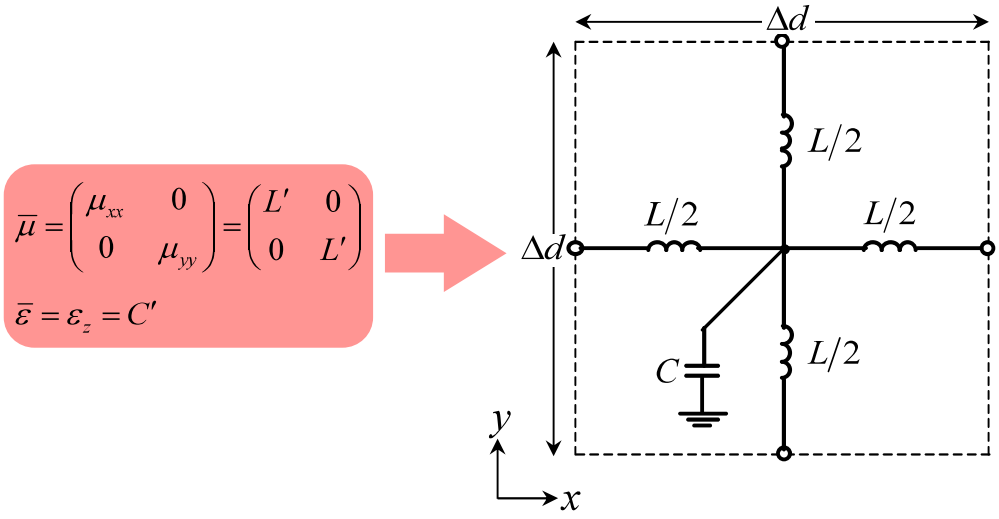

(a)

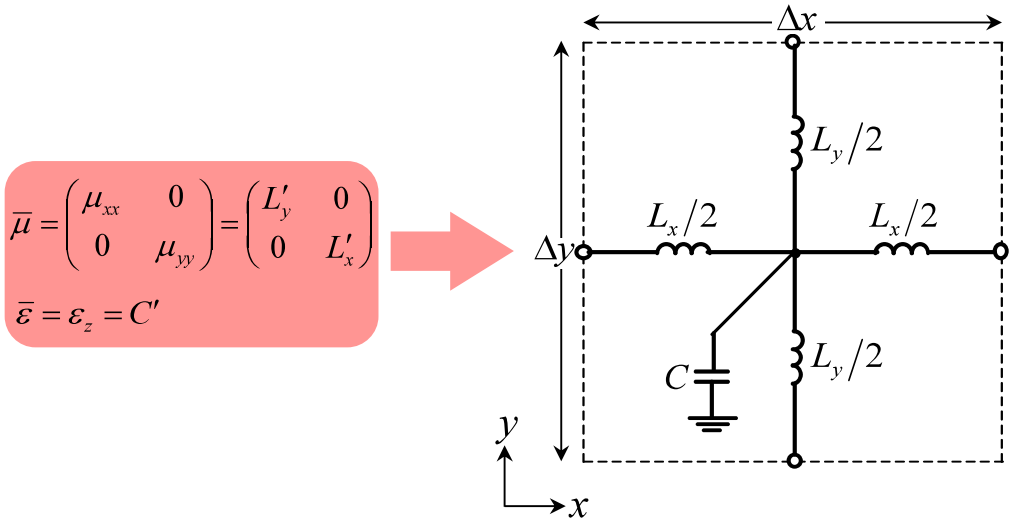

(b)

Fig. 3.3 Equivalent circuit models for 2-D materials. (a) For 2-D isotropic materials [65], [66], [68]. (b) For 2-D anisotropic materials without the off-diagonal components [65], [66], [68]. Here, L, L_x, and L_y are the self inductances of each branch, and C is the capacitance to the ground. ($'$) denotes per-unit-length quantities.

3.3 Equivalent Circuit Model for Full-Tensor Anisotropic Materials

Fig. 3.4 shows the proposed equivalent circuit models for full-tensor anisotropic materials [69]–[73]. For simplicity, a square unit cell $\Delta x = \Delta y = \Delta d$ is assumed. Here, x and y branches have the self-inductances $L_x/2$ and $L_y/2$, respectively, and those are magnetically coupled with a mutual inductance $M/2$ ($M > 0$ is assumed). Figs. 3.4(a) and (b) are isomer circuits with different coupling method of x- and y- branches. In addition, C is a capacitance to the ground. In the following, it is shown that full-tensor anisotropic materials can be expressed by the proposed circuit models.

First, we define the node voltages (V_x, V_{x+1}, V_y, and V_{y+1}) and the currents (I_x, I_{x+1}, I_y, and I_{y+1}) as shown in Fig. 3.4. From the Kirchhoff's voltage and current laws, we can obtain circuit equations as:

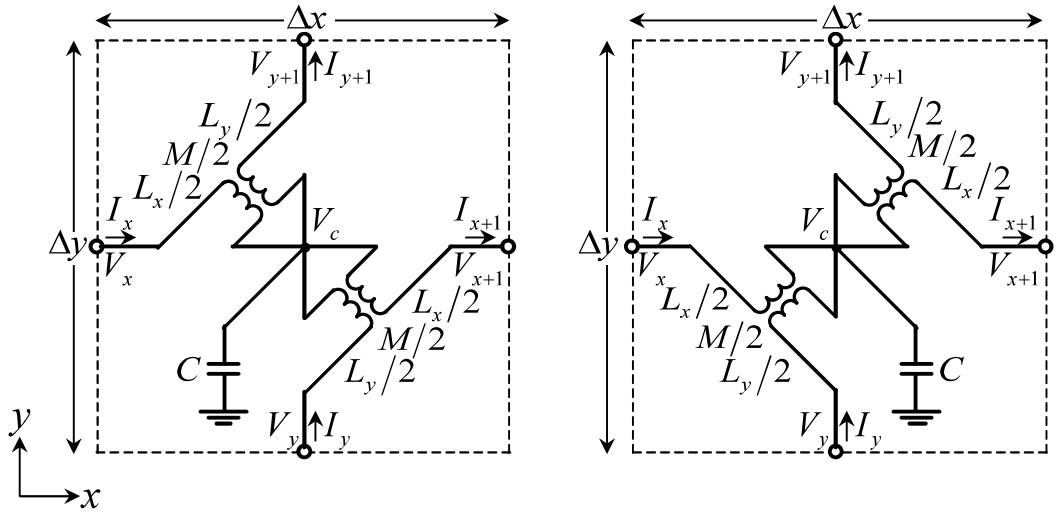

Fig. 3.4 Proposed equivalent circuit models for full-tensor anisotropic materials [69]–[73]. (a) For the $\mu_{xy} = \mu_{yx} > 0$ case. (b) For the $\mu_{xy} = \mu_{yx} < 0$ case.

$$\frac{V_{x+1}-V_x}{\Delta d}=\pm j\omega M'\left(\frac{I_{y+1}+I_y}{2}\right)+j\omega L'_x\left(-\frac{I_{x+1}+I_x}{2}\right) \tag{3.7}$$

$$\frac{V_{y+1}-V_y}{\Delta d}=-j\omega L'_y\left(\frac{I_{y+1}+I_y}{2}\right)\mp j\omega M'\left(-\frac{I_{x+1}+I_x}{2}\right) \tag{3.8}$$

$$\left(-\frac{I_{x+1}-I_x}{\Delta d}\right)-\left(\frac{I_{y+1}-I_y}{\Delta d}\right)=j\omega C'V_c\,, \tag{3.9}$$

where V_c is the voltage at the center node and (') denotes per-unit-length quantities as $L'_x = L_x/\Delta d$, $L'_y = L_y/\Delta d$, $M' = M/\Delta d$, and $C' = C/\Delta d$. In addition, the upper and lower signs of the double signs correspond to the cases of Fig. 3.4(a) and (b), respectively. On the other hand, Maxwell's equations for z-polarized TE waves in a full-tensor anisotropic material can be written as the following:

$$\frac{\partial E_z}{\partial x}=j\omega\mu_{yx}H_x+j\omega\mu_{yy}H_y \tag{3.10}$$

$$\frac{\partial E_z}{\partial y}=-j\omega\mu_{xx}H_x-j\omega\mu_{xy}H_y \tag{3.11}$$

$$\frac{\partial H_y}{\partial x}-\frac{\partial H_x}{\partial y}=j\omega\varepsilon_z E_z\,, \tag{3.12}$$

where μ_{xx}, μ_{xy}, μ_{yx}, and μ_{yy} are permeability tensor components and ε_z is permittivity in the z-direction. Here, from the duality between circuit equations and Maxwell's equations, we can obtain the following relations among the circuit parameters and the material parameters [70] by comparing (3.7)–(3.9) with (3.10)–(3.12) under the condition of the infinitesimal limit $\Delta d\to 0$:

$$\begin{pmatrix} L'_y & \pm M' \\ \pm M' & L'_x \end{pmatrix}=\begin{pmatrix} \mu_{xx} & \mu_{xy} \\ \mu_{yx} & \mu_{yy} \end{pmatrix} \tag{3.13}$$

$$C' = \varepsilon_z , \tag{3.14}$$

where the upper and lower signs of the double signs also correspond to the cases of Figs. 3.4(a) and (b), respectively. From these relations, it can be seen that the diagonal permeability tensor components μ_{xx} and μ_{yy} correspond to the self-inductances per-unit-length L'_y and L'_x, respectively, and more importantly, the off-diagonal permeability tensor components μ_{xy} and μ_{yx} correspond to the mutual inductance per-unit-length M'. In addition, permittivity ε_z corresponds to the capacitance per-unit-length C'. Incidentally, proposed circuit models can also be applied to TM wave problems [70] by interchanging the permeability tensor and the permittivity tensors as the following [70]:

$$\begin{pmatrix} L'_y & \pm M' \\ \pm M' & L'_x \end{pmatrix} = \begin{pmatrix} \varepsilon_{xx} & \varepsilon_{xy} \\ \varepsilon_{yx} & \varepsilon_{yy} \end{pmatrix} \tag{3.15}$$

$$C' = \mu_z , \tag{3.16}$$

It is noted from (3.13) that when M takes to 0, the circuit models become the same as the circuit of Fig. 3.3 (b) for anisotropic materials without the off-diagonal components. In addition, from (3.13) and (3.14), it is also noted that the circuit models are independent of the frequency and they correspond to the homogeneous medium with μ_{xx}, μ_{xy}, μ_{yx}, μ_{yy}, and ε_z under the condition of the infinitesimal limit $\Delta d \rightarrow 0$ (or $\lambda_g >> \Delta d$). Therefore, the circuit models have intrinsically wideband property from DC to certain frequencies in which the discretization errors cannot be neglected.

From these results, it can be concluded that the proposed circuit models can simultaneously realize anisotropy with the off-diaconal components, wideband property, and low-loss property.

3.4 Carpet Cloak Design

In order to confirm the validity of the circuit model, we design a 2-D carpet cloak of invisibility [31]–[35], [38] with the proposed circuit model. The carpet cloak (see Fig. 3.5(a)) can mimic specular reflections by a flat floor (see Fig. 3.5(b)) and suppress scatted waves by a bump (see Fig. 3.5(c)). Therefore, the bump under the carpet becomes invisible.

First, we determine an appropriate coordinate transformation for the carpet cloak. Let us consider the original area of $-p \le x \le p$ and $0 \le y \le h$ in Cartesian coordinate system (x, y) of Fig. 3.6(a) including a bump with height A to be hidden. Then, we also consider transforming the area into the area of $-p \le x' \le p$ and $A\{1 - (x/p)^2\}^2 \le y' \le h$ in the non-conformal cylindrical coordinate system (x', y') of Fig. 3.6(b) by using the following relations:

$$x' = x \tag{3.17}$$

$$y' = y + A\left(1 - \frac{y}{h}\right)\left\{1 - \left(\frac{x}{p}\right)^2\right\}^2 . \tag{3.18}$$

In the following design, we chose the parameters as $p = h = 10\Delta d$ and $A = 0.3h = 3\Delta d$.

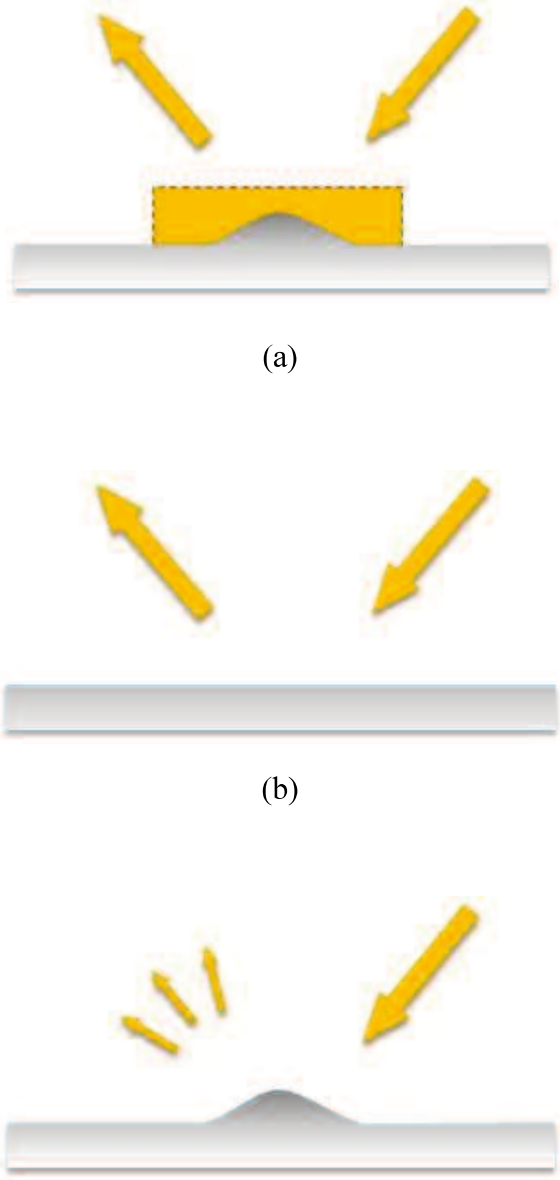

Fig. 3.5 The concept of a carpet cloak of invisibility. (a) A carpet cloak mimicking specular reflections by a flat floor. (b) Specular reflection by a flat floor to be mimicked. (c) Scattering by a bump to be suppressed.

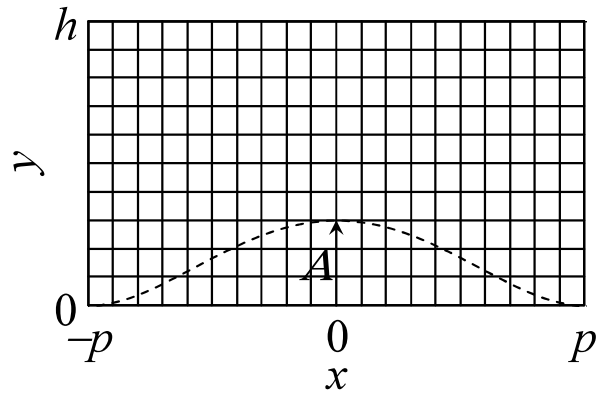

(a)

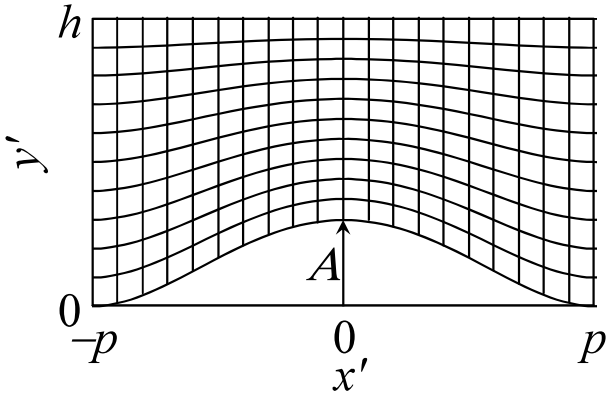

(b)

Fig. 3.6 Coordinate transformation for the carpet cloak design. (a) Original coordinate system (x, y). (b) Transformed coordinate system (x', y').

Secondly, we calculate the equivalent circuit parameters L_x, L_y, M, and C of Figs. 3.4(a) and (b) for designing the carpet cloak with the coordinate transformation of Fig. 3.6. Substituting the calculated μ_{xx}, μ_{xy}, μ_{yx}, μ_{yy}, and ε_z from (2.3) and (2.4) for the following relations according to (3.15) and (3.16), we can obtain the circuit parameters:

$$L_x = \mu_{yy}\Delta d\,, \tag{3.19}$$

$$L_y = \mu_{xx}\Delta d\,, \tag{3.20}$$

$$M = \pm\mu_{xy}\Delta d = \pm\mu_{yx}\Delta d (M > 0)\,, \tag{3.21}$$

$$C = \varepsilon_z \Delta d\,. \tag{3.22}$$

Figs. 3.7(a)–(c) show obtained values of L'_x, L'_y, and M' normalized by the permeability of vacuum μ_0, and Fig. 3.7(d) shows the value of C' normalized by the primitively of vacuum ε_0, respectively. Here, for the half area of $x < 0$, the unit cell of Fig 3.4(a) is used due to $\mu_{xy} = \mu_{yx} > 0$ according to (2.3), and for the half area of $x > 0$, the unit cell of Fig 3.4(b) is used due to $\mu_{xy} = \mu_{yx} < 0$. From Figs. 3.7(a) and (b), it is seen that L'_x/μ_0 and L'_y/μ_0 take minimum and maximum at the center of the area $(x, y) = (0, y)$, respectively. Besides, from Fig. 3.7(c), it is seen that M'/μ_0 takes 0 value at the center, top, and both sides of the area $(0, y)$, (x, h), and $(\pm p, y)$, respectively, and the off-diagonal permeability tensor components μ_{xy} and μ_{yx} become non-zero at the other area. In addition, from Fig. 3.7(d), it is seen that C'/ε_0 takes maximum at the center of the area. The operations of the carpet cloak are confirmed by carrying out circuit simulations in the next section.

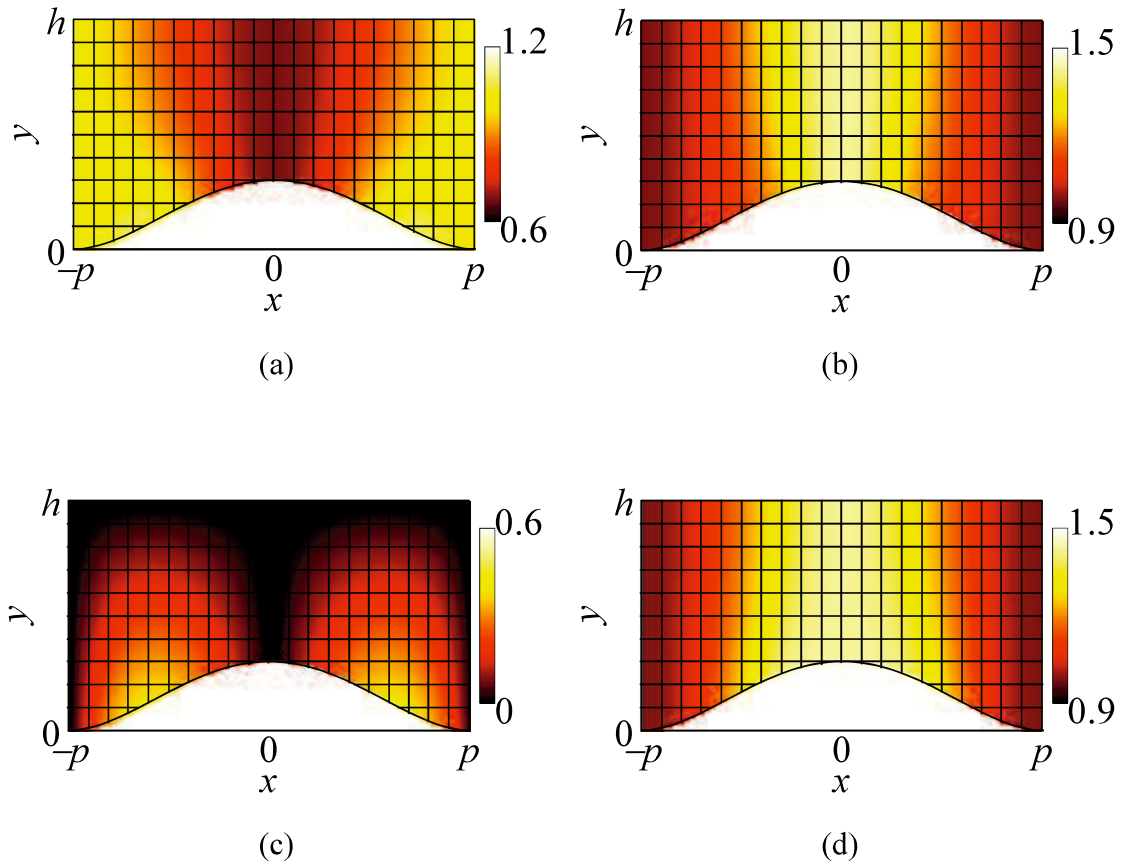

Fig. 3.7 Equivalent circuit parameters of the circuit models in Fig. 3.4 for the carpet cloak design. The unit cell of Fig. 3.4(a) is used for the half area of $x < 0$, and Fig. 3.4(b) is used for the half area of $x > 0$. (a) Normalized self-inductance per-unit-length L'_x/μ_0. (b) Normalized self-inductance per-unit-length L'_y/μ_0. (c) Normalized mutual inductance per-unit-length M'/μ_0. (d) Normalized capacitance per-unit-length C'/ε_0.

3.5 Circuit Simulations

In order to validate the carpet cloak design, circuit simulations are carried out with a SPICE simulator.

First, we prepare a node list of 20 × 10 cells for the carpet cloak area shown in Fig.

3.8(a). Here, for the left half area of Fig. 3.8(a), the unit cell of Fig 3.4(a) is used, and for the right half area, the unit cell of Fig 3.4(b) is used. Besides, the equivalent circuit parameters for each unit cell are given from the values in Fig 3.7(a)–(d). Then, we put the carpet cloak at the bottom center of the isotropic area discretized with $n_x \times n_y = 300 \times 150$ cells as shown in Fig. 3.8(b). The unit cell of Fig. 3.3(a) is used for the isotropic area. The circuit parameters are chosen to be $L = \mu_0 \Delta d$ and $C = \varepsilon_0 \Delta d$ in order to assume the vacuum.

Fifty in-phase voltage sources ($n_s = 50$) with the internal impedance of the Bloch impedance in the isotropic area are connected at the nodes in the center of the top row to illuminate the bump with a normal incident beam ($\theta_{inc} = 0$ deg). The amplitudes of the voltage sources are set to form the Gaussian beam with the beam waist of $10\Delta d$. Nodes on the bottom boundary of Fig. 3.8(b) are short-circuited including the bump area, and the other nodes on the top row and the side columns are terminated by resistors with the Bloch impedance in the isotropic area.

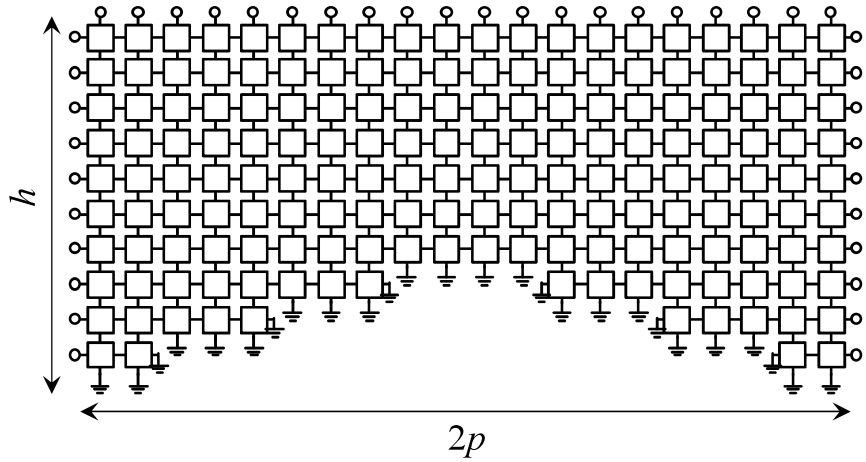

(a)

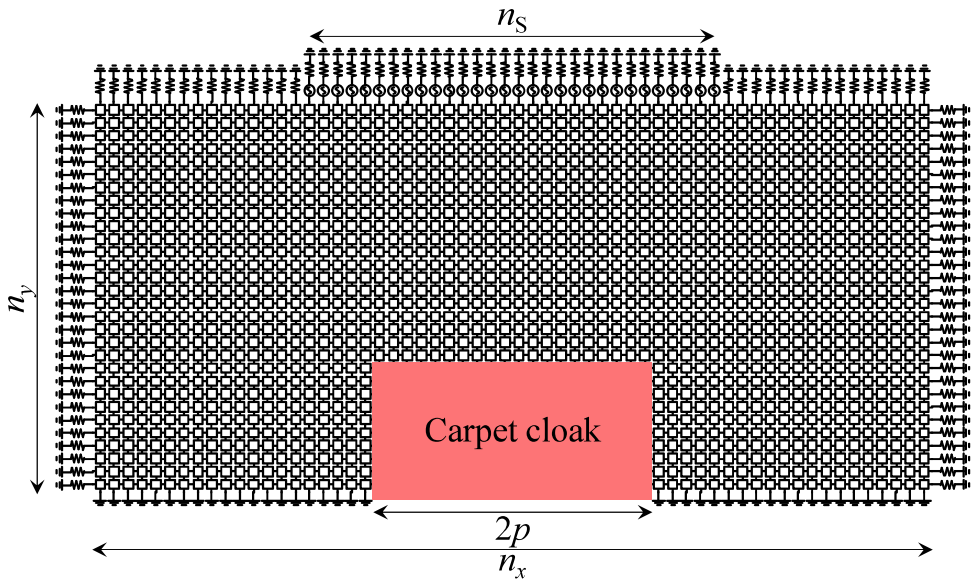

(b)

Fig. 3.8 Configuration of circuit simulations. (a) Cloak area with 20 × 10 unit cells ($p = h = 10\Delta d$). (b) Configuration for the normal incidence case ($\theta_{inc} = 0$ deg) with $n_x \times n_y = 300 \times 150$ unit cells and fifty in-phase voltage sources ($n_s = 50$).

Figs. 3.9(a)–(c) show calculated complex voltage distributions for the cases with (a) the carpet cloak, (b) a flat floor, and (c) a bump without the carpet cloak, respectively. Here, the wavelength is chosen as $\lambda_g = 12\Delta d$. For the simulation of a flat floor, the cloak region is replaced by section with 20 × 10 cells of Fig. 3.3(a) shown in Fig. 3.10. By comparing Figs. 3.9(a) with (b), it is seen that distributions agree well each other and the carpet cloak sufficiently mimics the flat floor. Besides, by comparing Figs. 3.9(a) with (c), it is clearly seen that scattered waves by the bump are considerably suppressed by the carpet cloak.

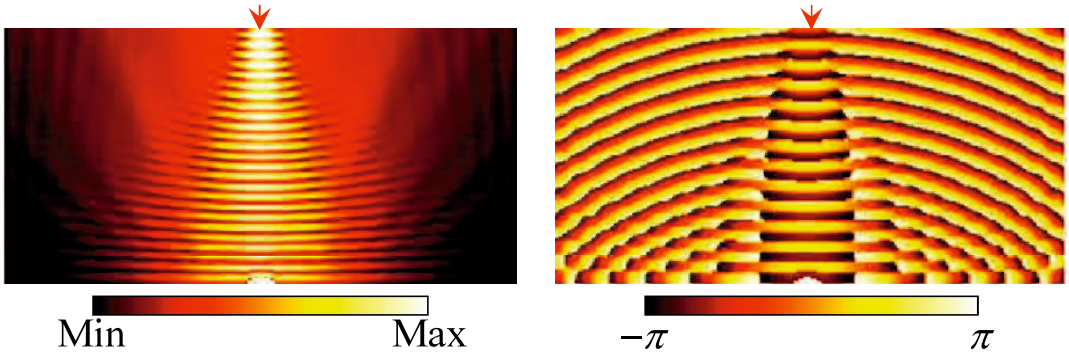

(a)

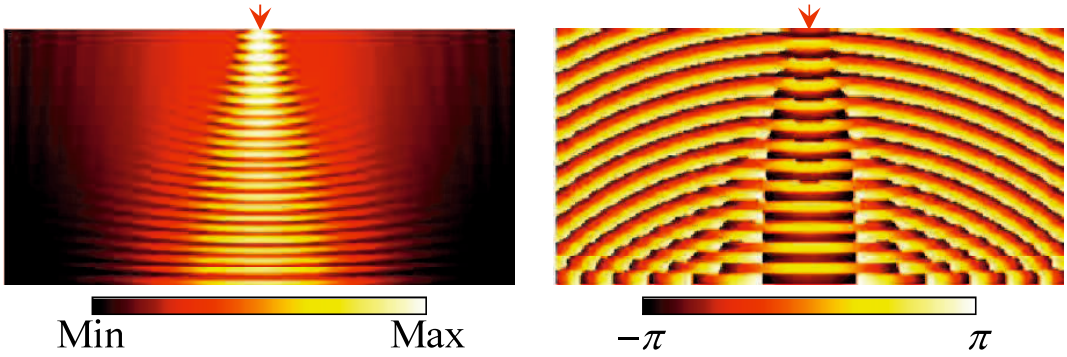

(b)

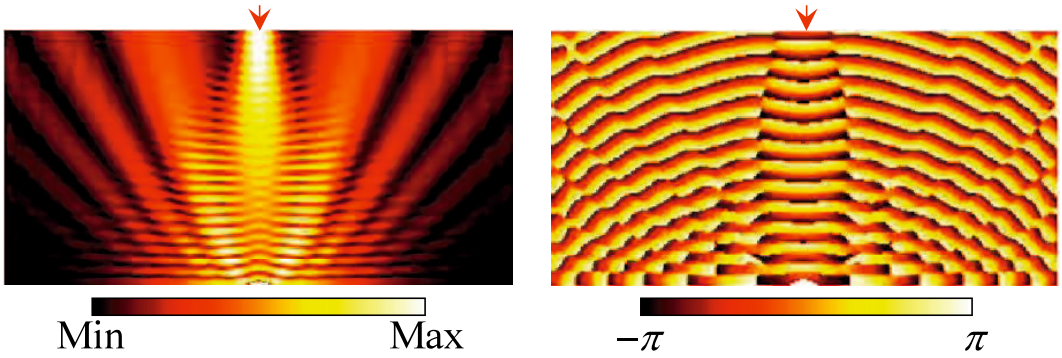

(c)

Fig. 3.9 Calculated complex voltage distributions ($\lambda_g = 12\Delta d$). Left and right figures are amplitude and phase, respectively. (a) Carpet cloak. (b) Flat floor. (c) Bump without the carpet cloak.

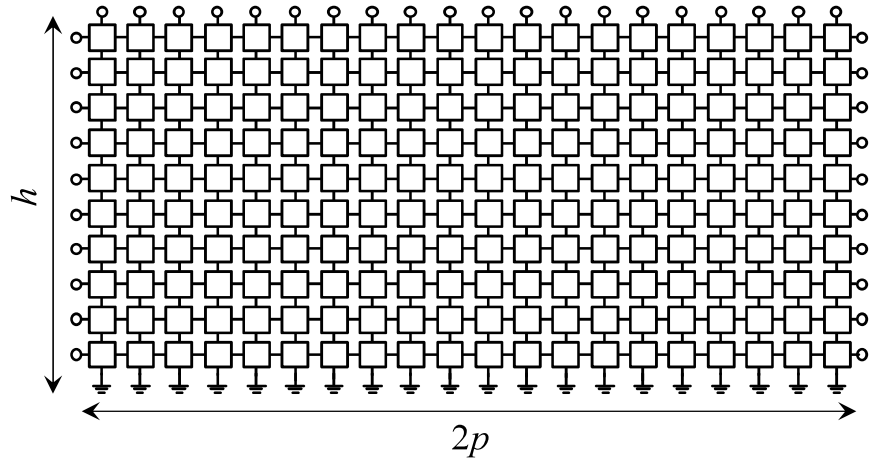

Fig. 3.10 Section of 20 × 10 cells for the flat floor simulations. The unit cell of Fig 3.3(a) is used.

Figs. 3.11(a)–(c) show similar results for the case with the shorter wave length $\lambda_g = 6\Delta d$. From these results, it is also seen that the carpet cloak suppresses scattered waves from the bump and mimic the flat floor, though the level of scattered waves is slightly increased (compare Fig. 3.11 (a) with Fig. 3.9 (a)). In contrast, it is expected for the carpet cloak to work also at lower frequency down to DC since the homogeneous medium approximation holds. Roughly speaking, the designed carpet cloak works if $\lambda_g > 6\Delta d$.

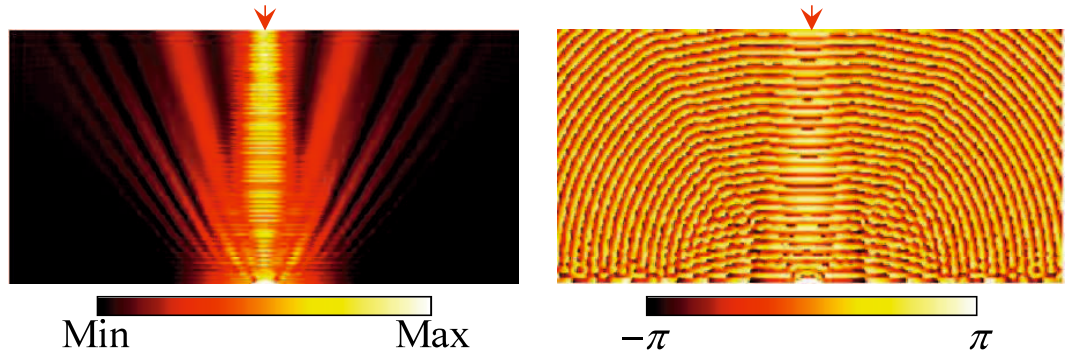

(a)

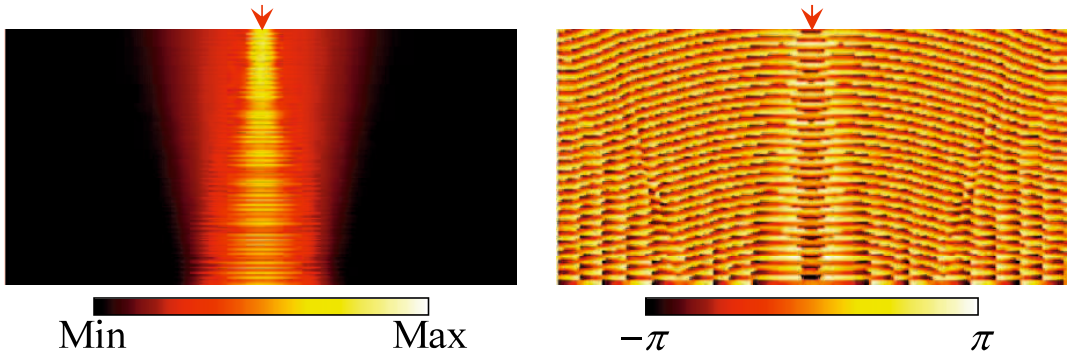

(b)

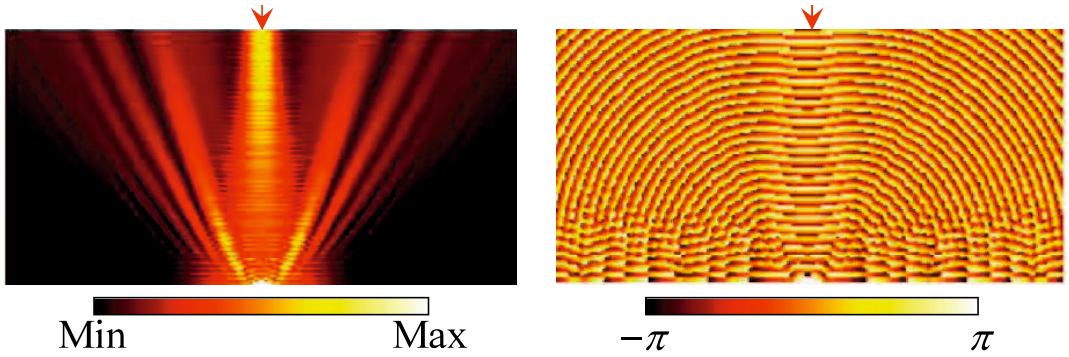

(c)

Fig. 3.11 Calculated complex voltage distributions ($\lambda_g = 6\Delta d$). Left and right figures are amplitude and phase, respectively. (a) Carpet cloak. (b) Flat floor. (c) Bump without the carpet cloak.

In order to further confirm the operation of the carpet cloak, circuit simulations for the oblique incidence cases are also carried out. Here, the incident angles are chosen as θ_{inc} = 30, 45, and 60 deg. Fig. 3.12 shows the configuration of the circuit simulation for the case with θ_{inc} = 45 deg, for example. In this case, the calculated area is $n_x \times n_y$ = 300 × 150 cells and a hundred in-phase voltage sources (n_{s} = 100) with the Gaussian amplitude distribution are connected at the nodes of the staircase boundary in the top-right corner. For the case with θ_{inc} = 30 and 60 deg, the calculated area is $n_x \times n_y$ = 172 × 120 cells and 240 × 86 cells, respectively, and the voltage sources are connected similarly at the nodes of the staircase boundary corresponding to those incident angles.

Figs. 3.13–3.15 show the calculated complex voltage distributions for the cases with θ_{inc} = 30, 45, and 60 deg, respectively. In these figures, the calculated results for the

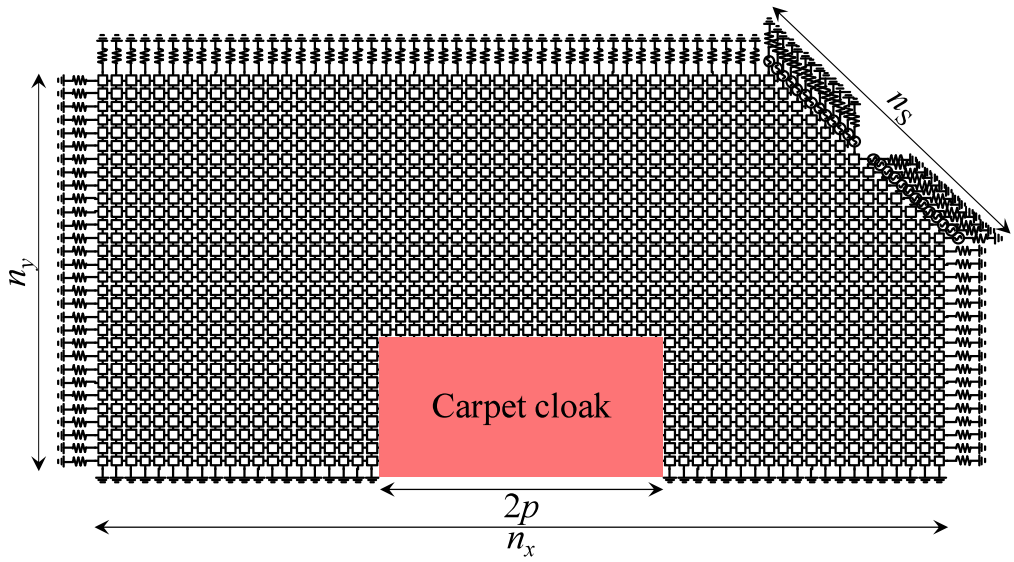

Fig. 3.12 An example of the configuration of circuit simulations for the oblique θ_{inc} = 45 deg incidence case. The calculated area is $n_x \times n_y$ = 300 × 150 unit cells and a hundred in-phase voltage sources (n_{s} = 100) are connected at the nodes of the staircase boundary in the top-right corner.

cases with (a) the carpet cloak, (b) a flat floor, and (c) a bump without the carpet cloak are included. Here, the wavelength is chosen as $\lambda_g = 12\Delta d$. From these figures, it is seen that the carpet cloak works well even with the oblique incidence cases.

From these results, it can be concluded that the validity of the proposed circuit model and operations of the carpet cloak with the circuit model are confirmed by the circuit simulations.

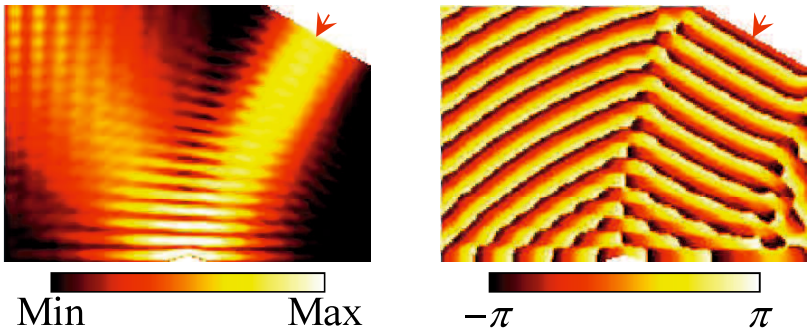

(a)

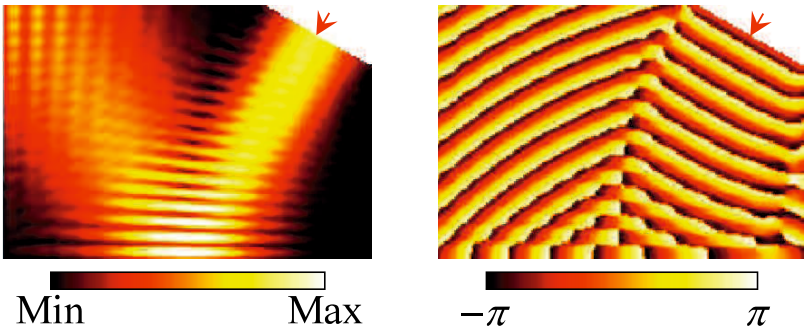

(b)

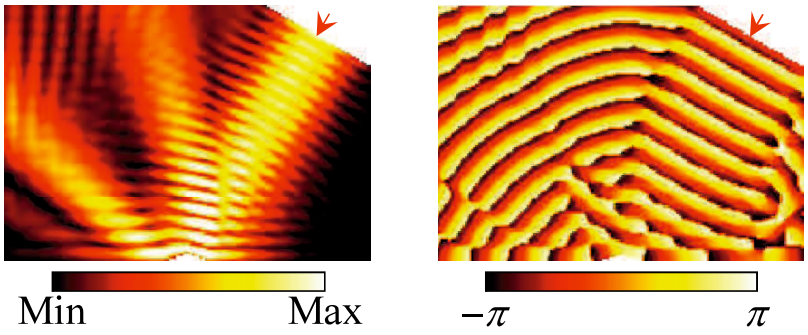

(c)

Fig. 3.13 Calculated complex voltage distributions for the case with θ_{inc} = 30 deg ($\lambda_g = 12\Delta d$). Left and right figures are amplitude and phase, respectively. (a) Carpet cloak. (b) Flat floor. (c) Bump without the carpet cloak.

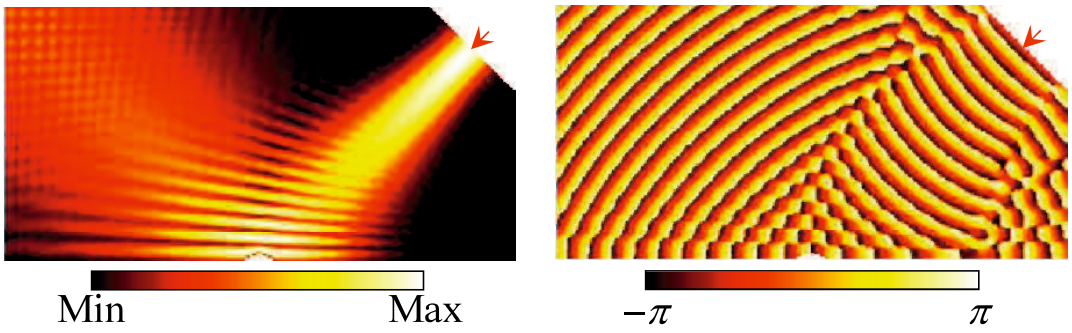

(a)

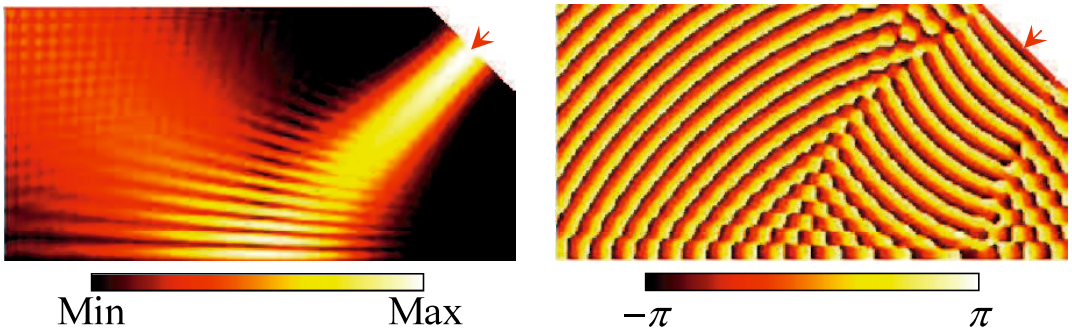

(b)

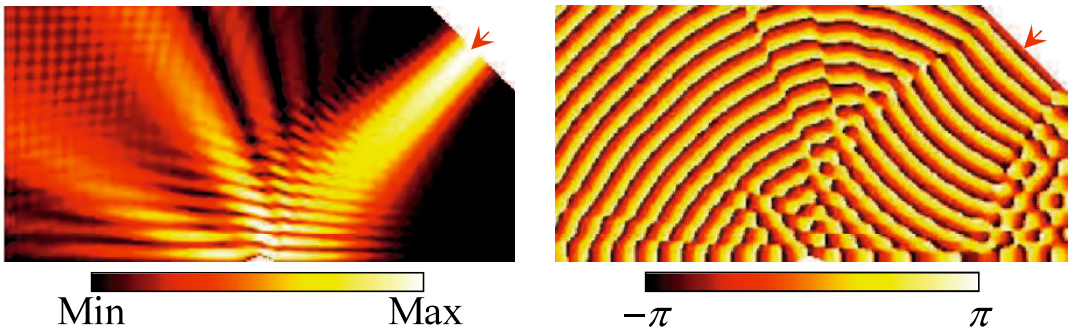

(c)

Fig. 3.14 Calculated complex voltage distributions for the case with θ_{inc} = 45 deg ($\lambda_g = 12\Delta d$). Left and right figures are amplitude and phase, respectively. (a) Carpet cloak. (b) Flat floor. (c) Bump without the carpet cloak.

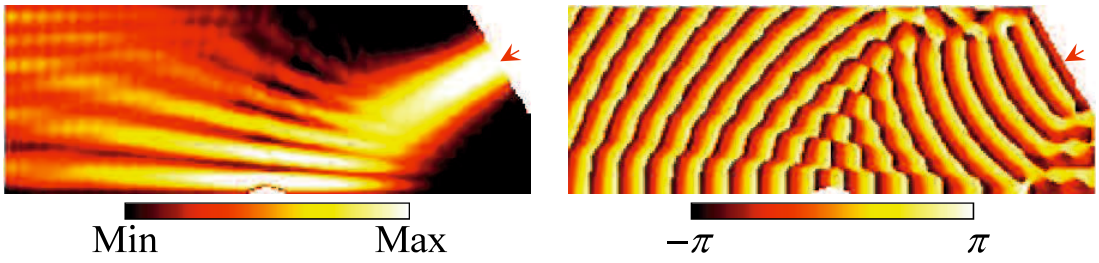

(a)

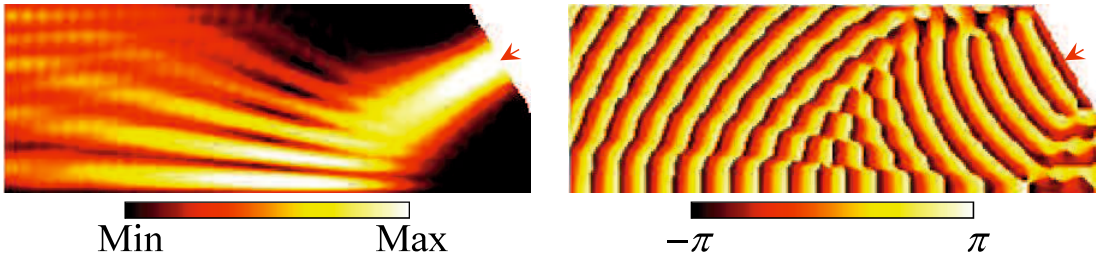

(b)

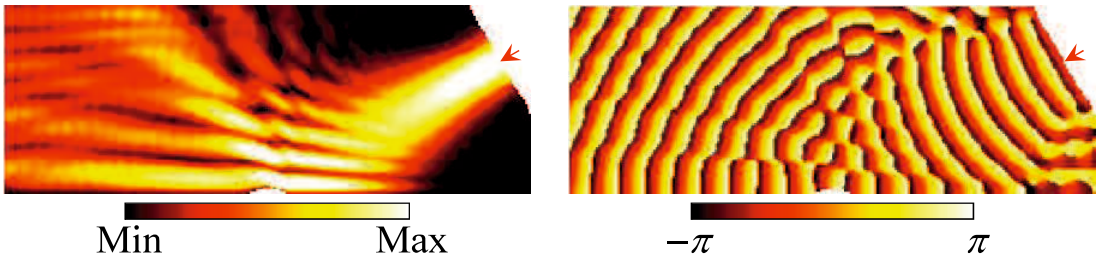

(c)

Fig. 3.15 Calculated complex voltage distributions for the case with θ_{inc} = 60 deg ($\lambda_g = 12\Delta d$). Left and right figures are amplitude and phase, respectively. (a) Carpet cloak. (b) Flat floor. (c) Bump without the carpet cloak.

Chapter 4 Distributed Full-Tensor Anisotropic Metamaterials

In the previous chapter, the equivalent circuit model for full-tensor anisotropic materials has been proposed. In this chapter, a novel material model for implementing the proposed circuit model is proposed. First, as a new material model, the distributed anisotropic metamaterials are proposed [74]. Secondly, equivalence of the metamaterial to the circuit model is shown. Thirdly, design formulas for structural parameters of the metamaterial are derived [74]. Fourthly, the carpet cloak of invisibility is designed with the distributed anisotropic metamaterials. Finally, its operations and the validity of the design theory are confirmed by circuit simulations.

4.1 Distributed Anisotropic Metamaterials

First, let us consider rigorous transformation of the equivalent circuit model in Fig. 3.4 into the circuit models shown in Fig. 4.1 [74] by using the T-circuit expression of the ideal transformer. Then, let us also consider to replace the inductance elements with the transmission-line sections as shown in Fig. 4.2 [74], leading to the proposed distributed anisotropic metamaterials. Here, Z_{0x}, Z_{0y}, and $Z_{0\mathrm{M}}$ are characteristic impedances and $\beta_x l_x$, $\beta_y l_y$, and $\beta_{\mathrm{M}} l_{\mathrm{M}}$ are electrical lengths of the transmission-line sections. However, the distributed anisotropic metamaterials do not always fully correspond to the circuit model in Fig. 3.4 just by replacing the inductance elements with the transmission-line sections. The equivalence between the circuit model and the proposed distributed anisotropic metamaterials is discussed in the next section.

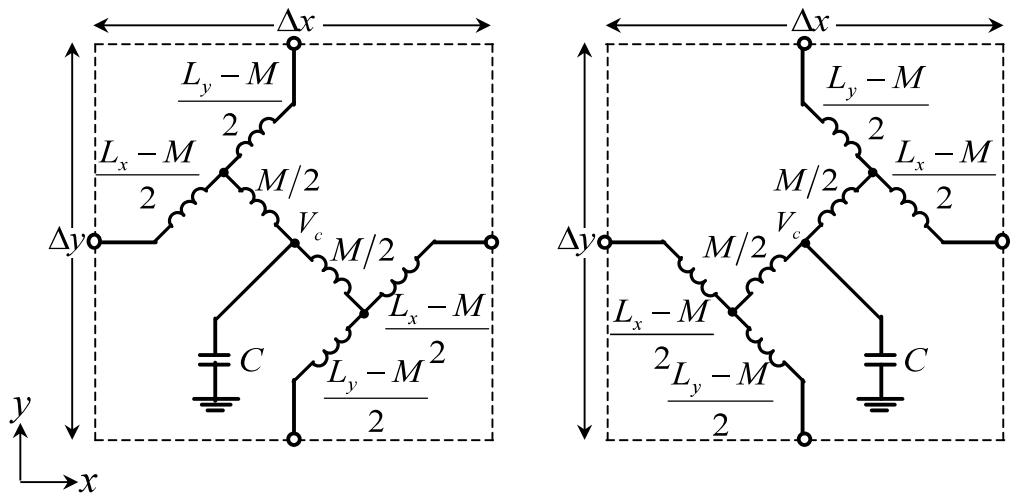

Fig. 4.1 Transformed equivalent circuit models by using T-circuits [74]. (a) For the $\mu_{xy} = \mu_{yx} > 0$ case. (b) For the $\mu_{xy} = \mu_{yx} < 0$ case.

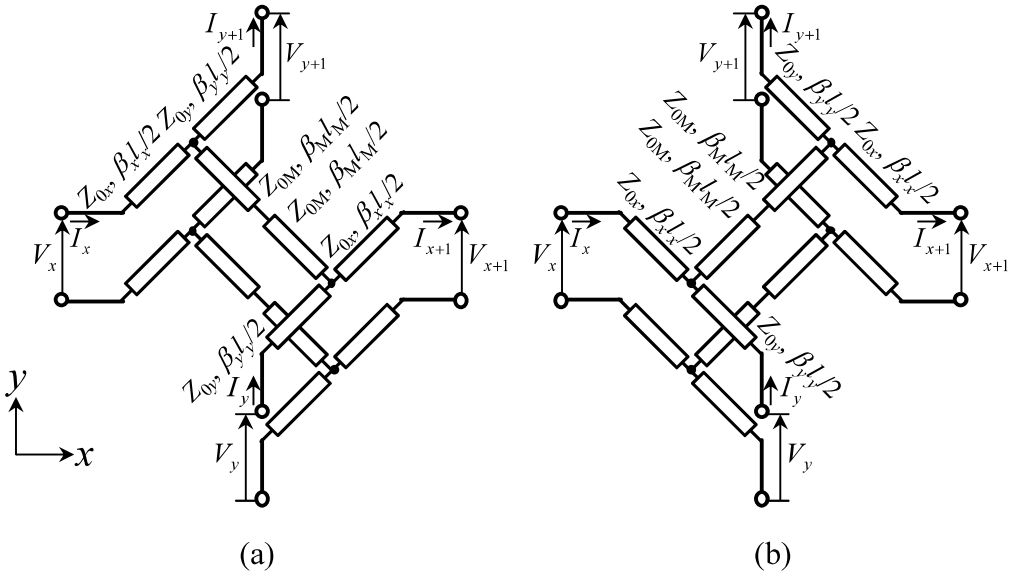

Fig. 4.2 Proposed distributed anisotropic metamaterials [74]. (a) For the $\mu_{xy} = \mu_{yx} > 0$ case. (b) For the $\mu_{xy} = \mu_{yx} < 0$ case.

4.2 Equivalence to the Circuit Model

In order to study the equivalence of the proposed distributed metamaterials and the equivalent circuit models, *Z*-parameters are calculated. First, let us consider the Z-parameters of Fig. 4.2(a). We define the node voltages (V_x, V_{x+1}, V_y, and V_{y+1}) and the currents (I_x, I_{x+1}, I_y, and I_{y+1}) as shown in Fig. 4.2(a), and also define the voltage vector and the current vector as $\boldsymbol{V} = [V_x, V_{x+1}, V_y, V_{y+1}]$ and $\boldsymbol{I} = [I_x, -I_{x+1}, I_y, -I_{y+1}]$. Then, we can obtain the *Z*-parameters

$$\boldsymbol{Z} = \left(Z_{ij}\right), \qquad i, j = 1, 2, 3, \text{ and } 4 \tag{4.1}$$

theoretically by Kirchhoff's voltage and current lows. Not that all of the directions of the currents in the vector $\boldsymbol{I}$ are defined as the directions flowing into the network. From this analysis, we can find the following identities:

$$\begin{aligned} Z_{11} &= Z_{22} \\ Z_{33} &= Z_{44} \\ Z_{14} &= Z_{23} = Z_{32} = Z_{41} \qquad (4.2) \\ Z_{12} &= Z_{21} \\ Z_{34} &= Z_{43} \\ Z_{13} &= Z_{24} = Z_{31} = Z_{42}. \qquad (4.3) \end{aligned}$$

The details for these matrix elements are summarized in Appendix. On the other hand, obtaining the *Z*-parameters of the circuit model in Fig. 3.4(a) with the same manner as

$$\boldsymbol{Z}' = \left(Z'_{ij}\right), \qquad i, j = 1, 2, 3, \text{ and } 4, \tag{4.4}$$

we can also find the following identities:

$$Z'_{11} = Z'_{22}$$

$$Z'_{33} = Z'_{44}$$

$$Z'_{14} = Z'_{23} = Z'_{32} = Z'_{41} \tag{4.5}$$

$$Z'_{12} = Z'_{21} = Z'_{34} = Z'_{43} = Z'_{13} = Z'_{24} = Z'_{31} = Z'_{42}. \tag{4.6}$$

The details for these matrix elements are also summarized in Appendix. Here, it is noted that (4.2) and (4.5) are consistently equivalent for any network parameters in Fig. 4.2(a), whereas (4.3) and (4.6) are not. However, if the condition:

$$\beta_x l_x = \beta_y l_y \,(\equiv \beta l) \tag{4.7}$$

is given, all of the parameters in (4.3) become identical, i.e., $Z_{12} = Z_{21} = Z_{34} = Z_{43} = Z_{13} = Z_{24} = Z_{31} = Z_{42}$, and (4.3) and (4.6) also become equivalent. In this case, $\boldsymbol{Z} = \boldsymbol{Z}'$ holds and the equivalence of the proposed distributed anisotropic metamaterials of Fig. 4.2(a) to the circuit model of Fig. 3.4(a) is guaranteed [74]. Therefore, the proposed distributed metamaterials can be definitely expressed by the circuit model under the condition of (4.7). Incidentally, the equivalence of isomer distributed anisotropic metamaterials of Fig. 4.2(b) to the circuit model of Fig. 3.4(b) can also be shown with the same manner, and its equivalence is guaranteed under the same condition as (4.7).

4.3 Design Formula for Structural Parameters

In the previous section, it has been shown that the equivalence of the proposed distributed anisotropic metamaterials to the circuit model is guaranteed under the condition of (4.7). Therefore, we can safety obtain the design formulas for determining the transmission-line parameters of the distributed anisotropic metamaterials from the circuit parameters of the circuit model. In the following, the material design formulas are derived.

Let us consider equating (4.2) to (4.5) and (4.3) to (4.6) under the condition of (4.7) for the case with Fig. 3.4(a) and Fig. 4.2(a). The relations between the circuit parameters L_x, L_y, M, and C and the transmission-line parameters Z_{0x}, Z_{0y}, $Z_{0\mathrm{M}}$, βl, and $\beta_{\mathrm{M}} l_{\mathrm{M}}$ can be obtained as [74]:

$$L_x - M = \frac{2Z_{0x}}{\omega}\tan\left(\frac{\beta l}{2}\right) \tag{4.8}$$

$$L_y - M = \frac{2Z_{0y}}{\omega}\tan\left(\frac{\beta l}{2}\right) \tag{4.9}$$

$$\begin{aligned} M = 2\Bigg[& Z_{0\mathrm{M}}^2\left(Y_{0x}+Y_{0y}\right)\tan\left(\frac{\beta l}{2}\right) \\ & + Z_{0\mathrm{M}}\left\{\mathrm{cosec}\left(\beta_{\mathrm{M}} l_{\mathrm{M}}\right) - \cot\left(\beta_{\mathrm{M}} l_{\mathrm{M}}\right)\right\}\Bigg] \\ & \Bigg/ \Bigg[\omega\left\{\cos^2\left(\frac{\beta l}{2}\right)\right. \\ & + Z_{0\mathrm{M}}\left(Y_{0x}+Y_{0y}\right)\sin\left(\beta l\right)\cot\left(\beta_{\mathrm{M}} l_{\mathrm{M}}\right) \\ & \left. - Z_{0\mathrm{M}}^2\left(Y_{0x}+Y_{0y}\right)^2\sin^2\left(\frac{\beta l}{2}\right)\right\}\Bigg] \end{aligned} \tag{4.10}$$

$$\begin{aligned} C = \frac{1}{\omega}\Bigg\{ & \left(Y_{0x}+Y_{0y}\right)\sin\left(\beta l\right)\cos\left(\beta_{\mathrm{M}} l_{\mathrm{M}}\right) \\ & + Y_{0\mathrm{M}}\cos^2\left(\frac{\beta l}{2}\right)\sin\left(\beta_{\mathrm{M}} l_{\mathrm{M}}\right) \\ & - Z_{0\mathrm{M}}\left(Y_{0x}+Y_{0y}\right)^2\sin^2\left(\frac{\beta l}{2}\right)\sin\left(\beta_{\mathrm{M}} l_{\mathrm{M}}\right)\Bigg\} \end{aligned} \tag{4.11}$$

By solving (4.8)–(4.11) simultaneously, we can determine Z_{0x}, Z_{0y}, $Z_{0\mathrm{M}}$, βl, and $\beta_{\mathrm{M}} l_{\mathrm{M}}$ from given L_x, L_y, M, and C with one degree of freedom, i.e., one of the transmission-line parameters can be chosen arbitrary. On the other hand, for the case with Fig. 3.4(b) and Fig. 4.2(b), the same formulas as (4.8)–(4.11) are obtained with the same manner. Therefore, these design formulas can be applied to both cases of $\mu_{xy} = \mu_{yx}$

> 0 and $\mu_{xy} = \mu_{yx} < 0$. For example, if $\mu_{xy} = \mu_{yx} > 0$, Fig. 4.2(a) with $M = \mu_{xy}\Delta d = \mu_{yx}\Delta d$ (> 0) should be used, and if $\mu_{xy} = \mu_{yx} < 0$, Fig. 4.2(b) with $M = \mu_{xy}\Delta d = \mu_{yx}\Delta d$ (> 0) should be used.

Incidentally, if the frequency approaches to zero in (4.8), by approximating $\tan x \approx x$, design formulas can be expressed as [74]:

$$\begin{aligned} L_x - M &= \frac{2Z_{0x}}{\omega}\tan\left(\frac{\beta l}{2}\right) \to \frac{2Z_{0x}}{\omega}\frac{\beta l}{2} = Z_{0x}\frac{\beta l}{\omega} \\ &= \sqrt{\frac{L_{0x}}{C_{0x}}}\sqrt{L_{0x}C_{0x}} \\ &= L_{0x} \end{aligned} \tag{4.12}$$

where L_{0x} and C_{0x} are the equivalent inductance and capacitance values of the corresponding transmission-line section with the characteristic impedance Z_{0x} in Fig. 4.2. Therefore, L_x approaches to the frequency independent value. Similarly, by approximating $\sin x = \tan x \approx x$ and $\cos x \approx 1$, it can also be shown that L_y, M, and C approach to frequency independent value as:

$$L_y - M \to L_{0y} \tag{4.13}$$

$$M \to L_{0\mathrm{M}}\frac{C_{0x} + C_{0y}}{C} \tag{4.14}$$

$$C \to C_{0x} + C_{0y} + C_{0\mathrm{M}} \tag{4.15}$$

where (L_{0y}, C_{0y}) and ($L_{0\mathrm{M}}$, $C_{0\mathrm{M}}$) are the equivalent inductance and capacitance values of the corresponding transmission-line sections with the characteristic impedance Z_{0y} and $Z_{0\mathrm{M}}$ in Fig. 4.2, respectively. From these results, it can be seen that the proposed distributed anisotropic metamaterials essentially operate as the lumped element circuits in Fig. 3.4 at lower frequencies down to DC. Therefore, the bandwidth is limited only

by the upper frequency of operation.

4.4 Carpet Cloak Design

In order to confirm the validity of the proposed anisotropic metamaterials, a carpet cloak of invisibility is designed by using the distributed anisotropic metamaterials. The equivalent circuit parameters L_x, L_y, M, and C in Fig. 3.4 for the carpet cloak calculated in Section 3.4 are used. In this section, the transmission-line parameters in Fig. 4.2 for the carpet cloak are calculated by using the calculated circuit parameters.

By solving (4.8)–(4.11) simultaneously with the parameter $Z_{0\mathrm{M}}/\eta$ = 1.5 ($\eta = \sqrt{\mu/\varepsilon}$ is the wave impedance in the original area), which is chosen as a degree of freedom, we determine Z_{0x}, Z_{0y}, βl, and $\beta_{\mathrm{M}} l_{\mathrm{M}}$ from calculated L_x, L_y, M, and C in Fig. 3.7. Figs. 4.3(a) and (b) show the obtained characteristic impedances Z_{0x} and Z_{0y} normalized by η, and Figs. 4.3(c) and (d) show the obtained electrical lengths βl and $\beta_{\mathrm{M}} l_{\mathrm{M}}$ normalized by $k\Delta d$ ($k = \omega\sqrt{\varepsilon\mu}$ is the wavenumber in the original area). Here, for the half area of $x < 0$, the distributed anisotropic metamaterial of Fig. 4.2(a) is used as the unit cell since $\mu_{xy} = \mu_{yx} > 0$ according to (2.3). On the other hand, for the half area of $x >0$, Fig. 4.2(b) is used as the unit cell since $\mu_{xy} = \mu_{yx} < 0$. From Figs. 4.3(a) and (b), it is seen that Z_{0x}/η and Z_{0y}/η take minimum and maximum at the center of the area (x, y) = (0, y), respectively. These tendencies are the same as L'_x/μ_0 and L'_y/μ_0 in Fig. 3.7(a) and (b) since (4.8) and (4.9) hold, respectively. Besides, from Fig. 4.3(c), it is seen that $\beta l/k\Delta d$ takes maximum at the center of the area (0, y). In addition, from Fig. 4.3(d), it is seen that $\beta_{\mathrm{M}} l_{\mathrm{M}}/k\Delta d$ takes 0 value at the center, top, and both sides of the area (0, y), (x, h), and ($\pm p$, y), respectively. These tendencies are the same as M'/μ_0 in Fig. 3.7(c) since (4.10) holds, and the off-diagonal components of the permeability tensor can be

determined with this value including Z_{0M}/η. Incidentally, the permittivity ε_z is implicitly determined by all of the values in Fig. 4.3 since (4.11) holds.

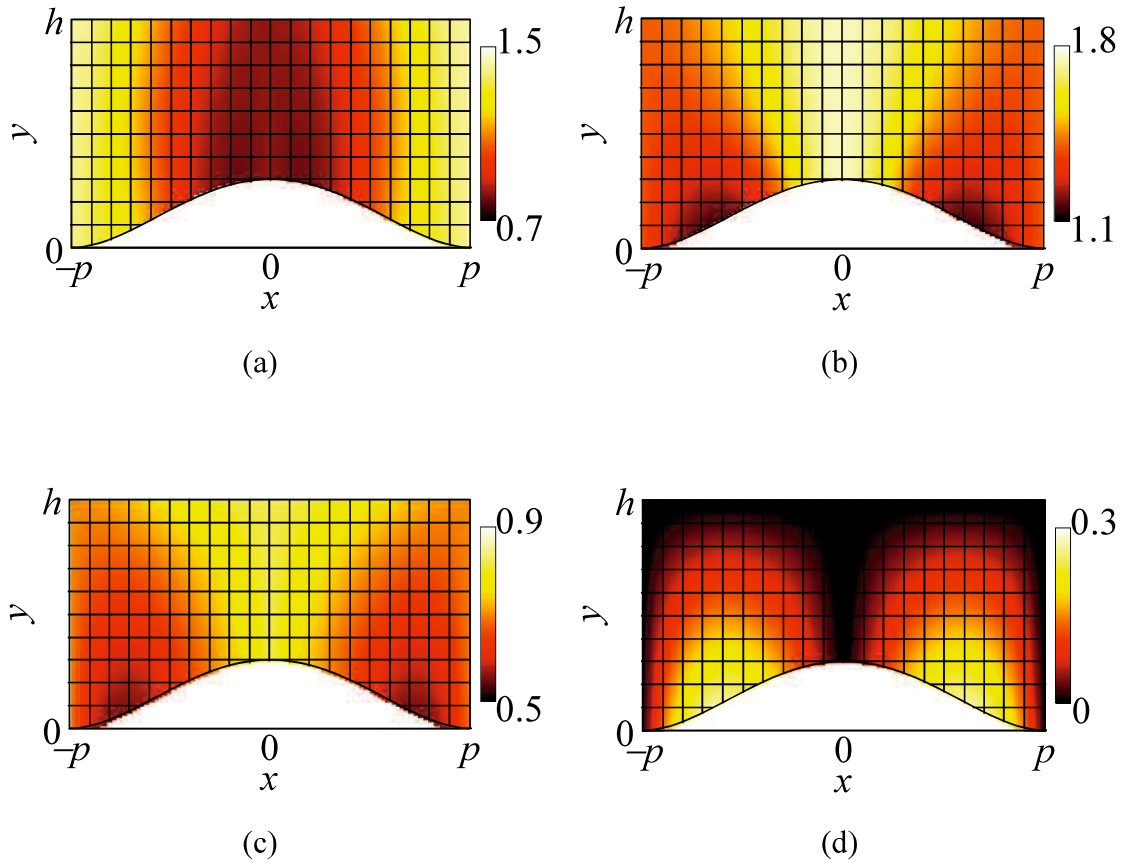

Fig. 4.3 Transmission-line parameters of the distributed anisotropic metamaterials in Fig. 4.2 for the carpet cloak design. The unit cell of Fig. 4.2(a) is used for the half area of $x < 0$, and Fig. 4.2(b) is used for the half area of $x > 0$. (a) Normalized characteristic impedance Z_{0x}/η. (b) Normalized characteristic impedance Z_{0y}/η. (c) Normalized electrical length $\beta l/k\Delta d$. (d) Normalized electrical length $\beta_M l_M/k\Delta d$. Here, we chose $Z_{0M}/\eta = 1.5$ as a degree of freedom.

4.5 Circuit Simulations

In order to validate the carpet cloak design, circuit simulations are carried out with a SPICE simulator.

First, we prepare the same node list of 20 × 10 cells as in Fig. 3.8(a). Here, for the left half area of Fig. 3.8(a), the unit cell of Fig. 4.2(a) is used, and for the right half area, the unit cell of Fig. 4.2(b) is used. The transmission-line is dealt as an ideal transmission-line, and the transmission-line parameters for each unit cell are given from the values in Figs. 4.3(a)–(d). Then, we put the carpet cloak at the bottom center of the isotropic area in Fig. 3.8(b). In the isotropic area, the unit cell of Fig. 4.4 is used. The characteristic impedance and the electrical length for both the x- and y- branches in Fig. 4.4 are $Z_{0x} = Z_{0y} = \sqrt{2}\,\eta$ and βl $(= \beta_x l_x = \beta_y l_y) = k\Delta d/\sqrt{2}$, respectively, taking into account the effect of 2-D transmission-line networks [65], [66], [68]. In the following design, the refractive index and the wave impedance of isotropic area are chosen to be $n = k/k_0 = 2.14$ (k_0 is the wavenumber in vacuum) and $\eta = 63.6\ \Omega$, respectively considering a convenience of realization.

According to the circuit simulation in Section 3.5, fifty in-phase voltage sources ($n_s = 50$) with the internal impedance of 62Ω, which is reasonably close to the wave impedance $\eta = 63.6\ \Omega$ are connected at the top row to illuminate the bump with a normal incident beam ($\theta_{inc} = 0$ deg). The amplitudes of the voltage sources are set to form the Gaussian beam with the beam waist of $10\Delta d$. Nodes on the bottom boundary including the bump area are short-circuited. On the other hand, the other nodes on the top row and the side columns are terminated by 62Ω resistors according to the determined wave impedance in the isotropic area.

The complex voltage distributions of the center nodes in all unit cells are calculated.

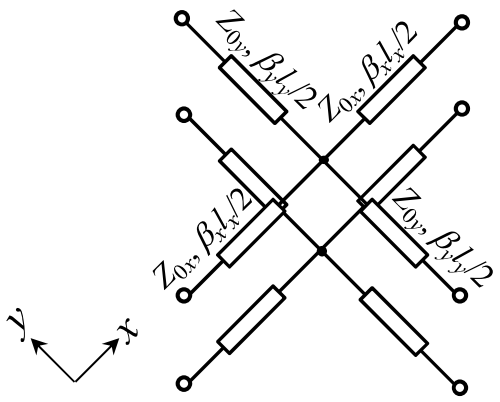

Fig. 4.4 Unit cell for the isotropic area.

For comparison, two simulations for a flat floor and a bump without the carpet cloak are also carried out. Here, although the settings of the circuit simulations are the same as in Section 3.5, the unit cell of Fig. 4.4 is used in place of the unit cell of Fig, 3.3(a).

Figs. 4.5(a)–(c) show calculated complex voltage distributions for the cases with (a) the carpet cloak, (b) a flat floor, and (c) a bump without the carpet cloak, respectively. Here, the wavelength is chosen as $\lambda_g = 12\Delta d$. By comparing Figs. 4.5(a) with (b), it is seen that the carpet cloak sufficiently mimics reflections from the flat floor. Besides, by comparing Figs. 4.5(a) with (c), it is clearly seen that scattered waves by the bump are considerably suppressed by the carpet cloak. In addition, it is also noted that these results are almost the same as those in Fig. 3.10(a)-(c).

Figs. 4.6(a)–(c) show similar results for the case with the shorter wave length $\lambda_g = 6\Delta d$. From these results, it is seen that similar results of Fig. 3.11(a)-(c) are obtained, and the carpet cloak suppresses scattered waves from the bump and mimic the flat floor, though the level of scattered waves is slightly increased (compare Fig. 4.6 (a) with Fig. 4.5 (a)). Incidentally, from the discussions in the previous section, it is expected for the carpet cloak to work also at lower frequencies down to DC according to (4.12)-(4.15).

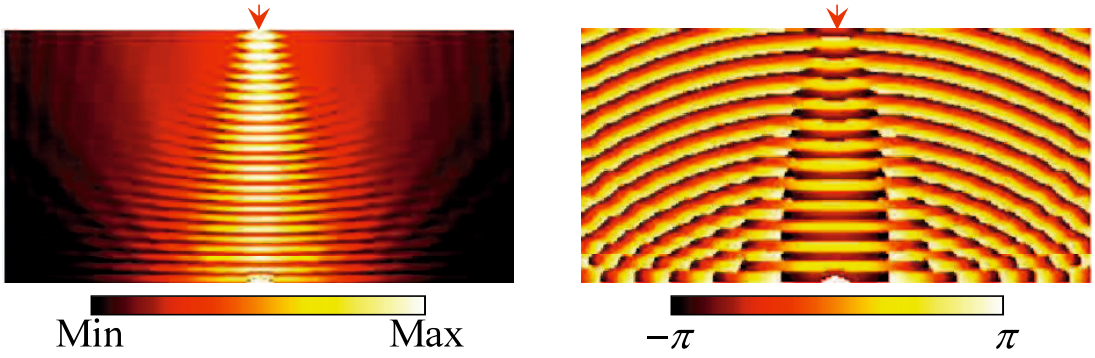

(a)

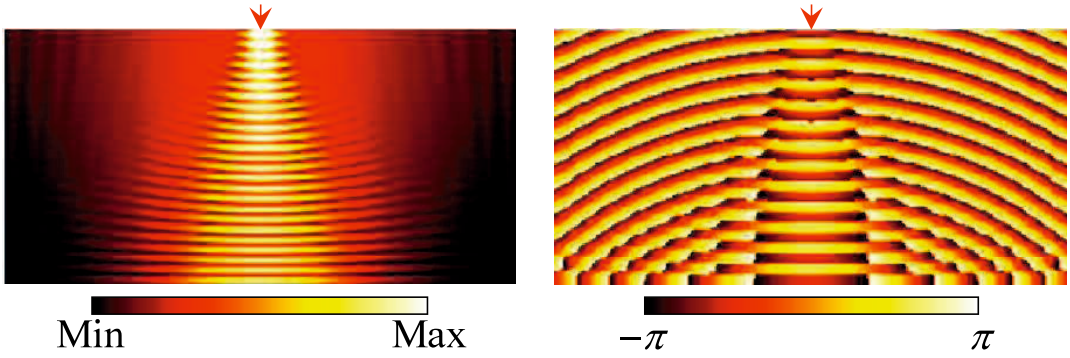

(b)

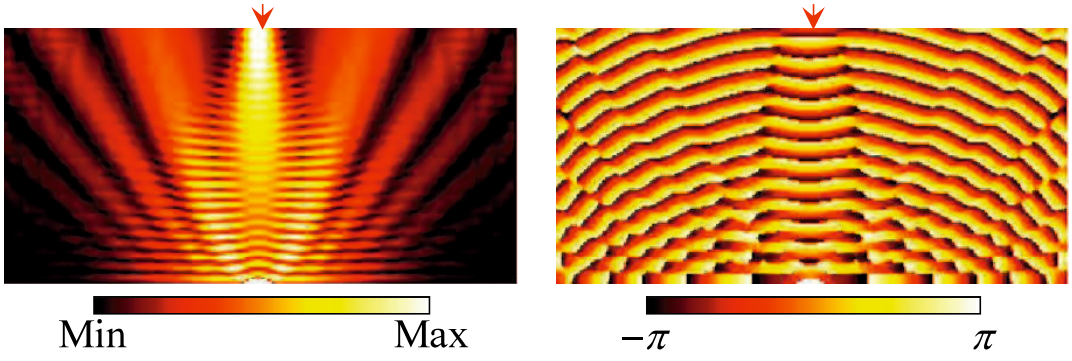

(c)

Fig. 4.5 Calculated complex voltage distributions (λ_g = 12Δd). Left and right figures are amplitude and phase, respectively. (a) Carpet cloak. (b) Flat floor. (c) Bump without the carpet cloak.

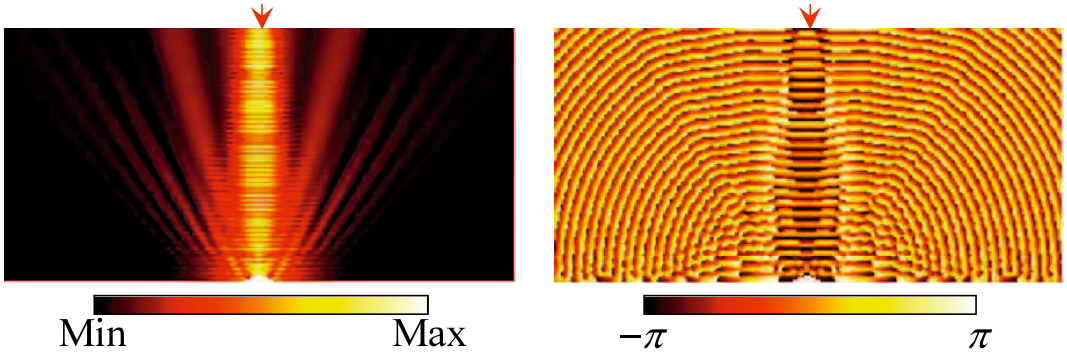

(a)

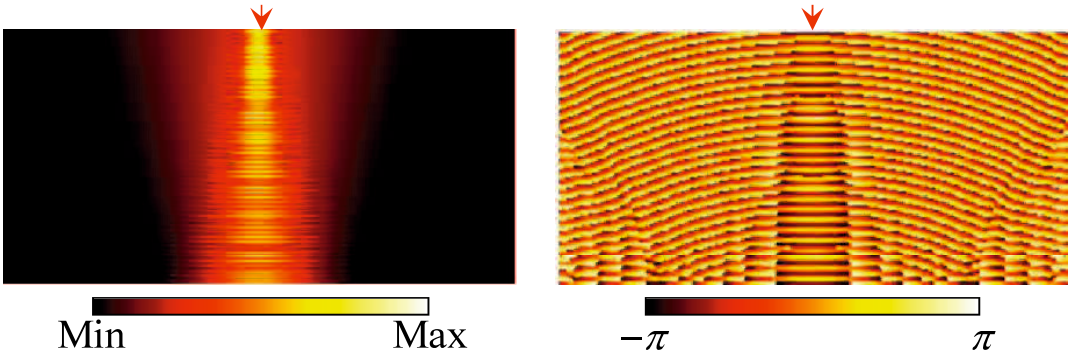

(b)

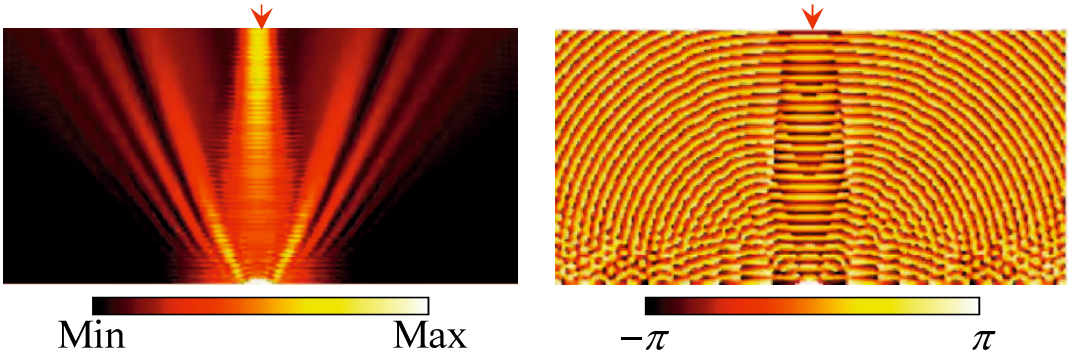

(c)

Fig. 4.6 Calculated complex voltage distributions ($\lambda_g = 6\Delta d$). Left and right figures are amplitude and phase, respectively. (a) Carpet cloak. (b) Flat floor. (c) Bump without the carpet cloak.

In order to further confirm the operation of the carpet cloak, circuit simulations for the oblique incident cases (θ_{inc} = 30, 45, and 60 deg) are also carried out. All configurations of these circuit simulations are almost the same as those in Section 3.5, except for the fact in which the unit cell of Fig. 4.2 and Fig.4.3 are used in the anisotropic and isotropic area, respectively. In addition, 62Ω resistors are connected at the nodes excluding the bottom boundary in place of the used them in Section 3.5 according to the determined wave impedance in the isotropic area.

Figs. 4.7–4.9 show the calculated complex voltage distributions for the cases with θ_{inc} = 30, 45, and 60 deg, respectively. In these figures, the calculated results for the cases with (a) the carpet cloak, (b) a flat floor, and (c) a bump without the carpet cloak are also shown. Here, the wavelength is chosen as $\lambda_g = 12\Delta d$. From these figures, it is seen that the carpet cloak with the distributed anisotropic metamaterials works well even with the oblique incident cases.

From these results, it can be concluded that the validity of the proposed distributed anisotropic metamaterials and operations of the carpet cloak with the distributed anisotropic metamaterials are confirmed by circuit simulations.

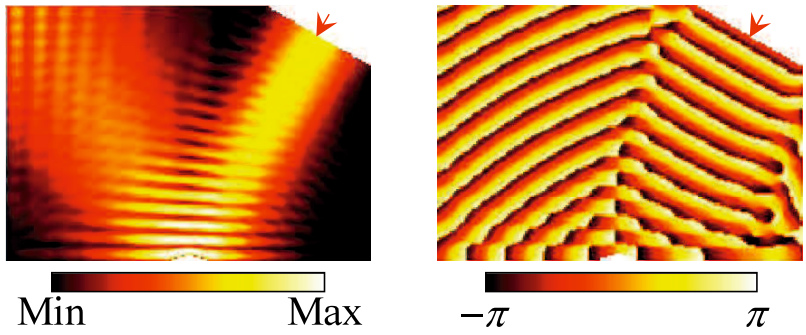

(a)

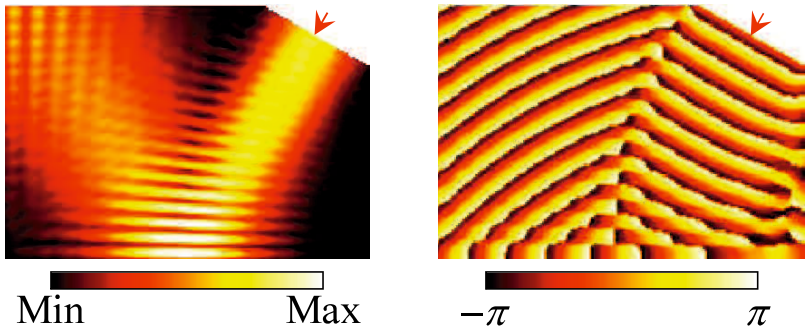

(b)

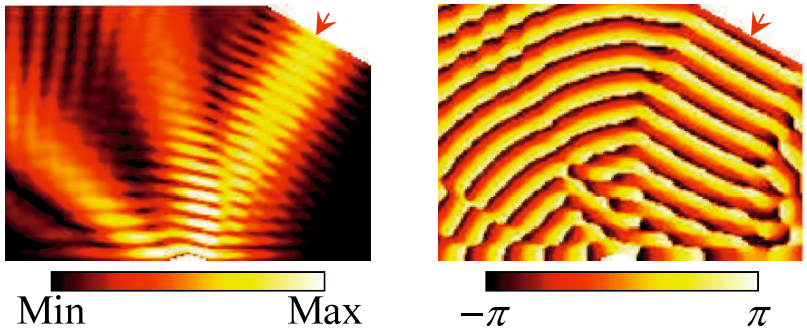

(c)

Fig. 4.7 Calculated complex voltage distributions for the case with θ_{inc} = 30 deg ($\lambda_g = 12\Delta d$). Left and right figures are amplitude and phase, respectively. (a) Carpet cloak. (b) Flat floor. (c) Bump without the carpet cloak.

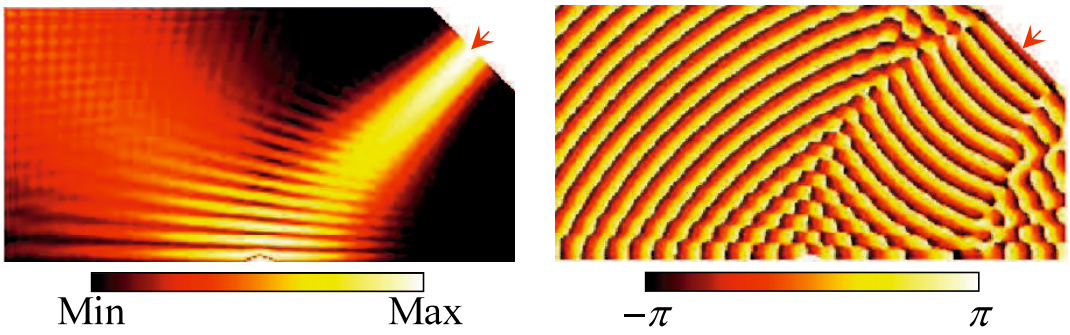

(a)

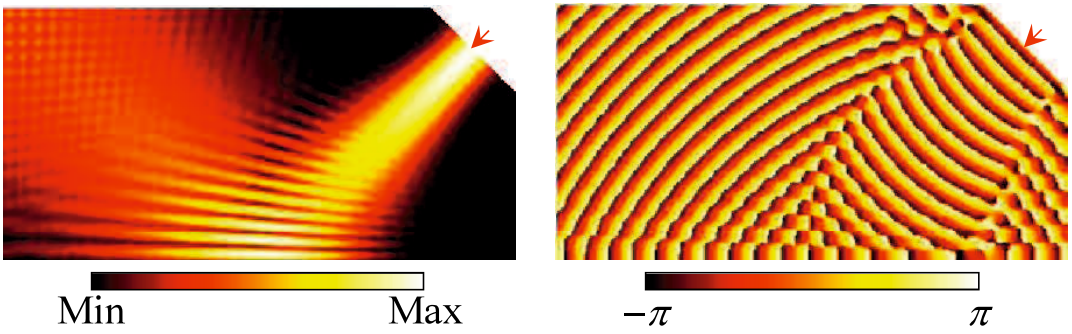

(b)

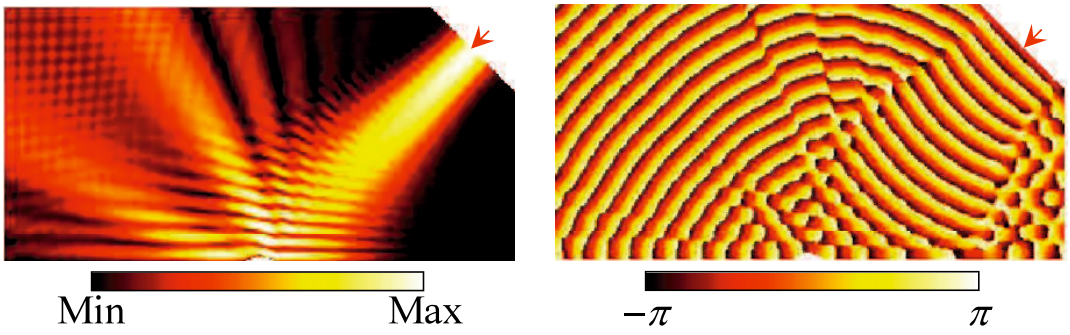

(c)

Fig. 4.8 Calculated complex voltage distributions for the case with θ_{inc} = 45 deg ($\lambda_g = 12\Delta d$). Left and right figures are amplitude and phase, respectively. (a) Carpet cloak. (b) Flat floor. (c) Bump without the carpet cloak.

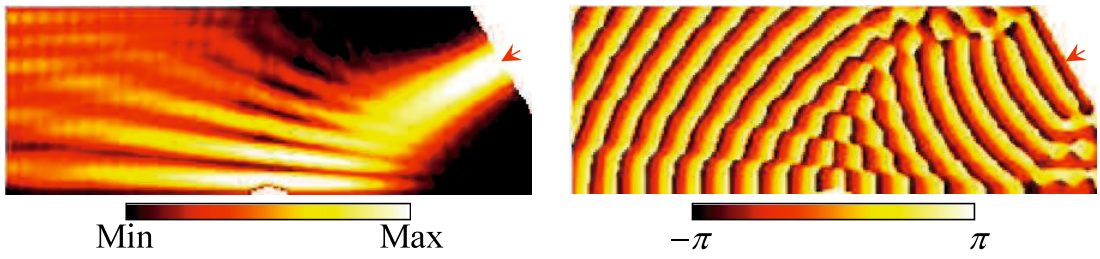

(a)

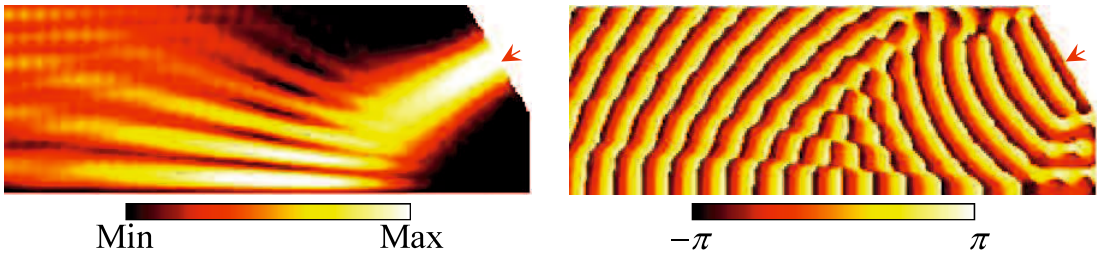

(b)

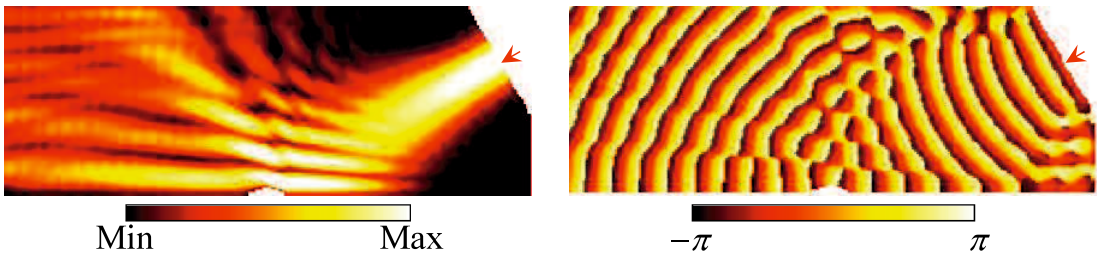

(c)

Fig. 4.9 Calculated complex voltage distributions for the case with $\theta_{\mathrm{inc}} = 60$ deg ($\lambda_g = 12\Delta d$). Left and right figures are amplitude and phase, respectively. (a) Carpet cloak. (b) Flat floor. (c) Bump without the carpet cloak.

Chapter 5 Carpet Cloak Implementation and Demonstrations

In this chapter, in order to confirm the validity of the design theory with the distributed anisotropic metamaterials, the carpet cloak designed in the previous chapter is implemented, and its operations are demonstrated [74]. First, the designed carpet cloak is implemented on a dielectric substrate with microstrip-line technology considering easy design and fabrication. Secondly, electric near-field measurements are carried out and operations of the implemented carpet cloak are verified experimentally.

5.1 Carpet Cloak Implementation with Microstrip-Line Technology

Let us consider implementing the anisotropic unit cell of Fig. 4.2. Fig. 5.1 shows the schematic of the unit cell of anisotropic metamaterials implemented on a dielectric substrate with microstrip-line technology [74]. Figs. 5.1(a) and (b) are for $\mu_{xy} = \mu_{yx} > 0$ and for $\mu_{xy} = \mu_{yx} < 0$, respectively. They consist of five transmission-line sections of three different kinds of parameters (width, length) = (W_x, l_x), (W_y, l_y), and (W_M, l_M). The transmission-line section of (W_M, l_M) affects the off-diagonal components of permeability tensor since this directly corresponds to the transmission-line section of (Z_{0M}, $\beta_M l_M$) in Fig. 4.2. The length of each line section is controlled by the curvature R of the right angle sector. The total lengths l_x, l_y, and l_M are defined along the center. The substrate is backed by a metallic ground plane.

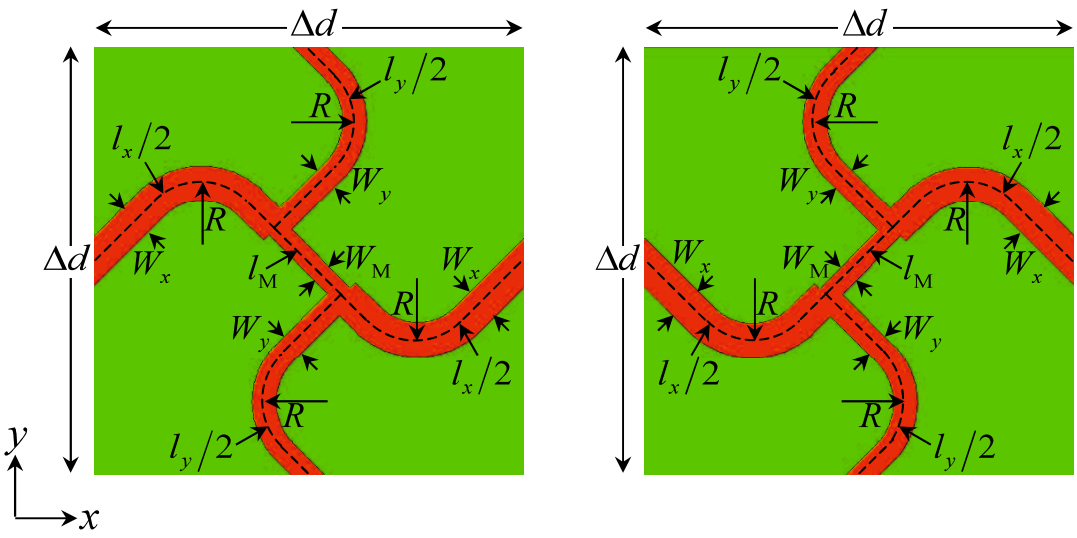

(a) (b)

Fig. 5.1 Schematics of the unit cells of the anisotropic metamaterials implemented on a dielectric substrate with microstrip-line technology [74]. (a) For the $\mu_{xy} = \mu_{yx} > 0$ case. (b) For the $\mu_{xy} = \mu_{yx} < 0$ case. The substrate is backed by a metallic ground plane.

Then, we determine the parameters of W_x, W_y, W_M, l, l_M in Fig. 5.1 for implementing the carpet cloak designed in the previous chapter. Here, we choose an ARLON DiClad880 with permittivity $\varepsilon_r = 2.17$, thickness $t = 0.254$ mm, and dielectric loss tan $\delta = 0.00085$ as a dielectric substrate. In addition, the width and the height of the carpet cloak area in Fig. 3.6(b) and the height of the bump under the carpet cloak are chosen to be $2p = 100$ mm, $h = 50$ mm, and $A = 0.3h = 15$ mm, respectively, and the carpet cloak is discretized with $\Delta d = 5$ mm. The total number of unit cells in the carpet cloak area is 20 × 10 cells which is the same as those in Fig. 3.8(a). We choose the effective impedance $\eta = 63.6\ \Omega$, the phase velocity $v_p = c_0/n$ (c_0 is the speed of light and $n = 2.14$)

of the medium in the isotropic area outside of the carpet cloak area corresponding to the original coordinate system to be mimicked. In addition, those values are determined by considering fabrication constraints in which the minimum line width is 0.1 mm and all of the lines have to be accommodated in the unit cell. Under these conditions, we calculated the parameters of W_x, W_y, W_M, l_x, l_y, and l_M from the calculated characteristic impedances and electrical lengths in Fig. 4.3 by assuming $\beta_x/k = \beta_y/k = \beta_M/k = 0.615$. Figs. 5.2(a)–(d) show the calculated W_x, W_y, l_x, l_y, and l_M. Here, for the half area of $x < 0$, the unit cells of Fig. 5.1(a) is used since $\mu_{xy} = \mu_{yx} > 0$, and for the half area of $x > 0$, the unit cells of Fig. 5.1(b) is used since $\mu_{xy} = \mu_{yx} < 0$. Besides, the parameter W_M is chosen to be 0.231 mm from $Z_{0M} = 1.5\eta$ chosen as a degree of freedom.

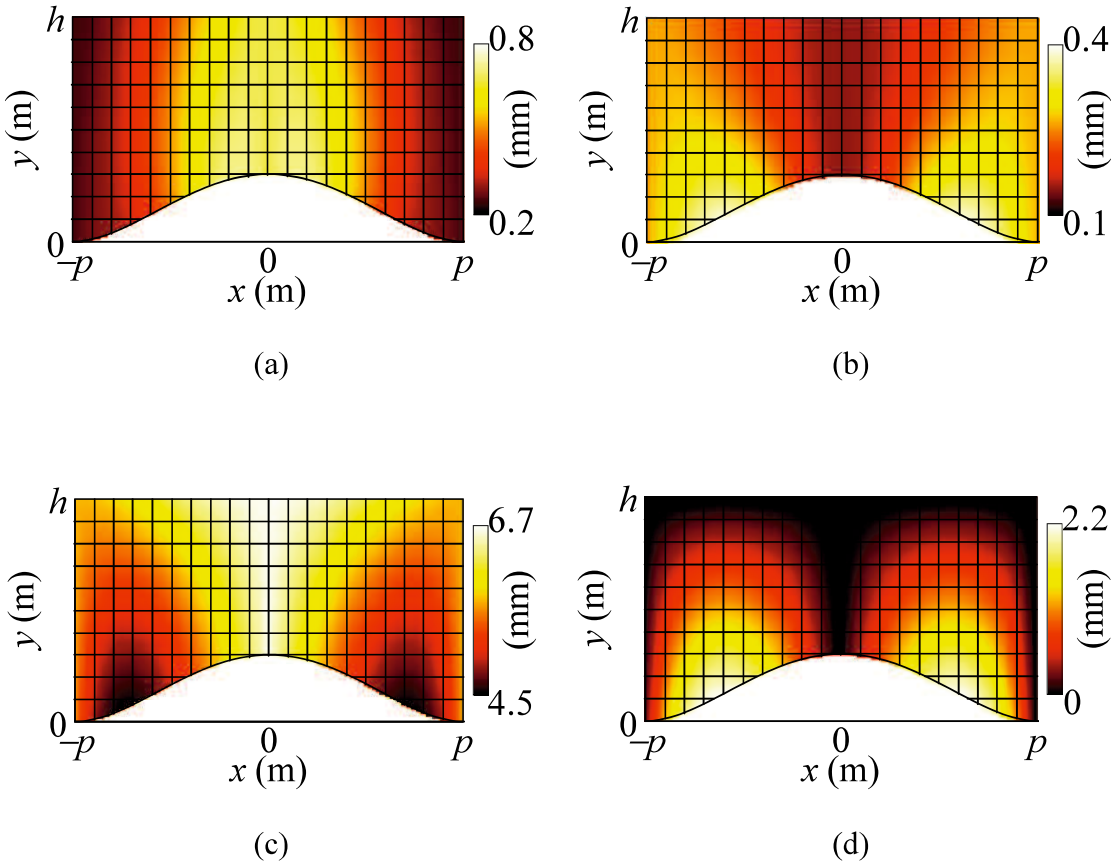

Fig. 5.2 Line widths and lengths of the implemented anisotropic unit cells in Fig. 5.1 for the carpet cloak design. The unit cells of Figs. 5.1(a) and (b) with Δd = 5 mm are used for the half area of $x < 0$ and $x > 0$, respectively. The width and the height in the carpet cloak area and the height of the bump under the carpet cloak are chosen to be $2p$ = 100 mm, h = 50 mm, and $A = 0.3h$ = 15 mm, respectively. (a) Line width W_x. (b) Line width W_y. (c) Line length $l_x = l_y$. (d) Line length l_M. W_M is chosen to be 0.231 mm.

From given the determined parameters in Fig. 5.2, we implemented the carpet cloak on a dielectric substrate. Fig. 5.3 shows the implemented carpet cloak. As seen in the figure, the carpet cloak is symmetrical with the center of $x = 0$, and the branches of the unit cells at the interface on $x = 0$ are connected smoothly maintaining the electrical length. Besides, Fig. 5.4 shows the schematic of the carpet cloak for fabrication. As seen in this figure, the implemented carpet cloak in Fig. 5.3 is placed into the bottom center of the isotropic area discretized with 56 × 40 cells (280 × 200 mm^2 due to $\Delta d = 5$ mm) shown in Fig. 5.5. Although, Fig. 5.5(a) and (b) are electrically identically, they are used in the left- and right-half of the isotropic area, respectively, for matching the geometry. The unit cell parameters for the isotropic area are chosen to be $W_x = W_y = 0.264$ mm and

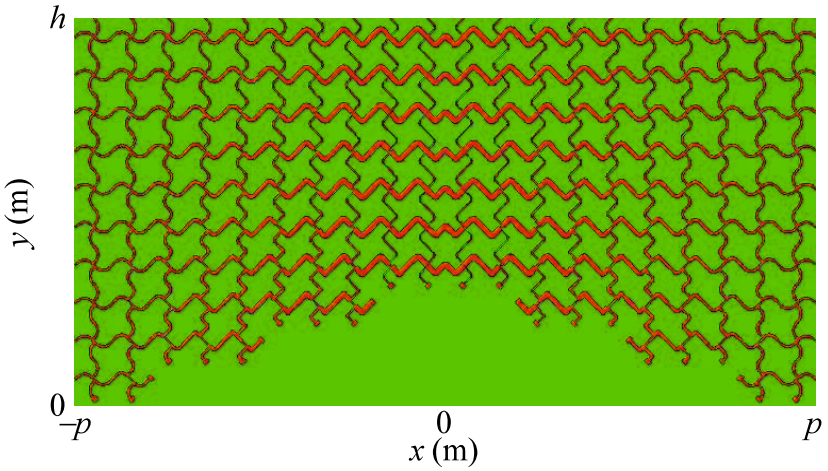

Fig. 5.3 Implemented carpet cloak with 20 × 10 unit cells ($2p \times h$ = 100 × 50 mm^2). The unit cells of Figs. 5.1(a) and (b) with $\Delta d = 5$ mm are used for the half area of $x < 0$ and $x > 0$, respectively. All line widths and lengths are determined from Figs. 5.2(a)–(d). The branches of the unit cells at the interface on $x = 0$ are connected smoothly maintaining the electrical length.

$l(= l_x = l_y)$ = 5.75 mm according to the determined refractive index n = 2.14 and the wave impedance η = 63.6 Ω.

For comparison, two cases for a flat floor (see Fig. 5.6(a)) and a bump without the carpet cloak (see Fig. 5.6(b)) are also implemented on a dielectric substrate. Here, Fig. 5.6(a) and (b) are used in place of the carpet cloak on the bottom center in Fig. 5.4.

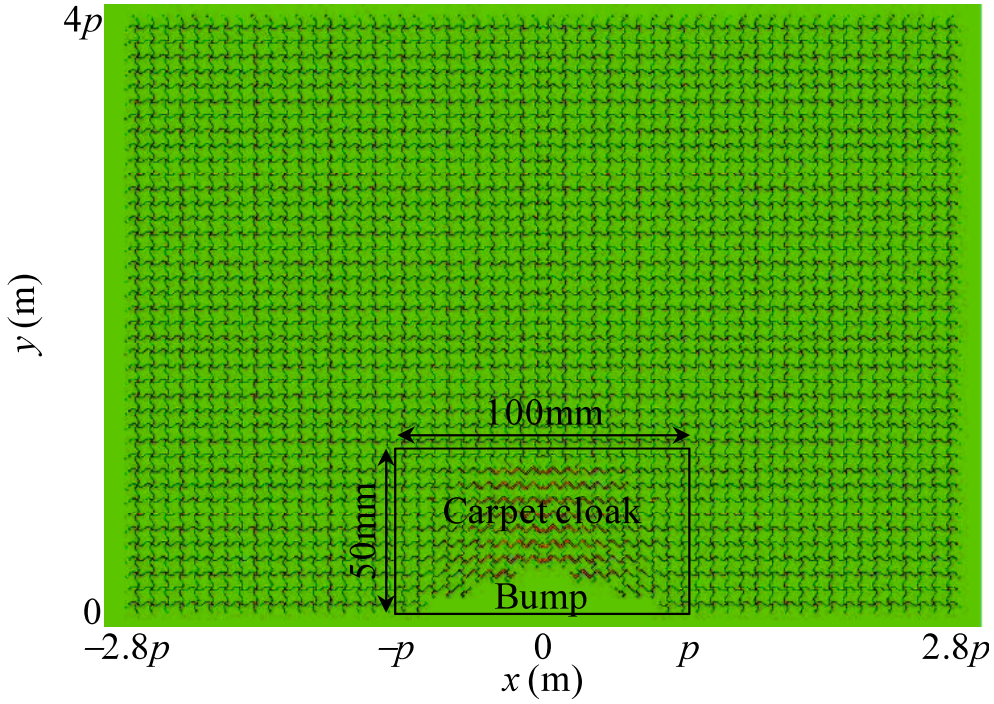

Fig. 5.4 Schematic for the prototype with 56 × 40 cells (5.6p × 4p = 280 × 200 mm^2). The implemented carpet cloak in Fig. 5.3 is placed at the bottom center of the area.

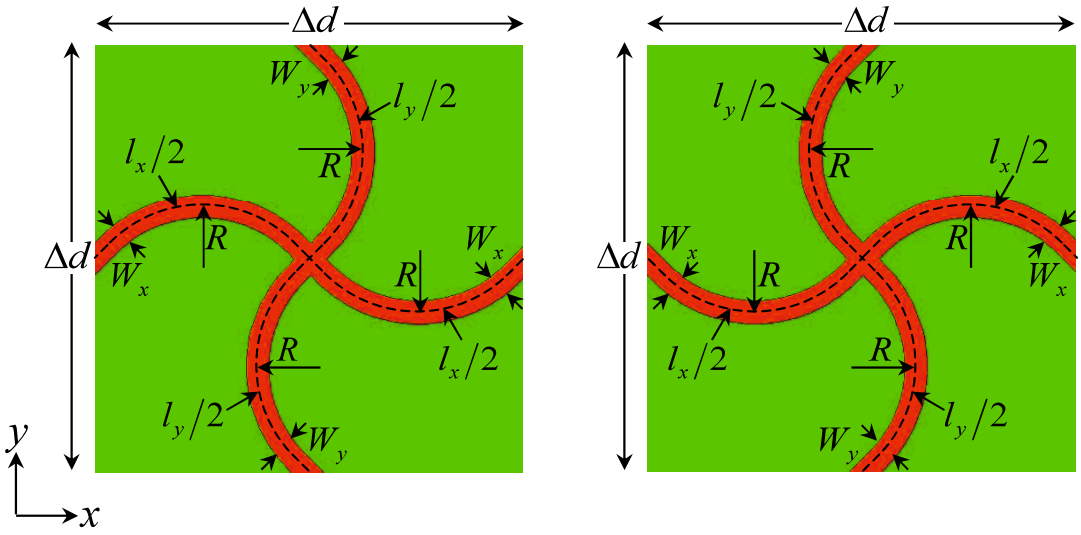

Fig. 5.5 Schematics of the unit cells of the isotropic area outside of the carpet cloak area. (a) For the left-half area of Fig. 5.4. (b) For the right-half area of Fig. 5.4. The substrate is backed by a metallic ground plane.

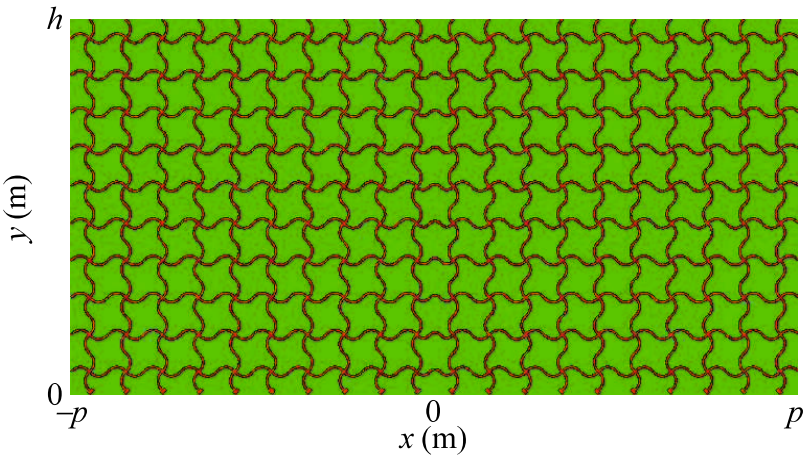

(a)

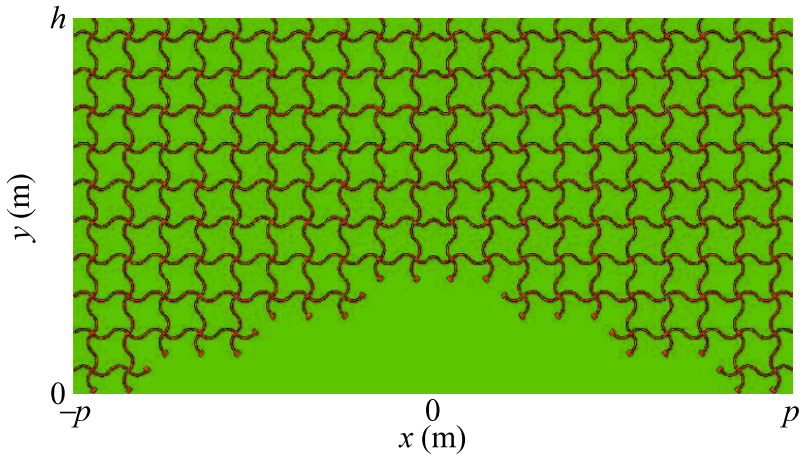

(b)

Fig. 5.6 Implemented a flat floor and a bump without the carpet cloak with 20 × 10 unit cells ($2p \times h = 100 \times 50$ mm^2). The isotropic unit cells of Figs. 5.5(a) and (b) with $\Delta d = 5$ mm are used for the half area of $x < 0$ and $x > 0$, respectively. The line widths and lengths are chosen to be $W_x = W_y = 0.264$ mm and $l(= l_x = l_y) = 5.75$ mm, respectively. The branches of the unit cells at the interface on $x = 0$ are connected smoothly maintaining the electrical length. (a) Flat floor. (b) Bump without the carpet cloak. These are placed into the carpet cloak area in Fig. 5.4.

5.2 Prototypes for Experiments

Fig. 5.7(a) shows the fabricated prototype for the carpet cloak corresponding to Fig. 5.4. In addition, Fig. 5.7(b) and (c) also show fabricated another two prototypes for a flat floor and a bump without the carpet cloak, respectively for comparison. All prototypes are fabricated with lithography. All the metallic parts are made of cupper plated by gold. The nodes on the bottom boundary including the bump area are short-circuited by through-hole vias with the diameter of ϕ = 0.3 mm. The other nodes are terminated by 62 Ω chip resistors with through metallic lands with 0.8 × 0.5 mm^2. The resistance value of 62 Ω is reasonably close to the wave impedance η = 63.6 Ω.

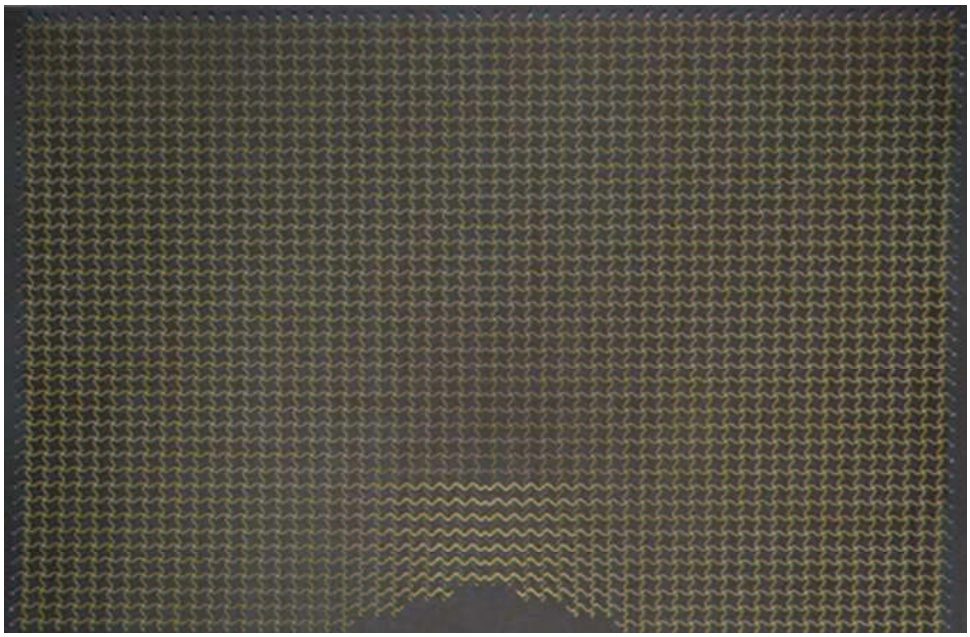

Fig. 5.7 Prototype of the carpet cloak.

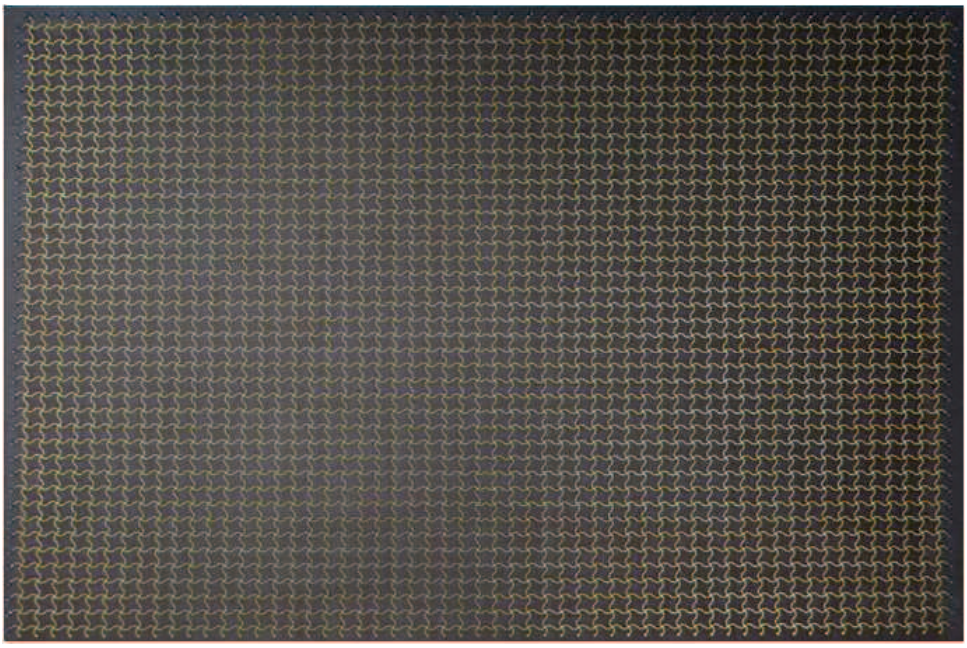

Fig. 5.8 Prototype of a flat floor.

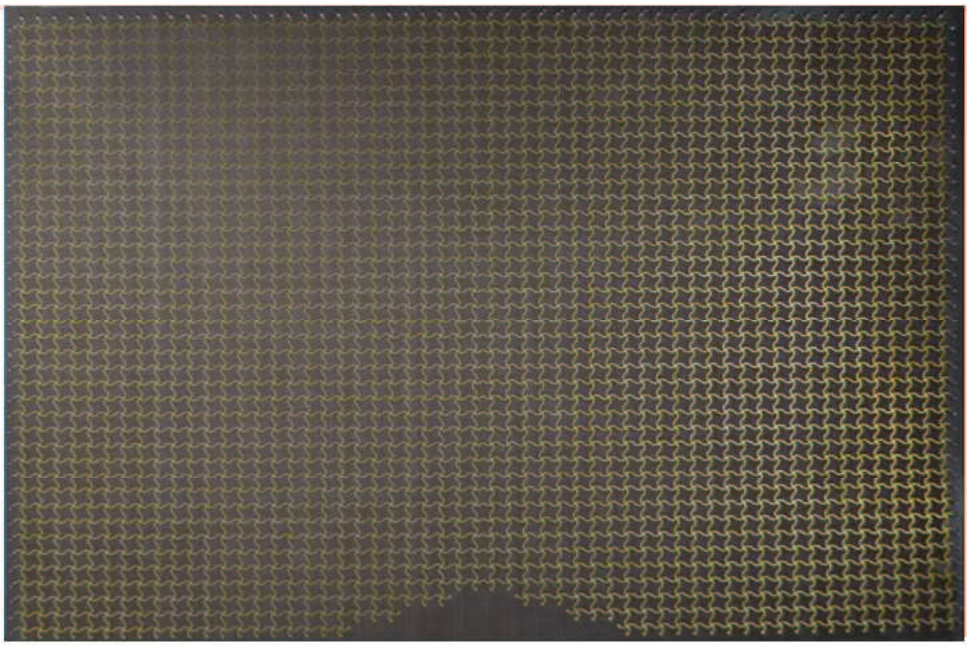

Fig. 5.9 Prototype of a bump without the carpet cloak.

5.3 Near-Field Measurement System

In order to confirm operations of the fabricated carpet cloak, electric near-field measurements are carried out.

Fig. 5.10 shows the electric near-field measurement system used in the experiments. For avoiding warp and keeping flatness of the prototype, an adhesive sheet is put on an aluminum plate, and the prototype is fixed on the adhesive sheet. A coaxial cable is soldered at the center node on the top row, and electromagnetic waves are excited from the point. Then, distributions of the z-component of the electric near-field approximately 0.5 mm above the prototype surface are measured by using a coaxial probe with a computer controlled *xyz*-stage. The total measurement area is 275 × 190 mm^2, and the complex electric field data are acquired in every 1.25 mm both in the *x*-

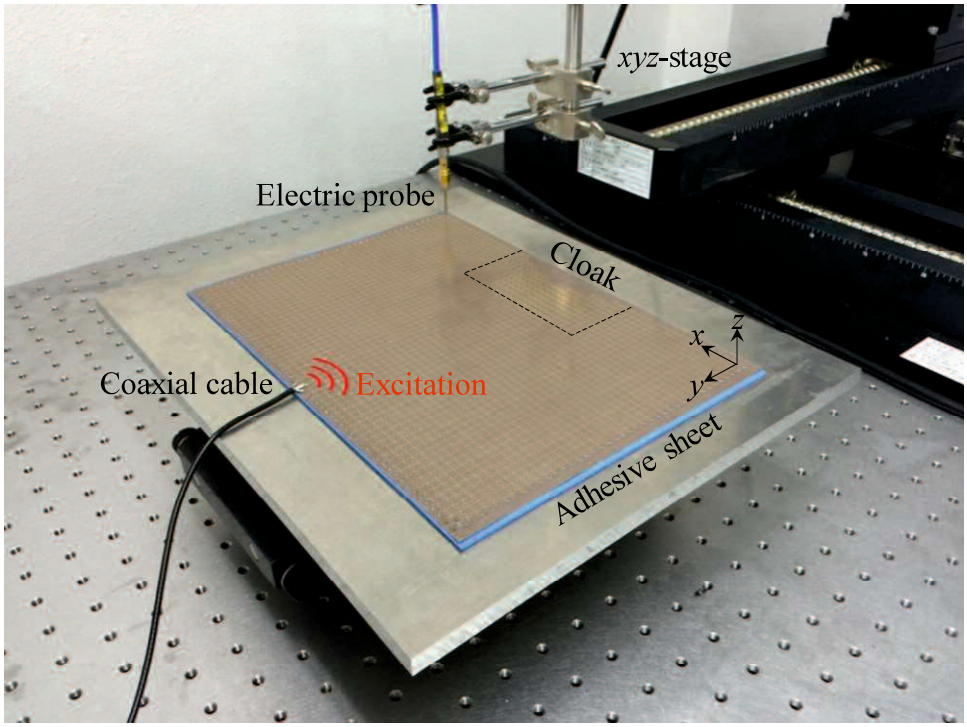

Fig. 5.10 Electric near-field measurement system.

and y-directions. The total number of the measurement points is 221 × 153. Here, in order to suppress the direct coupling between the coaxial cable for the excitation and the electric probe, the differential measurement technique is used, in which measured complex field distributions on two slightly different planes are differentiated. In this measurement, we choose the distance between the two planes as 1.5 mm.

5.4 Demonstration of a Carpet Cloak

Fig. 5.11 shows the measured complex electric near-field distributions for the cases with (a) the carpet cloak, (b) a flat floor, and (c) a bump without the carpet cloak. Here, the frequency is chosen as 2.20 GHz ($\lambda_g = 12.7\Delta d$). By comparing Fig. 5.11(a) with (b), it is seen that the wave front of the reflected wave by the carpet cloak is flattened outside the carpet cloak area and the total field distribution reflects well the scattered field by the flat floor. On the other hand, from Fig. 5.11(c), it is seen that the incident wave is scattered by the bump to the left and right and its wave front is bent according to the bump shape.

For comparison, circuit simulations for the same configurations as the experiments are carried out with the distributed anisotropic metamaterials in Fig. 4.2 base on the same manner in Section 4.5. Figs. 5.12(a)–(c) show calculated complex voltage distributions for the cases with (a) the carpet cloak, (b) a flat floor, and (c) a bump without the carpet cloak, respectively. By comparing calculated results in Fig. 5.12 with measured results in Fig. 5.11, it is seen that measured results reflect well calculated results by circuit simulations.

Fig. 5.13 shows the measured complex electric near-field distributions at a higher frequency 4.55GHz ($\lambda_g = 6.2\Delta d$) for the cases with (a) the carpet cloak, (b) a flat floor,

and (c) a bump without the carpet cloak. By comparing Fig. 5.13(c) with Fig. 5.11(c), it is seen that although the level of scattered waves by the bump is increased, the carpet cloak can sufficiently suppress those scattered waves by the bump and mimic the flat floor (compare Fig. 5.13(a) with Fig. 5.13(b)).

Similarly, for comparison, circuit simulations for the same configurations as the experiments are also carried out. Figs. 5.14(a)–(c) show calculated complex voltage distributions for the cases with (a) the carpet cloak, (b) a flat floor, and (c) a bump without the carpet cloak, respectively. By comparing calculated results in Fig. 5.14 with measured results in Fig. 5.13, it is also seen that measured results can reflect well calculated results by circuit simulations.

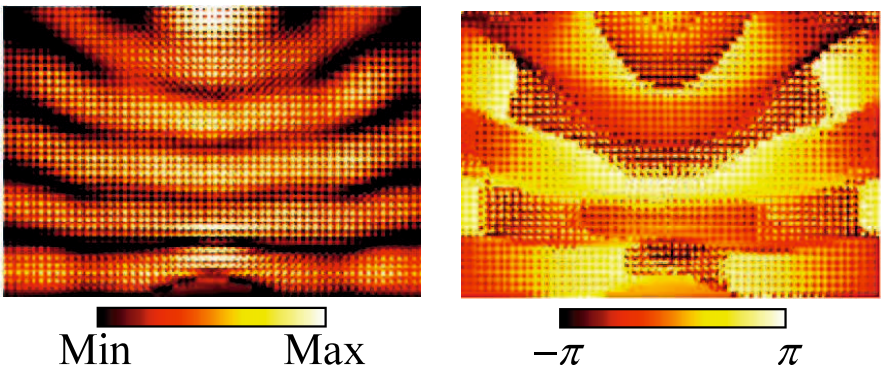

(a)

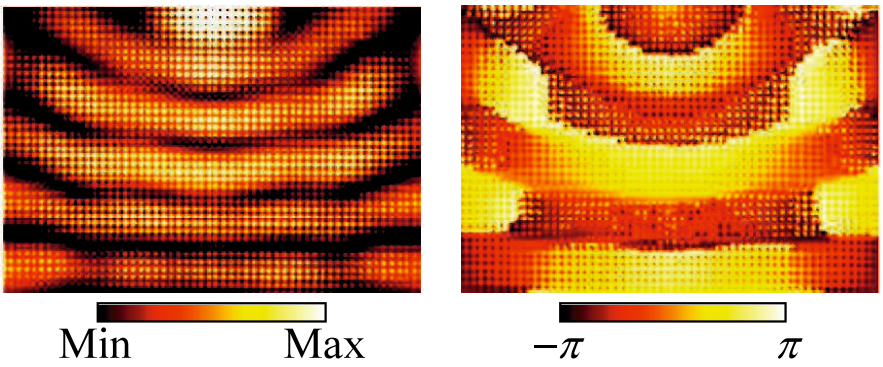

(b)

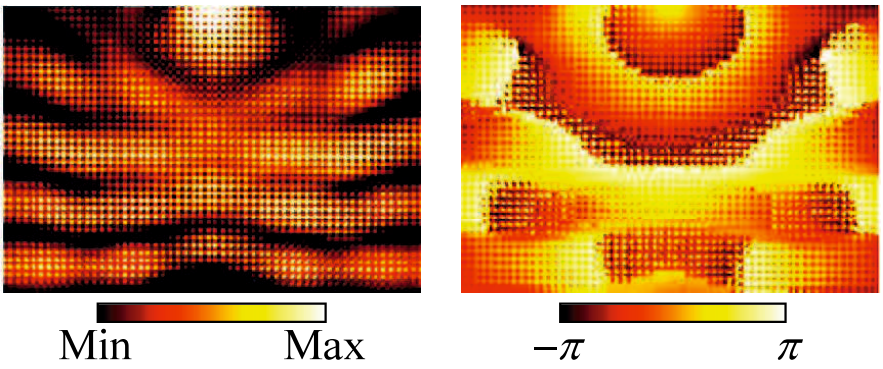

(c)

Fig. 5.11 Measured complex electric near-field distributions (λ_g = 12.7Δd at 2.20GHz). Left and right figures are amplitude and phase, respectively. (a) Carpet cloak. (b) Flat floor. (c) Bump without the carpet cloak.

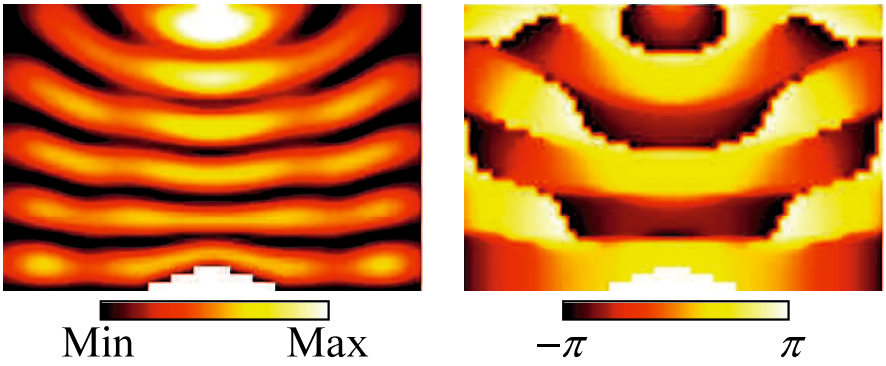

(a)

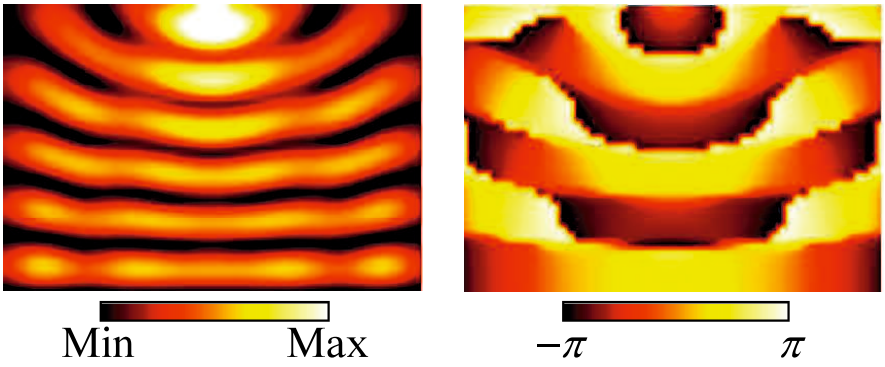

(b)

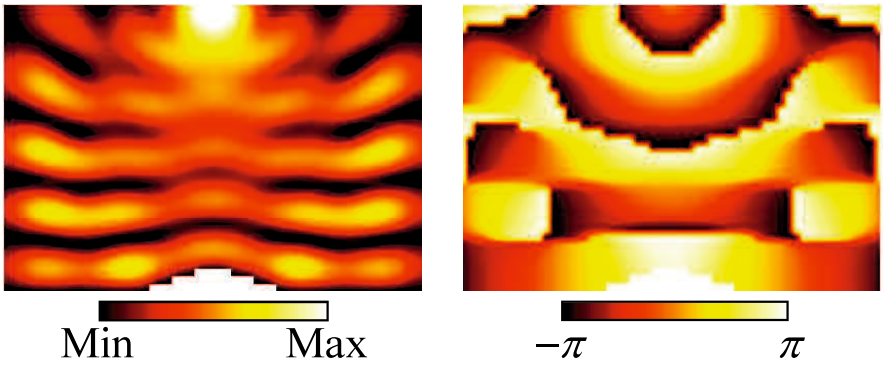

(c)

Fig. 5.12 Calculated complex voltage distributions (λ_g = 12.7Δd at 2.20GHz). Left and right figures are amplitude and phase, respectively. (a) Carpet cloak. (b) Flat floor. (c) Bump without the carpet cloak.

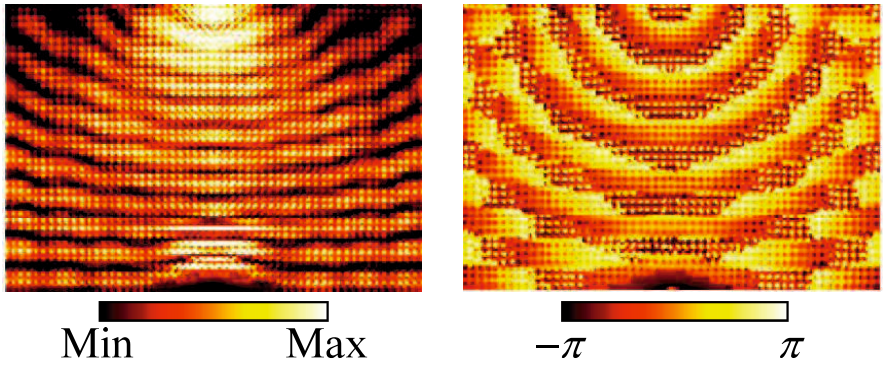

(a)

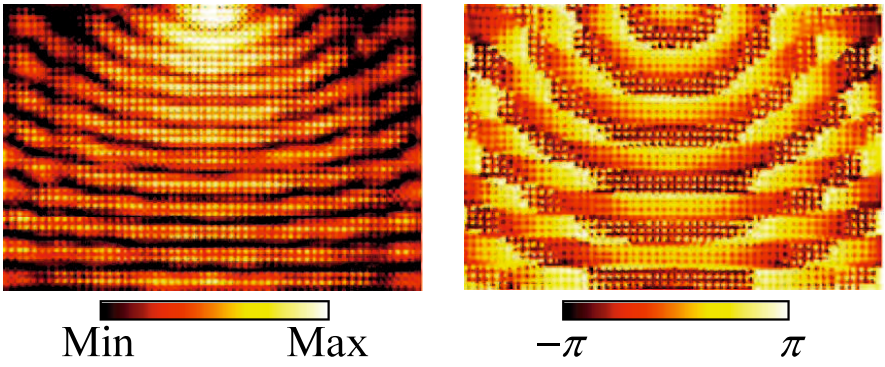

(b)

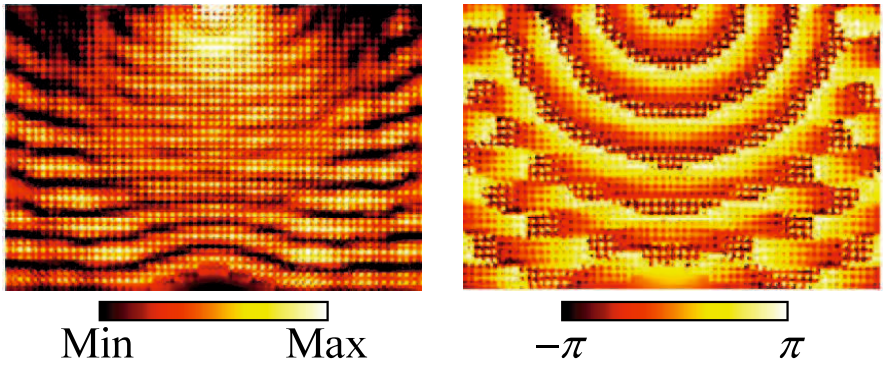

(c)

Fig. 5.13 Measured complex electric near-field distributions (λ_g = 6.2Δd at 4.55GHz). Left and right figures are amplitude and phase, respectively. (a) Carpet cloak. (b) Flat floor. (c) Bump without the carpet cloak.

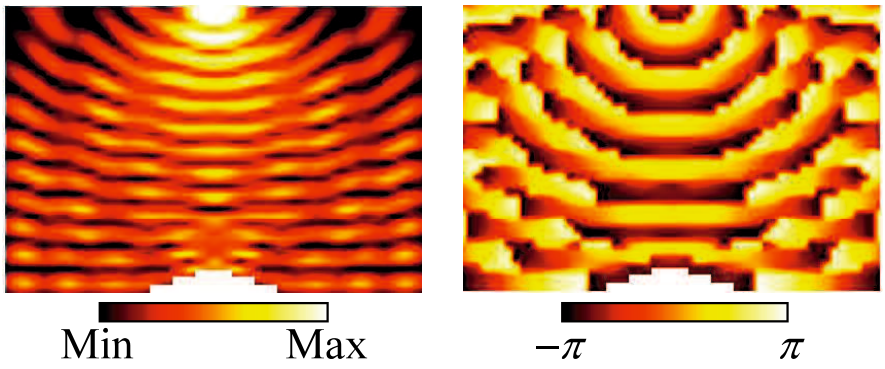

(a)

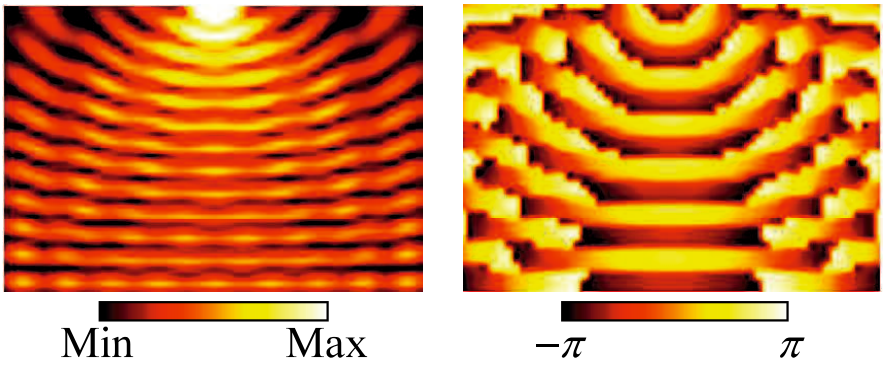

(b)

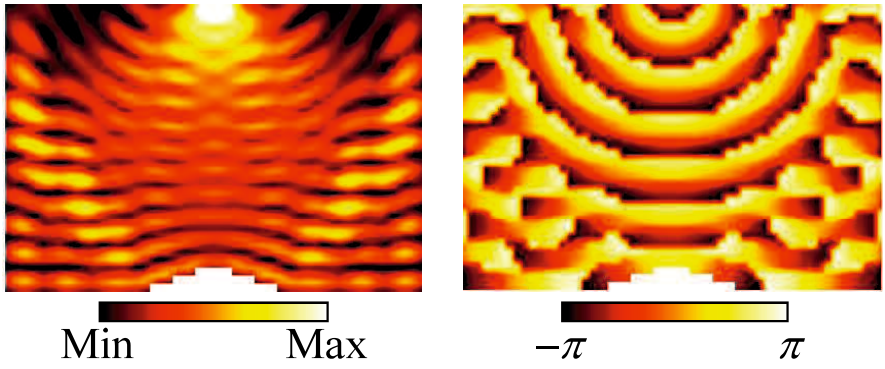

(c)

Fig. 5.14 Calculated complex voltage distributions ($\lambda_g = 6.2\Delta d$ at 4.55GHz). Left and right figures are amplitude and phase, respectively. (a) Carpet cloak. (b) Flat floor. (c) Bump without the carpet cloak.

In order to further confirm the operation of the carpet cloak, similar electric near-field measurements for the oblique incident case are also carried out. The measurement system is exactly the same as Fig. 5.10, and a coaxial cable is soldered at the top node on the left side column of the prototype as shown in Fig. 5.15.

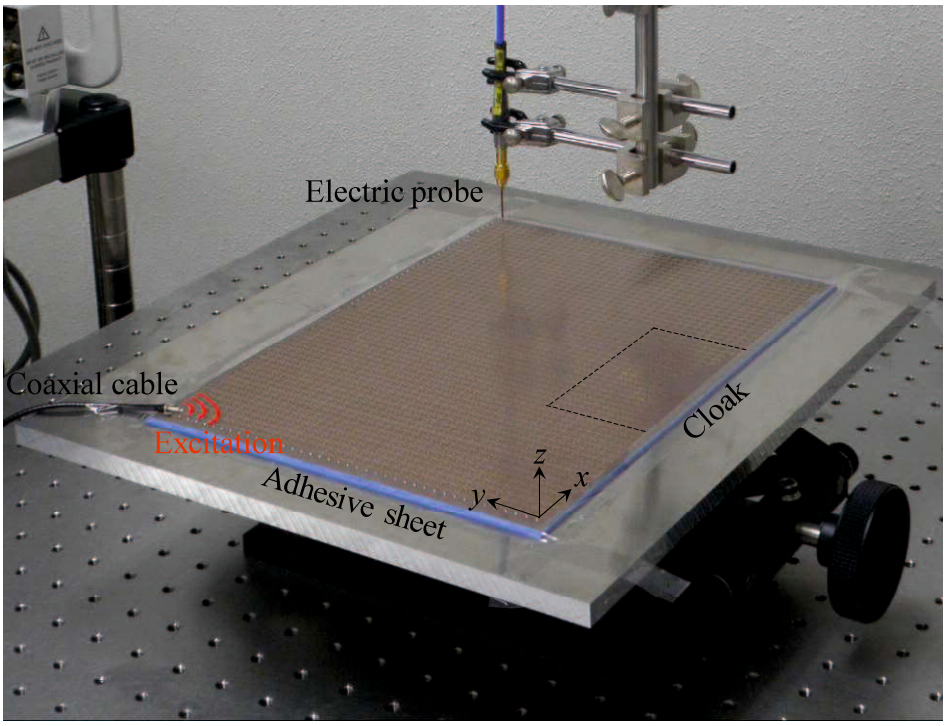

Fig. 5.15 Electric near-field measurement system for the oblique incident case.

Figs. 5.16(a)-(c) show measured complex electric near-field distributions for the cases with (a) the carpet cloak, (b) a flat floor, and (c) a bump without the carpet cloak, respectively. Here, the frequency is chosen as 4.65 GHz ($\lambda_g = 6.0\Delta d$). By comparing Fig. 5.16(a) with Fig. 5.16(b), it is seen that the total distribution of the carpet cloak reflects well the scattered field by the flat floor. Especially, from the phase distributions, it is also seen that the wave front of the reflected waves by the flat floor are recovered well by the carpet cloak. On the other hand, in Fig. 5.16(c), it is clearly seen that incident wave is strongly scattered by the bump in the almost normal direction. By comparing Fig. 5.16(a) with Fig. 5.16(c), the scattered waves by the bump can be suppressed well

by the carpet cloak.

Similarly, for comparison, circuit simulations for the same configurations as the experiments are also carried out. Figs. 5.17(a)–(c) show calculated complex voltage distributions for the cases with (a) the carpet cloak, (b) a flat floor, and (c) a bump without the carpet cloak, respectively. By comparing calculated results in Fig. 5.17 with measured results in Fig. 5.16, it is seen that measured results reflect well the calculated results by circuit simulations. Therefore, the validity of the measured results for the oblique incident case is confirmed.

From these results, it can be concluded that the validity of the design theory with the proposed distributed anisotropic metamaterials is confirmed and operations of the implemented carpet cloak are successfully demonstrated.

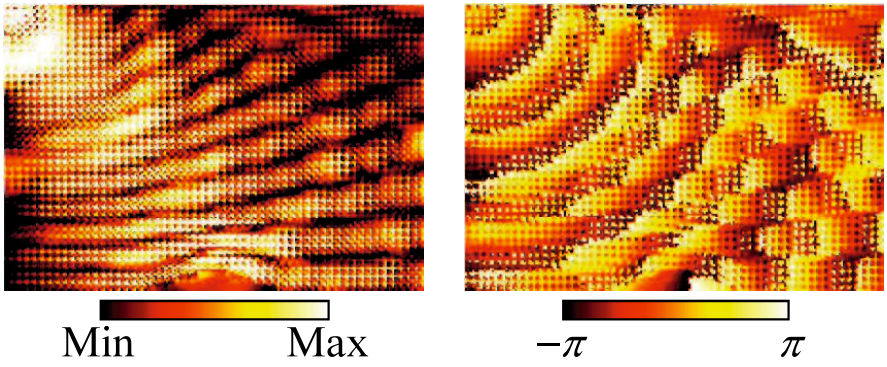

(a)

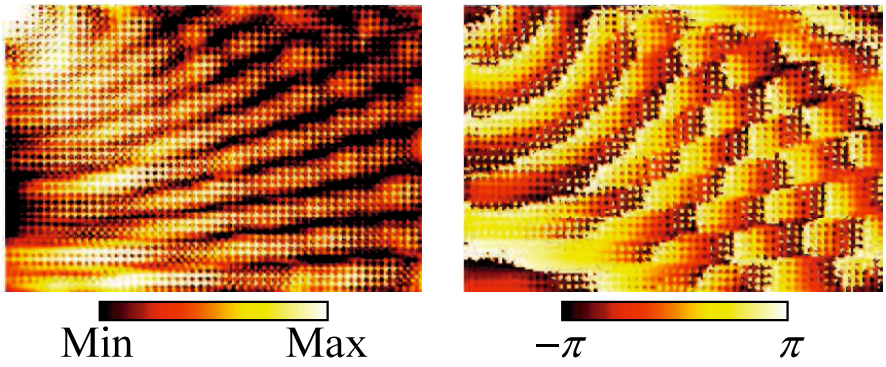

(b)

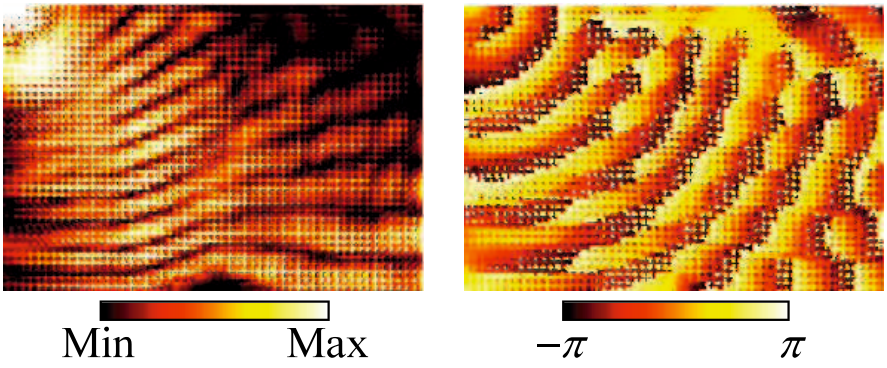

(c)

Fig. 5.16 Measured complex electric near-field distributions for the oblique incident case (λ_g = 6.0Δd at 4.65GHz). Left and right figures are amplitude and phase, respectively. (a) Carpet cloak. (b) Flat floor. (c) Bump without the carpet cloak.

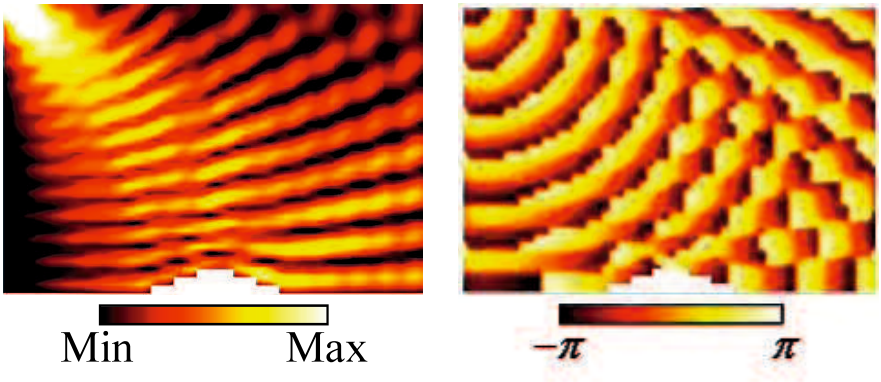

(a)

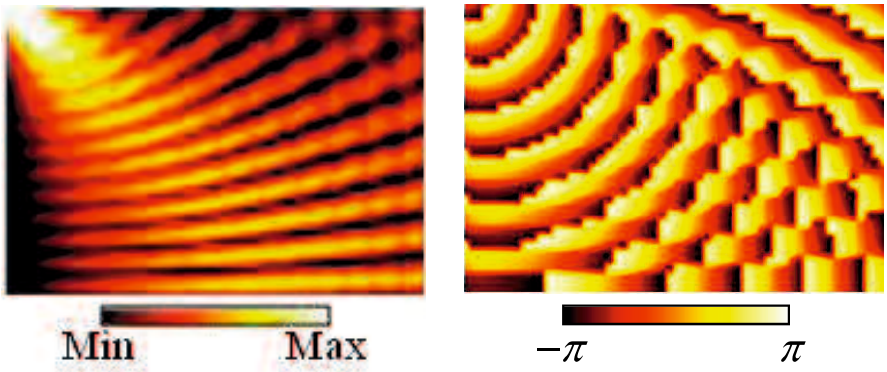

(b)

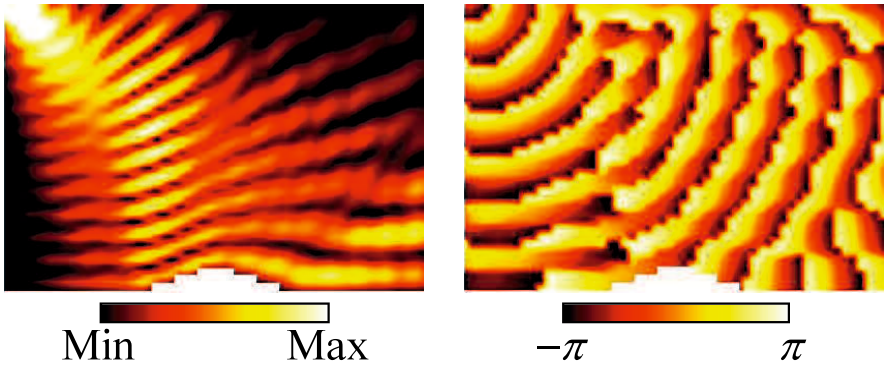

(c)

Fig. 5.17 Calculated complex voltage distributions for the oblique incident case (λ_g = 6.0Δd at 4.65GHz). Left and right figures are amplitude and phase, respectively. (a) Carpet cloak. (b) Flat floor. (c) Bump without the carpet cloak.

Chapter 6 Applications to Illusion Media

In this chapter, in order to show further potentials of the proposed distributed anisotropic metamaterials, an illusion medium [56]–[63] mimicking scattered waves by a groove is designed with the distributed anisotropic metamaterials. First, the concept of illusion media is presented. Secondly, the illusion medium mimicking a groove is designed with the proposed distributed anisotropic metamaterials. Finally, its operations are confirmed by circuit simulations.

6.1 Concept of Illusion Media

Illusion media are media to mimic scatted waves by arbitral objects [56]–[63]. The illusion media can also be realized by using the medium which is designed based on material interpretation of the coordinate transformation. Here, the concept of illusion media is introduced in detail with an example.

Let us consider the Cartesian coordinate system (x, y) with a groove on the bottom as shown in Fig. 6.1(a) and transform the coordinate system into the square non-conformal coordinate system (x', y') as shown in Fig. 6.1(b) by using the following relations:

$$x' = x \tag{6.1}$$

$$y' = \frac{y + A\left\{1 - \left(\frac{x}{p}\right)^2\right\}^2}{h + A\left\{1 - \left(\frac{x}{p}\right)^2\right\}^2} h, \tag{6.2}$$

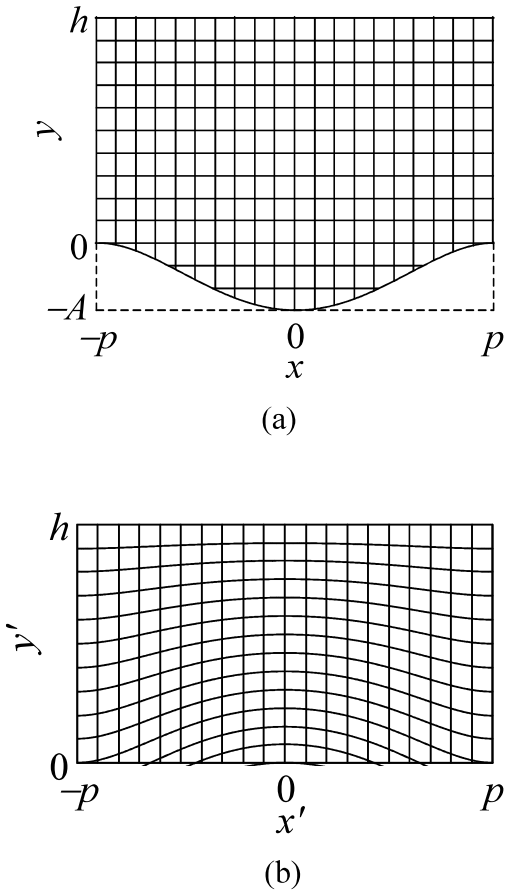

Fig. 6.1 Coordinate transformation for the illusion medium design. (a) Original coordinate system including a groove on the bottom (x, y). (b) Transformed square non-conformal coordinate system (x', y').

where $-p \le x \le p$, $A\{1-(x/p)^2\}^2 \le y \le h$, $-p \le x' \le p$, and $0 \le y' \le h$. By designing the medium corresponding to the transformed coordinate system of Fig. 6.1(b) based on material interpretation, we can mimic a groove in the original coordinate system of Fig. 6.1(a). For example, if the medium is put on a flat floor as shown in Fig. 6.2(a), the medium has exactly the same scattered waves as those by the groove as shown in Fig. 6.2(b). We chose the parameters as $p = h = 10\Delta d$ and $A = 0.3h = 3\Delta d$ in the following design.

(a)

(b)

Fig. 6.2 The concept of an illusion medium. (a) An illusion medium mimicking scattered waves from a groove. (b) Scattering by a groove to be mimicked.

6.2 Illusion Medium Design with Distributed Anisotropic Metamaterials

As the first step of the illusion medium design with the distributed anisotropic metamaterials, we calculate equivalent circuit parameters L_x, L_y, M, and C in Fig. 3.4 according to (3.19)–(3.22). Figs. 6.3(a)–(d) show obtained L'_x/μ_0, L'_y/μ_0, M'/μ_0, and C'/ε_0, respectively. Here, for the half areas of $x < 0$ and $x > 0$, the unit cells of Figs 3.4(a) and (b) are used due to $\mu_{xy} = \mu_{yx} > 0$ and $\mu_{xy} = \mu_{yx} < 0$ according to (2.3), respectively. From Figs. 6.3(a) and (b), it is seen that L'_x/μ_0 and L'_y/μ_0 take minimum

and maximum at the center of the area (x, y) = (0, y), respectively. Besides, from Fig. 6.3(c), it is seen that M'/μ_0 takes 0 value at the center, top, and both sides of the area (0, y), (x, h), and ($\pm p$, y), respectively, and the off-diagonal permeability tensor components μ_{xy} and μ_{yx} become non-zero at the other area. It is seen from Fig. 6.3(d) that C'/ε_0 takes maximum at the center of the area.

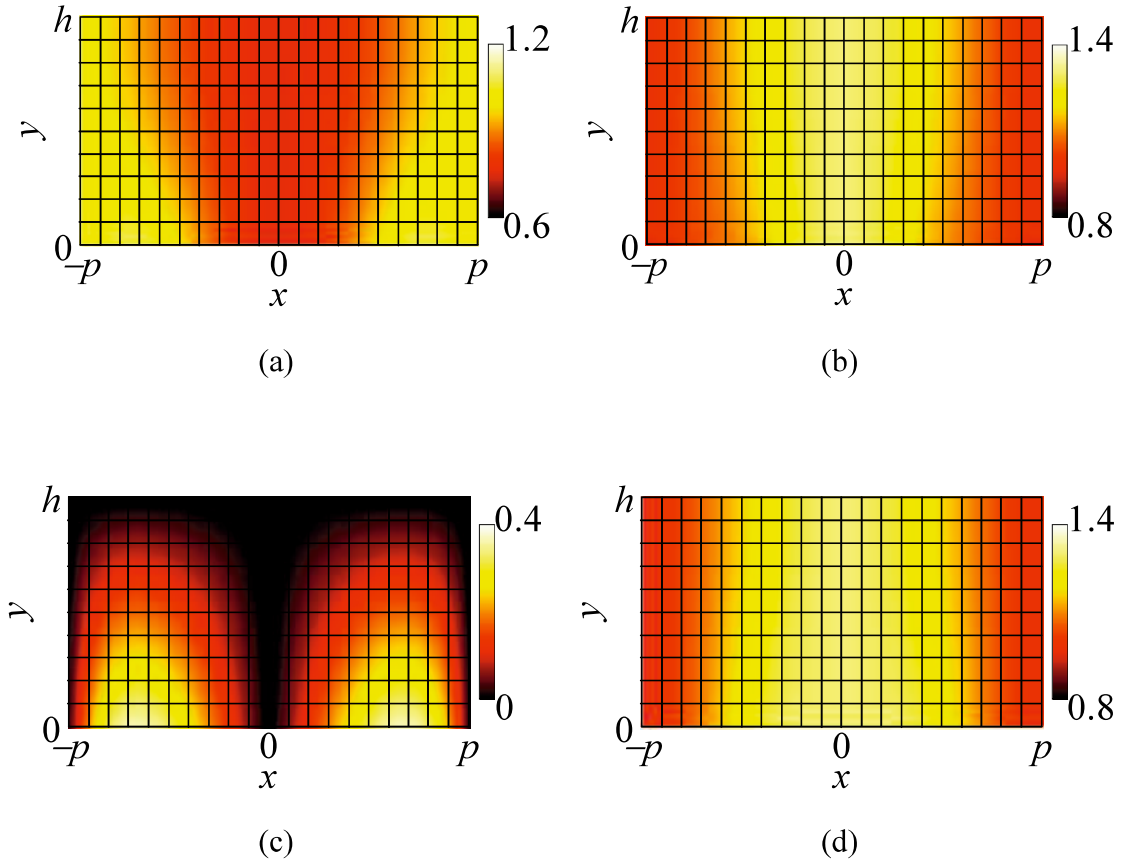

Fig. 6.3 Equivalent circuit parameters in Fig. 3.4 for the illusion medium design. The unit cells of Figs. 3.4(a) and (b) are used for the half area of $x < 0$ and $x > 0$, respectively. (a) Normalized self-inductance per-unit-length L'_x/μ_0. (b) Normalized self-inductance per-unit-length L'_y/μ_0. (c) Normalized mutual inductance per-unit-length M'/μ_0. (d) Normalized capacitance per-unit-length C'/ε_0.

Then, we determine transmission-line parameters Z_{0x}, Z_{0y}, βl, and $\beta_M l_M$ in Fig. 4.2 from calculated L_x, L_y, M, and C in Fig. 6.3 by solving (4.8)–(4.11) simultaneously with the parameter $Z_{0M}/\eta = 1.5$ which is chosen as a degree of freedom. Figs. 6.4(a)–(d) show obtained Z_{0x}/η, Z_{0y}/η, $\beta l/k\Delta d$, and $\beta_M l_M/k\Delta d$, respectively. Here, for the half area of $x < 0$ and $x > 0$, the unit cells of Figs 4.2(a) and (b) are used since $\mu_{xy} = \mu_{yx} > 0$ and $\mu_{xy} = \mu_{yx} < 0$ according to (2.3), respectively. From Figs. 6.4(a) and (b), it is seen that Z_{0x}/η and Z_{0y}/η take minimum and maximum at the center of the area $(x, y) = (0, y)$, respectively. Besides, from Fig. 6.4(c), it is seen that $\beta l/k\Delta d$ takes maximum at the center of the area $(0, y)$. In addition, from Fig. 6.4(d), it is seen that $\beta_M l_M/k\Delta d$ takes 0 value at the center, top, and both sides of the area $(0, y)$, (x, h), and $(\pm p, y)$, respectively.

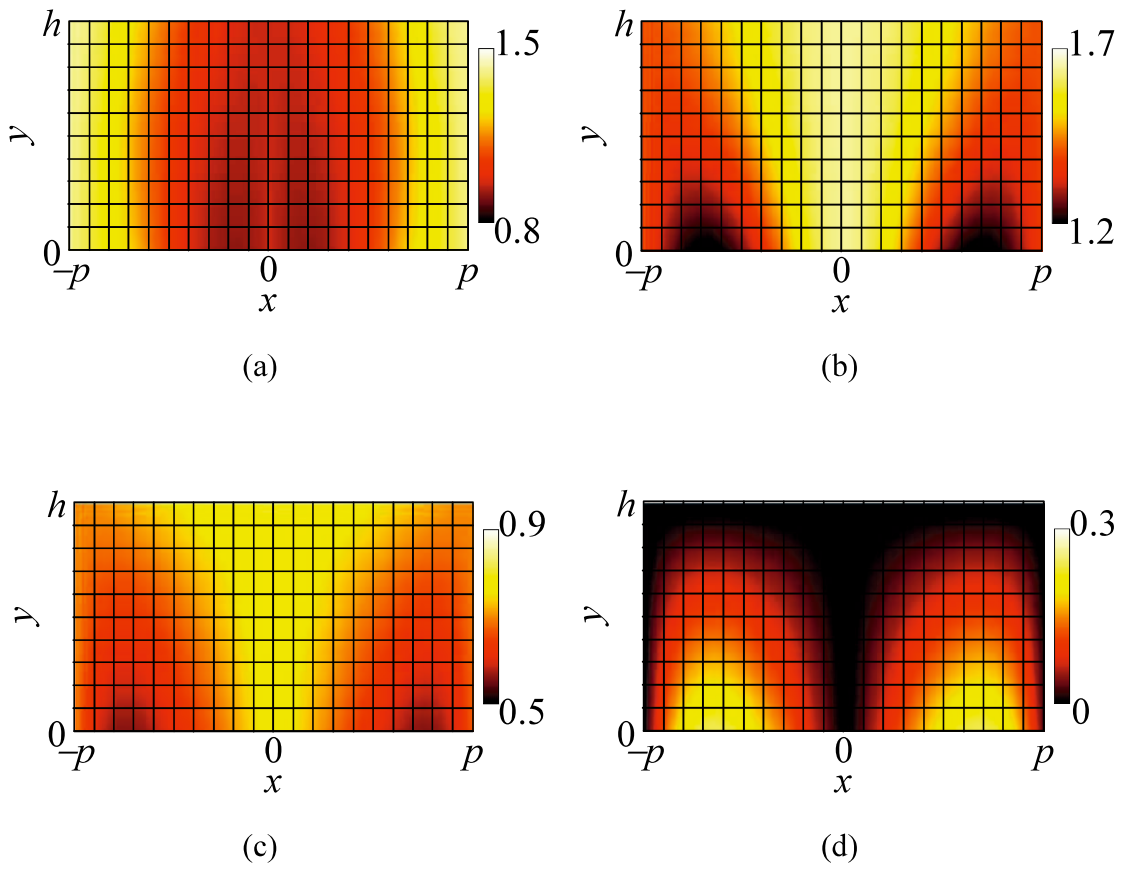

Fig. 6.4 Transmission-line parameters of the distributed anisotropic metamaterials in Fig. 4.2 for the illusion medium design. The unit cells of Figs. 4.2(a) and (b) are used for the half area of $x < 0$ and $x > 0$, respectively. (a) Normalized characteristic impedance Z_{0x}/η. (b) Normalized characteristic impedance Z_{0y}/η. (c) Normalized electrical length $\beta l/k\Delta d$. (d) Normalized electrical length $\beta_M l_M/k\Delta d$. Here, $Z_{0M}/\eta = 1.5$ is chosen as a degree of freedom.

6.3 Circuit Simulations

In order to validate the illusion medium design, circuit simulations are carried out with a SPICE simulator.

For the illusion medium simulations, we first prepare the same node list of 20 × 10 cells shown in Fig. 3.9. For the left half area of Fig. 3.9, the unit cell of Fig. 4.2(a) is used, and for the right half area, the unit cell of Fig. 4.2(b) is used. The transmission-line is dealt as an ideal transmission-line. The transmission-line parameters for each unit cell are given from the values in Figs. 6.4(a)–(d). In addition, we put the illusion medium at the bottom center of the isotropic area in Fig. 3.8(b) with the unit cell of Fig. 4.4. The refractive index and the wave impedance of isotropic area are chosen to be $n = k/k_0 = 2.14$ and $\eta = 63.6$, which are the same values as those in carpet cloak simulations of Section 4.5. On the other hand, for the case with the groove simulations, a node list with the unit cell of Fig. 4.4 is placed by those of Fig. 6.5 with the isotropic unit cell in Fig. 3.8(b).

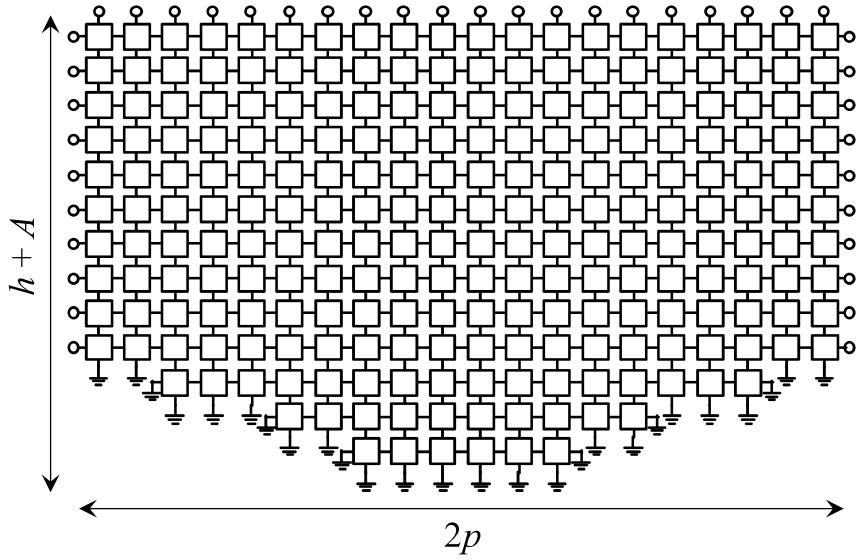

Fig. 6.5 Node list for the groove simulations. Here, the unit cell of Fig. 4.4 is used.

As in the circuit simulation in Section 4.5, fifty in-phase voltage sources (n_s = 50) with the internal impedance of 62Ω are connected at the top row. The amplitudes of the voltage sources are set to form the Gaussian beam with the beam waist of $10\Delta d$. Similarly, nodes on the bottom boundary including the groove area are short-circuited, and the other nodes are terminated by resistors with 62Ω. Then, the complex voltage distributions of the center nodes in all unit cells are calculated.

Figs. 6.6(a)–(c) show calculated complex voltage distributions for the cases with (a) the illusion medium, (b) a groove, and (c) a flat floor without the illusion medium, respectively. Here, the wavelength is chosen as $\lambda_g = 12\Delta d$. By comparing Figs. 6.6(a) with (b), it is seen that those calculated distributions agree well each other and the illusion medium can mimic the groove well. On the other hand, by comparing Figs. 6.6(a) with (c), it is also seen that scattered waves by the illusion medium are clearly different to those by the flat floor.

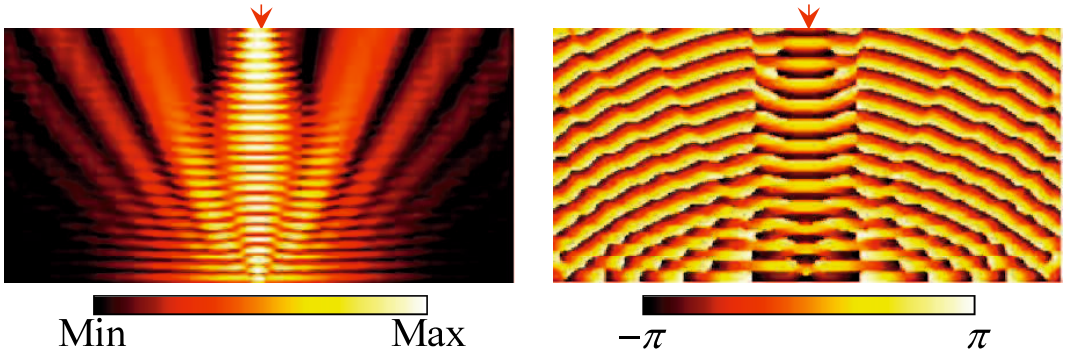

(a)

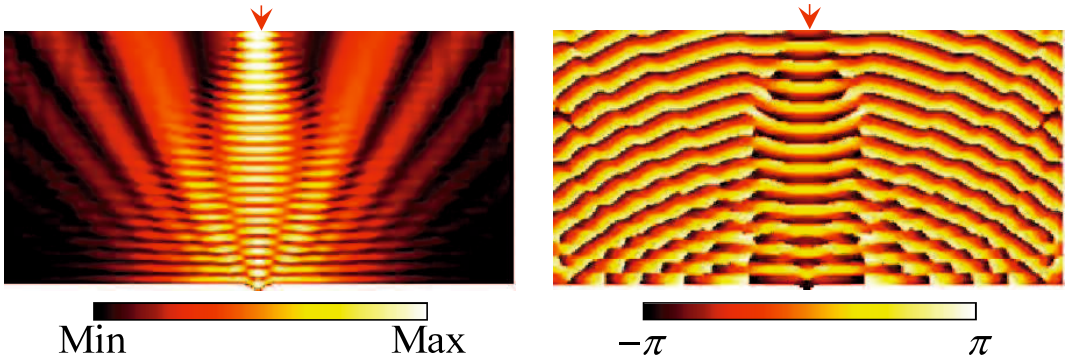

(b)

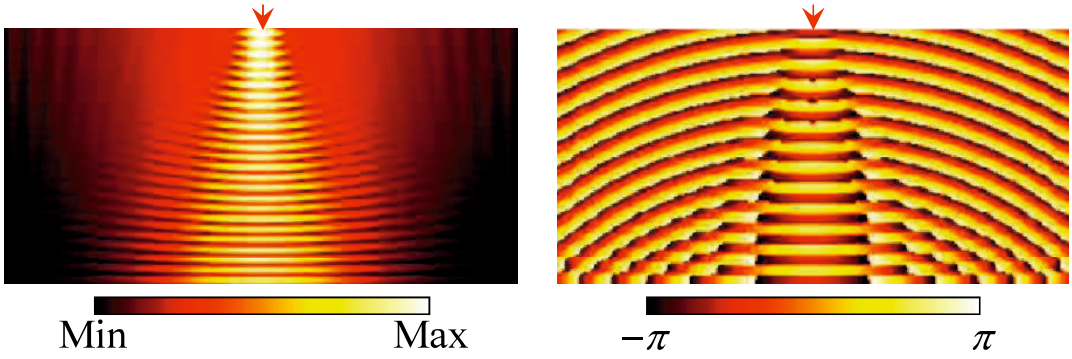

(c)

Fig. 6.6 Calculated complex voltage distributions ($\lambda_g = 12\Delta d$). Left and right figures are amplitude and phase, respectively. (a) Illusion medium. (b) Groove. (c) Flat floor without the illusion medium.

In order to further confirm the operation of the illusion medium, circuit simulations for the oblique incident cases (θ_{inc} = 30, 45, and 60 deg) are carried out. Here, setting of all the simulations is the same as those in Section 4.5. Figs. 6.7–6.9 show the calculated complex voltage distributions for the cases with θ_{inc} = 30, 45, and 60 deg, respectively. In these figures, the calculated results for the cases with (a) the illusion medium, (b) a groove, and (c) a flat floor without the illusion medium are also shown. The wavelength is chosen as $\lambda_g = 12\Delta d$. From these figures, it is seen that the illusion medium cam mimic the groove well even with the oblique incident cases.

From these results, it can be concluded that operations of the designed illusion medium are confirmed, and it is shown that the proposed distributed anisotropic metamaterials can be used for implementing media based on transformation electromagnetics other than cloaks of invisibility.

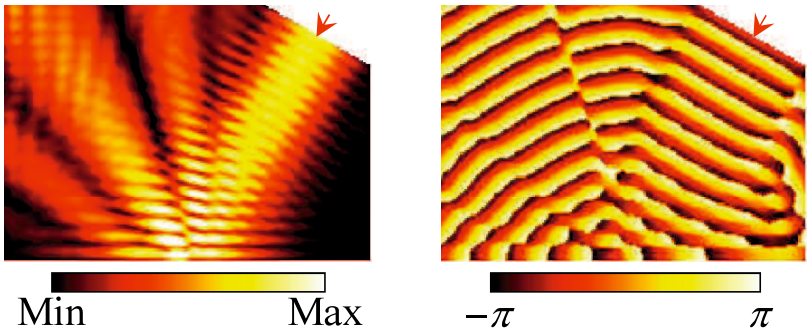

(a)

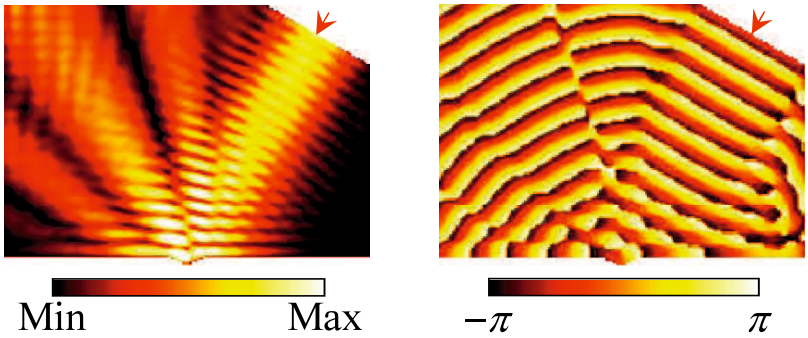

(b)

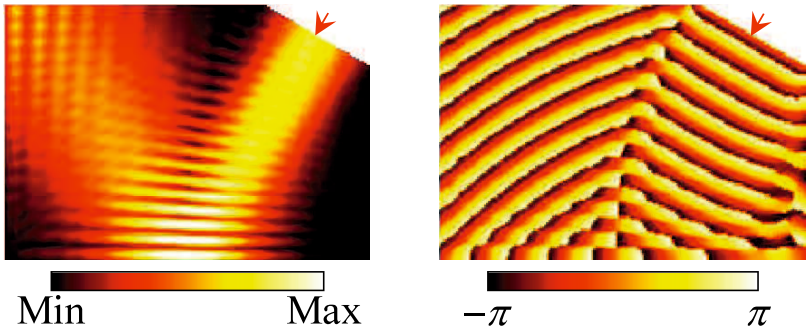

(c)

Fig. 6.7 Calculated complex voltage distributions for the case with θ_{inc} = 30 deg (λ_g = 12Δd). Left and right figures are amplitude and phase, respectively. (a) Illusion medium. (b) Groove. (c) Flat floor without the illusion medium.

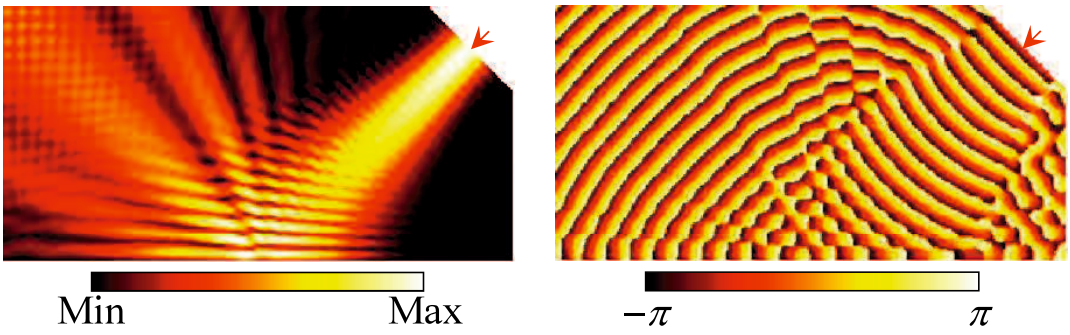

(a)

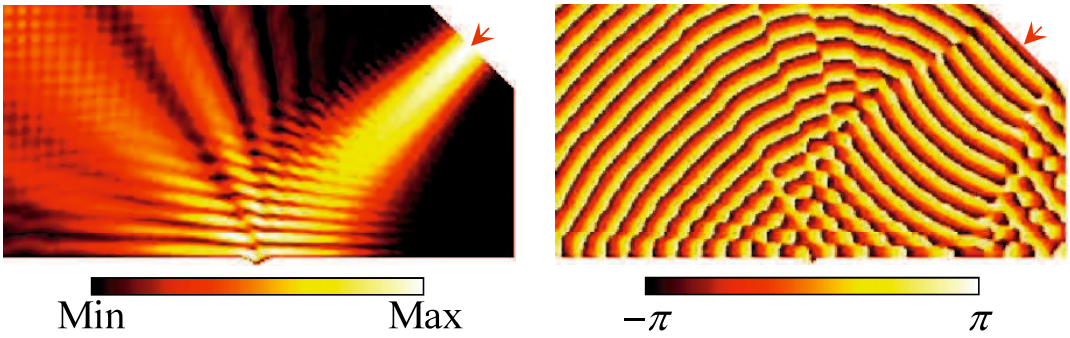

(b)

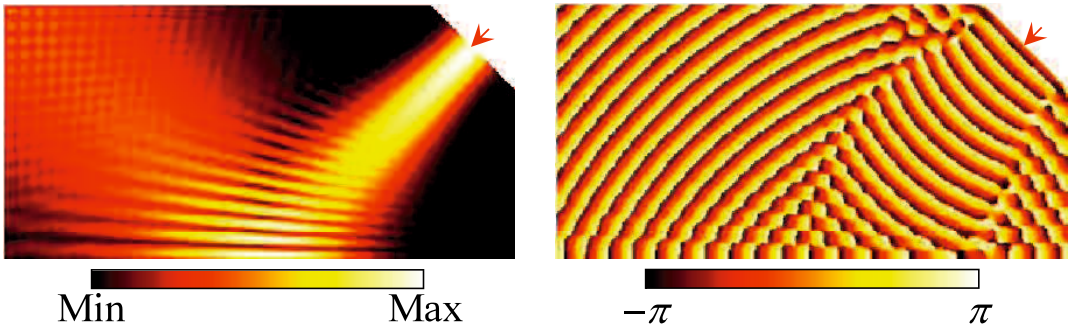

(c)

Fig. 6.8 Calculated complex voltage distributions for the case with θ_{inc} = 45 deg (λ_g = 12Δd). Left and right figures are amplitude and phase, respectively. (a) Illusion medium. (b) Groove. (c) Flat floor without the illusion medium.

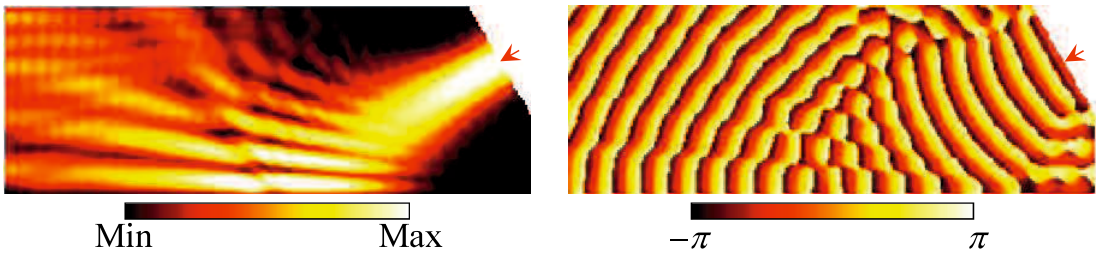

(a)

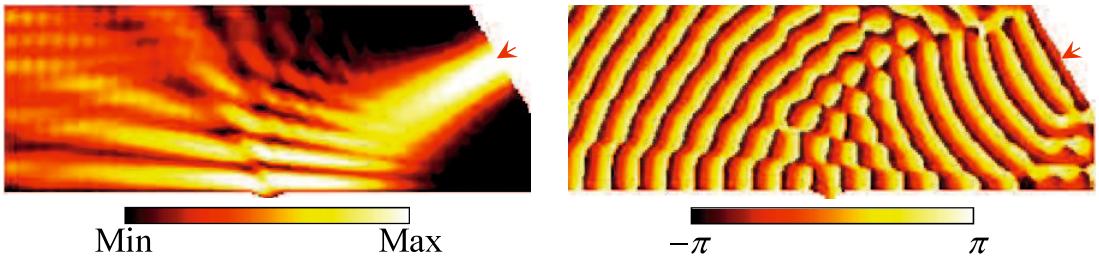

(b)

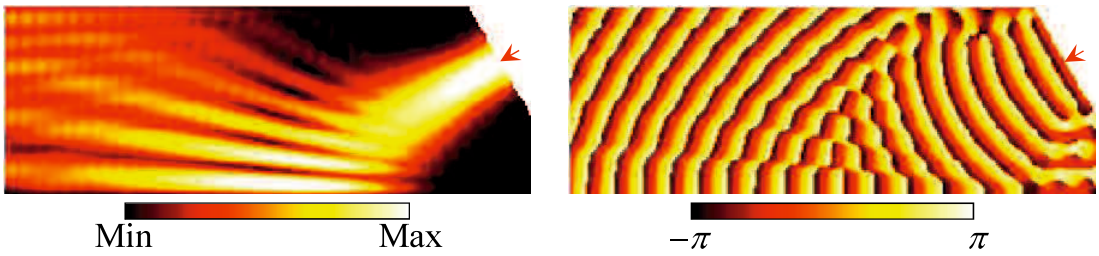

(c)

Fig. 6.9 Calculated complex voltage distributions for the case with θ_{inc} = 60 deg (λ_g = 12Δd). Left and right figures are amplitude and phase, respectively. (a) Illusion medium. (b) Groove. (c) Flat floor without the illusion medium.

Chapter 7 Conclusions

In this thesis, distributed anisotropic metamaterials for transformation electromagnetics has been studied. First, the theoretical model for transformation electromagnetics based on the transmission-line approach has been proposed, and major subjects for transformation electromagnetics: full control of anisotropy including the off-diagonal tensor components, and wideband and low-loss properties have been achieved by the proposed circuit model. Secondly, a novel distributed anisotropic metamaterial for implementing the proposed theoretical mode has been proposed, and the theory for composing media based on transformation electromagnetics has been established. Finally, based on the theory for composing media, the proposed distributed anisotropic metamaterials have been implemented, and the validity of the theory has been confirmed by demonstrating a carpet cloak of invisibility experimentally.

In Chapter 2, the theory and concept of transformation electromagnetics have been overviewed. Mathematical treatment and potentials of transformation electromagnetics have been shown, and design formulas for a cylindrical cloak of invisibility have also been shown as an example.

In Chapter 3, the equivalent circuit model for full-tensor anisotropic materials based on the transmission-line approach has been proposed. The circuit model can realize the wideband and low-loss properties due to its intrinsic non-resonant property. Besides, from the duality between circuit equations and Maxwell's equations, it has been shown that the diagonal permeability tensor components μ_{xx} and μ_{yy} correspond to the self-inductances per-unit-length L'_y and L'_x in the circuit model, respectively, and more importantly, the off-diagonal permeability tensor components μ_{xy} and μ_{yx} correspond to

the mutual inductance per-unit-length M' in the circuit model. It has also been shown that the circuit model corresponds to the homogeneous dispersionless medium with μ_{xx}, μ_{xy}, μ_{yx}, μ_{yy}, and ε_z under the condition of the infinitesimal limit $\Delta d \to 0$ (or $\lambda_g >> \Delta d$), and therefore the model has intrinsically wideband properties from DC to a certain frequency at which the discretization errors cannot be neglected. In addition, a carpet cloak of invisibility has been designed with the proposed circuit model and its cloaking operation and has been confirmed by circuit simulations. Therefore, the validity of the theory of the proposed equivalent circuit model has been confirmed.

In Chapter 4, distributed anisotropic metamaterials for implementing the proposed circuit model have been proposed. First, equivalence of the metamaterial to the proposed circuit model has been shown theoretically and the design formulas for structural parameters of metamaterial constituents have been derived. It has also been shown that the proposed distributed anisotropic metamaterials essentially operate as the proposed lumped element circuit model at lower frequencies down to DC. In addition, the carpet cloak of invisibility has been designed with the proposed distributed anisotropic metamaterials, and the validity of the theory of the proposed distributed anisotropic metamaterials as well as their wideband operations have been confirmed by circuit simulations.

In Chapter 5, a carpet cloak of invisibility designed in the previous chapter with the proposed distributed anisotropic metamaterials has been implemented on a dielectric substrate with microstrip-line technology. It has been experimentally shown by electric near-field measurements that the carpet cloak suppresses scattered waves by a bump and mimics the flat floor, and therefore the validity of the theory of the proposed distributed anisotropic metamaterials has been demonstrated experimentally.

In Chapter 6, in order to show further potentials of the proposed distributed anisotropic metamaterials, an illusion medium mimicking scattered waves by a groove has been designed with the proposed distributed anisotropic metamaterials. Operations of the designed illusion medium have been confirmed by circuit simulations. It has been successfully shown that this approach can also be applied to other media based on transformation electromagnetics than cloaks of invisibility.

The proposed distributed anisotropic metamaterials can be useful for implementing novel planar circuit devices. For instance, a 2-D resonator based on transformation electromagnetics could have unique property in which the resonant frequencies become exactly the same as those of the original resonator including higher harmonics regardless of its physical shape. In addition, Rotman lenses based on 2-D transformation is another possible candidate for microwave application.

The proposed distributed anisotropic metamaterials have been implemented with planar circuits in this thesis, however, implementations are not limited to planar circuits and other implementation methods are future subjects to be tackled. 3-D extensions of the structures are also another future subject. In addition, implementations of the media without metal will be required to reduce conductor losses, which is to be realized at higher frequency above terahertz and optical wave regions. Furthermore, exporting the concept of transformation electromagnetics to other academic fields (elastic waves, heat, fluids, and the like) is also challenging but interesting topic in the future.

Appendix

In this appendix, details of formulas for the *Z*-parameters of Fig. 4.2(a) and Fig. 3.4(a) in Section 4.2 are given as follows.

First, the *Z*-parameter components of (4.1) for the transmission-line network in Fig. 4.2(a) are given as:

$$\begin{aligned} Z_{11} &= Z_{22} \\ &= jZ_{0x}\tan\left(\frac{\beta_x l_x}{2}\right) \\ &\quad + \frac{1}{D}\left[j\frac{Z_{0\mathrm{M}}}{Z_{0x}}\left\{\tan\left(\frac{\beta_x l_x}{2}\right)+\tan^3\left(\frac{\beta_x l_x}{2}\right)\right\}\right. \\ &\quad + j\frac{Z_{0\mathrm{M}}^2}{Z_{0y}}\left\{\sec^2\left(\frac{\beta_x l_x}{2}\right)\tan\left(\frac{\beta_y l_y}{2}\right)\right\} \\ &\quad \left. - jZ_{0\mathrm{M}}^2\sec^2\left(\frac{\beta_x l_x}{2}\right)\cot\left(\beta_{\mathrm{M}} l_{\mathrm{M}}\right)\right] \end{aligned} \tag{A1}$$

$$\begin{aligned} Z_{33} &= Z_{44} \\ &= jZ_{0y}\tan\left(\frac{\beta_y l_y}{2}\right) \\ &\quad + \frac{1}{D}\left[j\frac{Z_{0\mathrm{M}}^2}{Z_{0x}}\left\{\tan\left(\frac{\beta_x l_x}{2}\right)\sec^2\left(\frac{\beta_y l_y}{2}\right)\right\}\right. \\ &\quad + j\frac{Z_{0\mathrm{M}}}{Z_{0y}}\left\{\tan\left(\frac{\beta_y l_y}{2}\right)+\tan^3\left(\frac{\beta_y l_y}{2}\right)\right\} \\ &\quad \left. - jZ_{0\mathrm{M}}^2\sec^2\left(\frac{\beta_y l_y}{2}\right)\cot\left(\beta_{\mathrm{M}} l_{\mathrm{M}}\right)\right] \end{aligned} \tag{A2}$$

$$
\begin{aligned}
Z_{14} &= Z_{23} = Z_{32} = Z_{41} \\
&= j\frac{1}{D}\left[j\frac{Z_{0\mathrm{M}}^2}{Z_{0x}}\tan\left(\frac{\beta_x l_x}{2}\right)\sec\left(\frac{\beta_x l_x}{2}\right)\sec\left(\frac{\beta_y l_y}{2}\right)\right. \\
&\qquad + j\frac{Z_{0\mathrm{M}}^2}{Z_{0y}}\sec\left(\frac{\beta_x l_x}{2}\right)\tan\left(\frac{\beta_y l_y}{2}\right)\sec\left(\frac{\beta_y l_y}{2}\right) \\
&\qquad \left. - jZ_{0\mathrm{M}}^2\sec\left(\frac{\beta_x l_x}{2}\right)\sec\left(\frac{\beta_y l_y}{2}\right)\cot\left(\beta_{\mathrm{M}} l_{\mathrm{M}}\right)\right]
\end{aligned} \tag{A3}
$$

$$
Z_{12} = Z_{21} = \frac{1}{D}\left[- jZ_{0\mathrm{M}}\sec^2\left(\frac{\beta_x l_x}{2}\right)\mathrm{cosec}\left(\beta_{\mathrm{M}} l_{\mathrm{M}}\right)\right] \tag{A4}
$$

$$
Z_{34} = Z_{43} = \frac{1}{D}\left[- jZ_{0\mathrm{M}}\sec^2\left(\frac{\beta_y l_y}{2}\right)\mathrm{cosec}\left(\beta_{\mathrm{M}} l_{\mathrm{M}}\right)\right] \tag{A5}
$$

$$
\begin{aligned}
Z_{13} &= Z_{24} = Z_{31} = Z_{42} \\
&= \frac{1}{D}\left[- jZ_{0\mathrm{M}}\sec\left(\frac{\beta_x l_x}{2}\right)\sec\left(\frac{\beta_y l_y}{2}\right)\mathrm{cosec}\left(\beta_{\mathrm{M}} l_{\mathrm{M}}\right)\right],
\end{aligned} \tag{A6}
$$

where

$$
\begin{aligned}
D &= 2\cot\left(\beta_{\mathrm{M}} l_{\mathrm{M}}\right)\left\{\frac{Z_{0\mathrm{M}}}{Z_{0x}\cot\left(\frac{\beta_x l_x}{2}\right)} + \frac{Z_{0\mathrm{M}}}{Z_{0y}\cot\left(\frac{\beta_y l_y}{2}\right)}\right\} + 1 \\
&\quad - \mathrm{cosec}\left(\beta_{\mathrm{M}} l_{\mathrm{M}}\right)\frac{1}{D}\left[\frac{Z_{0\mathrm{M}}}{Z_{0x}\cot\left(\frac{\beta_x l_x}{2}\right)} + \frac{Z_{0\mathrm{M}}}{Z_{0y}\cot\left(\frac{\beta_y l_y}{2}\right)}\right]^2 .
\end{aligned} \tag{A7}
$$

Here, if the condition of (4.7) is given, equations (A4)–(A6) become identical as shown in the following:

$$
\begin{aligned}
Z_{12} &= Z_{21} = Z_{34} = Z_{43} = Z_{13} = Z_{24} = Z_{31} = Z_{42} \\
&= \frac{1}{D}\left[- jZ_{0\mathrm{M}}\sec^2\left(\frac{\beta l}{2}\right)\mathrm{cosec}\left(\beta_{\mathrm{M}} l_{\mathrm{M}}\right)\right] .
\end{aligned} \tag{A8}
$$

Incidentally, by interchanging the matrix elements of (Z_{14}, Z_{23}, Z_{32}, Z_{41}) and (Z_{13}, Z_{24}, Z_{31}, Z_{42}), Z-parameter components for the isomer transmission-line network in Fig. 4.2(b) can be obtained. On the other hand, the Z-parameter components of (4.1) for the equivalent circuit model in Fig. 3.4(a) are given as:

$$Z'_{11} = Z'_{22} = \frac{j\omega L_x}{2} + \frac{1}{j\omega C} \tag{A9}$$

$$Z'_{33} = Z'_{44} = \frac{j\omega L_y}{2} + \frac{1}{j\omega C} \tag{A10}$$

$$Z'_{14} = Z'_{23} = Z'_{32} = Z'_{41} = \frac{j\omega M}{2} + \frac{1}{j\omega C} \tag{A11}$$

$$Z'_{12} = Z'_{13} = Z'_{21} = Z'_{24} = Z'_{31} = Z'_{34} = Z'_{42} = Z'_{43} = \frac{1}{j\omega C}. \tag{A12}$$

Similarly, by interchanging the matrix elements of (Z'_{14}, Z'_{23}, Z'_{32}, Z'_{41}) and (Z'_{13}, Z'_{24}, Z'_{31}, Z'_{42}), Z-parameter components for the isomer transmission-line network in Fig. 3.4(b) can be obtained.

Acknowledgement

This work is carried out from 2010 to 2016 in Yamaguchi University and partially supported by MEXT KAKENHI Grant-in-Aid for Scientific Research on Innovative Areas Number 22109002.

First, I would like to express my deepest gratitude to Professor Atsushi Sanada for supervising me at his laboratory. From his guidance, I learned a lot about technical knowledge and attitude to research. This work would not be completed without his support.

Besides, I would like to express thanks to Professor Hiroshi Kubo and Assistant Professor Tsunayuki Yamamoto for their fruitful discussions and advices.

In addition, I would like to show my gratitude to all members of the applied physics laboratory and the electromagnetic device laboratory for supporting me. I have been able to grow with them.

Finally, I would like to thank my father, mother, and all the family for supporting my university life in nine years.

References

[1] V. G. Veselago, “The electrodynamics of substances with simultaneously negative values of ε and μ,” *Sov. Phys. –Usp.*, vol. 10, no. 4, pp. 509–514, Jan.–Feb. 1968.

[2] J. B. Pendry, A. J. Holden, W. J. Stewart, and I. Youngs, “Extremely low frequency plasmons in metallic mesostructures,” *Phys. Rev. Lett.*, vol. 76, no. 25, pp. 4773–4776, June 1996.

[3] J. B. Pendry, A. J. Holden, D. J. Robbins, and W. J. Stewart, “Low frequency plasmons in thin-wire structures,” *J. Phys. Condens. Matter*, vol. 10, no. 22, pp. 4785–4809, Mar. 1998.

[4] J. B. Pendry, A. J. Holden, D. J. Robbins, and W. J. Stewart “Magnetism from conductors and enhanced nonlinear phenomena,” *IEEE Trans. Microw. Theory Techn.*, vol. MTT–47, no. 11, pp. 2075–2084, Nov. 1999.

[5] J. B. Pendry, “Negative refraction makes a perfect lens,” *Phys. Rev. Lett.*, vol. 85, no. 18, pp. 3966–3969, Oct. 2000.

[6] D. R. Smith, W. J. Padilla, D. C. Vier, S. C. Nemat-Nasser, and S. Schultz, “Composite medium with simultaneously negative permeability and permittivity,” *Phys. Rev. Lett.*, vol. 84, no. 18, pp. 4184–4187, May 2000.

[7] A. Alù, A. Salandrino, and N. Engheta, “Negative effective permeability and left-handed materials at optical frequencies,” *Opt. Express*, vol. 14, no. 4, pp. 1557–1567, Feb. 2006.

[8] C. Caloz and T. Itoh, “Application of the transmission line theory of left-handed (LH) materials to the realization of a microstrip LH transmission line,” *IEEE AP-S Int. Symp. Dig.*, vol. 2, pp. 412–415, June 2002.

[9] A. A. Oliner, “A periodic-structure negative-refractive-index medium without resonant elements,” *IEEE AP-S/URSI Int. Symp. Dig.*, p. 41, June 2002.

[10] G. V. Eleftheriades, A. K. Iyer, P. C. Kremer, “Planar negative refractive index media using periodically *L–C* loaded transmission lines,” *IEEE Trans. Microw. Theory Techn.*, vol. MTT–50, no. 12, pp. 2702–2712, Dec. 2002.

[11] A. A. Oliner, “A planar negative-refractive-index medium without resonant elements,” *2003 IEEE MTT–S Int. Microwave Symp. Dig.*, pp. 191–194, June 2003.

[12] A. Grbic and G. V. Eleftheriades, “Experimental verification of backward-wave radiation from a negative refractive index material,” *J. Appl. Phys.*, vol. 92, no. 10, pp. 5930–5935, Nov. 2002.

[13] C. Caloz and T. Itoh, “Novel microwave devices and structures based on the transmission line approach of meta-materials,” *2003 IEEE MTT–S Int. Microwave Symp. Dig.*, pp. 195–198, June 2003.

[14] C. Caloz, A. Sanada, L. Liu, and T. Itoh, “A broadband left-handed (LH) coupled-line backward coupler with arbitrary coupling level,” *2003 IEEE MTT–S Int. Microwave Symp. Dig.*, pp. 317–320, June 2003.

[15] A. Sanada, C. Caloz, and T. Itoh, “Novel zeroth-order resonance in composite right/left-handed transmission line resonator,” *2003 Asia–Pacific Microwave Conf. Proc.*, pp. 1588–1591, Nov. 2003.

[16] A. Sanada, C. Caloz, and T. Itoh, “2D distributed meta-structures with negative refractive properties,” *2003 IEEE AP-S Int. Symp.*, vol. 1, p. 4.10, June 2003.

[17] C. Caloz and T. Itoh, “Positive/Negative refractive index anisotropic 2-D metamaterials,” *IEEE Microwave Wireless Comp. Lett.*, vol. 13, no. 12, pp.

547–549, Dec. 2003.

[18] A. Gbric and G. V. Eleftheriades, “Dispersion analysis of a microstrip based negative refractive index periodic structure,” *IEEE Microwave Wireless Comp. Lett.*, vol. 13, no. 4, pp. 155–157, Apr. 2003.

[19] A. Sanada, C. Caloz, and T. Itoh, “Characteristics of the composite right/left-handed transmission lines,” *IEEE Microwave Wireless Comp. Lett.*, vol. 14, no. 2, pp. 68–70, Feb. 2004.

[20] A. Sanada, C. Caloz, and T. Itoh, “Planar distributed structures with negative refractive index,” *IEEE Trans. Microw. Theory Techn.*, vol. MTT–52, no. 4, pp. 1252–1263, Apr. 2004.

[21] C. Caloz and T. Itoh, “Transmission line approach of left-handed (LH) materials and microstrip implementation of an artificial LH transmission line,” *IEEE Trans. Antennas Propagat.* , vol. 52, no. 5, pp. 1159–1166, May 2004.

[22] T. J. Yen, W. J. Padilla, N. Fang, D. C. Vier, D. R. Smith, J. B. Pendry, D. N. Basov, and X. Zhang, “Terahertz magnetic response from artificial materials,” *Science*, vol. 303, no. 5663, pp. 1494–1496, Mar. 2004.

[23] G. Dolling, M. Wegener, C. M. Soukoulis, and S. Linden, “Negative-index metamaterial at 780nm wavelength,” *Opt. Lett.*, vol. 32, no. 1, pp. 53–55, Jan. 2007.

[24] A. Grbic and G. Eleftheriades, “An isotropic three-dimensional negative-refractive-index transmission-line metamaterial,” *J. Appl. Phys.*, vol. 98, no. 4, pp. 043106–1–043106–5, Aug. 2005.

[25] W. J. R. Hoefer, P. P. M. So, D. Thompson, and M. Tenrzeris, “Topology and design of wide-band 3D metamaterials made of periodically loaded transmission

line arrays," *2005 IEEE MTT–S Int. Microwave Symp. Dig.*, pp. 12–17, June 2005.

[26] H. Toyao, E. Hankui, H. Kobayashi, and T. Ando, "Electromagnetic noise suppression technology using metamaterial – Its practical implementation," *NEC Technical Journal*, vol. 8, no. 2, pp. 74–77, Apr. 2014.

[27] J. B. Pendry, D. Schurig, and D. R. Smith, "Controlling electromagnetic fields," *Science*, vol. 312, no. 5781, pp.1780–1782, June 2006.

[28] D. Schurig, J. B. Pendry, and D. R. Smith, "Calculation of material properties and ray tracing in transformation media," *Opt. Express*, vol. 14, no. 21, pp. 9794–9804, Oct. 2006.

[29] D. Schurig, J. J. Mock, B. J. Justice, S. A. Cummer, J. B. Pendry, A. F. Starr, and D. R. Smith, "Metamaterial electromagnetic cloak at microwave frequencies," *Science*, vol. 314, no. 5801, pp. 977–980, Nov. 2006.

[30] B. Kanté, D. Germain, and A. de Lustrac, "Experimental demonstration of a nonmagnetic metamaterial cloak at microwave frequencies," *Phys. Rev. B.*, vol. 80, no. 20, pp. 201104–1–201104–4, Nov. 2009.

[31] J. Li and J. B. Pendry, "Hiding under the carpet: A new strategy for cloaking," *Phys. Rev. Lett.*, vol. 101, no. 20, pp. 203901–1–203901–4, Nov. 2008.

[32] J. Valentine, J. Li, T. Zentgraf, G. Bartal, and X. Zhang, "An optical cloak made of dielectrics," *Nature Materials*, vol. 8, pp.568–571, Apr. 2009.

[33] R. Liu, C. Ji, J. J. Mock, J. Y. Chin, T. J. Cui, and D. R. Smith, "Broadband ground–plane cloak," *Science*, vol. 323, no. 5912, pp. 366–369, Jan. 2009.

[34] J. H. Lee, J. Blair, V. A. Tamma, Q. Wu, S. J. Rhee, C. J. Summers, and W. Park, "Direct visualization of optical frequency invisibility cloak based on silicon

nanorod array," *Opt. Express*, vol. 17, no. 15, pp. 12922–12928, July 2009.

[35] L. H. Gabrielli, J. Cardenas, C. B. Poitras, and M. Lipson, "Silicon nanostructure cloak operating at optical frequencies," *Nature Photonics*, vol. 3, pp. 461–463, Aug. 2009.

[36] T. Ergin, N. Stenger, P. Brenner, J. B. Pendry, and M. Wegener, "Three–dimensional invisibility cloak at optical wavelengths," *Science*, vol. 328, no. 5976, pp. 337–339, Apr. 2010.

[37] H. F. Ma, and T. J. Cui, "Three–dimensional broadband ground–plane cloak made of metamaterials," *Nature Comm*, vol. 1, pp. 21, Feb. 2011.

[38] D. Shin, Y. Urzhumov, Y. Jung, G. Kang, S. Baek, M. Choi, H. Park, K. Kim, and D. R. Smith, "Broadband electromagnetic cloaking with smart metamaterials," *Nature Comm*, vol. 3, pp. 1213, Nov. 2012.

[39] P. Alitalo, O. Luukkonen, L. Jylhä, J. Venermo, and S. Tretyakov, "Transmission–line networks cloaking objects from electromagnetic fields," *IEEE Trans. Antennas Propagat*., vol. 56, no. 2, pp. 416–424, Feb. 2008.

[40] P. Alitalo and S. Tretyakov, "Broadband microwave cloaking with periodic networks of transmission lines," *Proc. of Metamaterials 2008*, pp. 392–394, Sep. 2008.

[41] P. Alitalo, F. Bongard, J–F. Zürcher, J. Mosig, and S. Tretyakov, "Experimental verification of broadband cloaking using a volumetric cloak composed of periodically stacked cylindrical transmission–line networks," *Appl. Phys. Lett.*, vol. 94, no. 1, pp. 014103–1–014103–3, Jan. 2009.

[42] P. Alitalo, F. Bongard, J–F. Zürcher, J. Mosig, and S. Tretyakov, "Broadband electromagnetic cloaking of long cylindrical objects," *Phys. Rev. Lett.*, vol. 103,

no. 10, pp. 103905–1–103905–4, Sep. 2009.

[43] X. Liu, C. Li, K. Yao, X. Meng, W. Feng, B. Wu, and F. Li, "Experimental verification of broadband invisibility using a cloak based on inductor–capacitor networks," *Appl. Phys. Lett.*, vol. 95, no. 19, pp. 191107–1–191107–3, Nov. 2009.

[44] M. Zedler and G. V. Eleftheriades, "2D transformation optics using anisotropic transmission–line metamaterials," *2010 IEEE MTT–S Int. Microwave Symp. Dig.*, May 2010, pp. 33–36.

[45] A. Alù, "Mantle cloak: Invisibility induced by a surface," *Phys. Rev. B.*, vol. 80, no. 24, pp. 245115–1–245115–5, Oct. 2009.

[46] Y. R. Padooru, A. B. Yakovlev, P–Y. Chen, and A. Alù, "Analytical modeling of conformal mantle cloaks for cylindrical objects using sub–wavelength printed and slotted arrays," *Appl. Phys. Lett.*, vol. 112, no. 3, pp. 034907–1–034907–13, Aug. 2012.

[47] M. Selvanayagam and G. Eleftheriades, "An active electromagnetic cloak based on the equivalence principle," *IEEE Antennas and Microwave Wireless propag. Lett.*, vol. 11, pp. 1226–1229, Oct. 2012.

[48] M. Selvanayagam and G. Eleftheriades, "Discontinuous electromagnetic fields using orthogonal electric and magnetic currents for wavefront manipulation," *Opt. Express*, vol. 21, no. 12, pp. 14409–14429, June 2013.

[49] M. Selvanayagam and G. Eleftheriades, "Experimental demonstration of active electromagnetic cloaking," *Phys. Rev. X*, vol. 3, no. 4, pp. 041011–1–041011–13, June 2013.

[50] R. S. Schofield, J. C. Soric, D. Rainwater, A. Kerkhoff, and A. Alù, "Scattering suppression and wideband tenability of a flexible mantle cloak for finite–length

conducting rods," *New J. Phys.*, vol. 16, no. 6, pp. 063063–1–063063–18, June 2014.

[51] U. Leonhardt, "Optical conformal mapping," *Science*, vol. 312, no. 5781, pp.1777–1780, June 2006.

[52] M. G. Silveirinha, A. Alù, and N. Engheta, "Parallel–plate metamaterials for cloaking structures," *Phys. Rev. E*, vol. 75, no. 3, pp. 036603–1–036603–16, Mar. 2007.

[53] B. Edwards, A. Alù, M. G. Silveirinha, and N. Engheta, "Experimental verification of plasmonic cloaking at microwave frequencies with metamaterials," *Phys. Rev. Lett.*, vol. 103, no. 15, pp. 153901–1–153901–4, Oct. 2009.

[54] R. Schittny, M. Kadie, T. Biickmann, and M. Wegener, "Invisibility cloaking in a diffusive light scattering medium," *Science*, vol. 345, no. 6195, pp. 427–429, July 2014.

[55] X. Ni, Z. J. Wong, M. Mrejen, and Y. Wang, and X. Zhang, "An ultrathin invisibility skin cloak for visible light," *Science*, vol. 349, no. 6254, pp. 1310–1314, Sep. 2015.

[56] F. Kong, B. I. Wu, J. A. Kong, J. Huangfu, S. Xi, and H. Chen, "Planar focusing antenna design by using coordinate transformation technology," *Appl. Phys. Lett.*, vol. 91, no. 25, pp. 253509–1–253509–3, Nov. 2007.

[57] Y. Lai, J. Ng, H. Y. Chen, D. Z. Han, J. J. Xiao, Z. Q. Zhang, and C. T. Chan, "Illusion optics: The optical transformation of an object into another object," *Phys. Rev. Lett.*, vol. 102, no. 25, pp. 253902–1–253902–4, June 2009.

[58] W. X. Jiang, H. F. Ma, Q. Cheng, and T. J. Cui, "Illusion media: Generating virtual objects using realizable metamaterials," *Appl. Phys. Lett.*, vol. 96, no. 12,

pp. 121910–1–121910–3, Mar. 2010.

[59] W. Tang, C. Argyropoulos, E. Kallos, W. Song, and Y. Hao, “Discrete coordinate transformation for designing all-dielectric flat antennas,” *IEEE Trans. Antennas Propagat.*, vol. 58, no. 12, pp. 3795–3804, Dec. 2010.

[60] R. Yang, W. Tang, Y. Hao, and I. Youngs, “A coordinate transformation-based broadband flat lens via microstrip array,” *IEEE Antennas and Microwave Wireless propag. Lett.*, vol. 10, pp. 99–102, Jan. 2011.

[61] W. X. Jiang and T. J. Cui, “Radar illusion via metamaterials,” *Phys. Rev. E.*, vol. 83, no. 2, pp. 026601–1–026601–5, Feb. 2011.

[62] Y. Feng, S. Xiong, X. Xu, B. Zhu, J. Zhao, and T. Jiang, “Dielectric multilayers for antenna and cloaking devices designed from transformation electromagnetics,” *Proc. 2013 Int. Symp. Electromagnetic Theory*, pp. 872–875, May 2013.

[63] L. Liang and S. V. Hum, “Realizing a flat UWB 2-D reflector designed using transformation optics,” *IEEE Trans. Antennas Propagat.*, vol. 62, no. 5, pp. 2481–2487, May 2014.

[64] G. Kron, “Equivalent circuit of the field equations of Maxwell–I,” *Proc. IRE*, vol. 32, no. 5, pp. 289–299, May 1944.

[65] P. B. Johns and R. L. Beurle, “Numerical solution of 2–dimensional scattering problems using a transmission–line matrix,” *Proc. Inst. Elec. Eng.*, vol 118, no. 9, pp. 1203–1208, Sep. 1971.

[66] W. J. R. Hoefer, “The transmission–line matrix method–theory and applications,” *IEEE Trans. Microw. Theory Techn.*, vol. MTT–33, no. 10, pp. 882–893, Oct. 1985.

[67] P. B. Johns, “A symmetrical condensed node for the TLM method,” *IEEE Trans.*

Microw. Theory Techn., vol. MTT–35, no. 4, pp. 370–377, Apr. 1987.

[68] C. Christopoulos, *The Transmission–Line Modeling Method: TLM*. New York, NY, USA: IEEE, 1995.

[69] A. Sanada and T. Nagayama, "Transmission line approach for transformation electromagnetics," *Proc. 2013 Int. Symp. Electromagnetic Theory*, pp. 336–337, May 2013.

[70] T. Nagayama and A. Sanada, "Physical equivalent circuit model for 2D full–tensor anisotropic metamaterials," *2013 IEEE MTT–S Int. Microwave Symp. Dig.*, pp. 1–3, June 2013.

[71] T. Nagayama and A. Sanada, "Specular reflection from a sinusoidal periodic boundary by a carpet cloak of invisibility," *2013 Asia–Pacific Microwave Conf. Proc.*, pp. 1209–1211, Nov. 2013.

[72] A. Sanada and T. Nagayama, "Transmission line approach to 2D full–tensor anisotropic metamaterials for transformation electromagnetics," *2014 Int. Conf. Electromagnetics Advanced Appl.*, pp. 804–805, Aug. 2014.

[73] A. Sanada and T. Nagayama, "Transmission line metamaterials for transformation electromagnetics," *2014 44th Eur. Microwave Conf.*, pp. 965–967, Oct. 2014.

[74] T. Nagayama and A. Sanada, "Planar distributed full-tensor anisotropic metamaterials for transformation electromagnetics," *IEEE Trans. Microw. Theory Techn.*, vol. MTT–63, no. 12, pp. 3851–3861, Dec. 2015.

List of Publications

Journal Papers

[1] T. Nagayama and A. Sanada, “Planar distributed full-tensor anisotropic metamaterials for transformation electromagnetics,” *IEEE Trans. Microw. Theory Techn.*, vol. MTT–63, no. 12, pp. 3851–3861, Dec. 2015.

International Conference Proceedings

[1] A. Sanada and T. Nagayama, “Transmission line approach for transformation electromagnetics,” *Proc. 2013 Int. Symp. Electromagnetic Theory*, pp. 336–337, May 2013.

[2] T. Nagayama and A. Sanada, “Physical equivalent circuit model for 2D full–tensor anisotropic metamaterials,” *2013 IEEE MTT–S Int. Microwave Symp. Dig.*, pp. 1–3, June 2013.

[3] T. Nagayama and A. Sanada, “Specular reflection from a sinusoidal periodic boundary by a carpet cloak of invisibility,” *2013 Asia–Pacific Microwave Conf. Proc.*, pp. 1209–1211, Nov. 2013.

[4] A. Sanada and T. Nagayama, “Transmission line approach to 2D full–tensor anisotropic metamaterials for transformation electromagnetics,” *Proc. 2014 Int. Conf. Electromagnetics Advanced Appl.*, pp. 804–805, Aug. 2014.

[5] A. Sanada and T. Nagayama, “Transmission line metamaterials for transformation electromagnetics,” *Proc. 44th Eur. Microwave Conf.*, pp. 965–967, Oct. 2014.

Presentations

[1] T. Nagayama, A. Sanada, T. Yamamoto, H. Kubo, and T. Kodera, “On equivalent circuit models for 2D full-tensor anisotropic metamaterials,” *Conf. Record 2010 (61th) Chugoku-branch Joint Convention of Inst. of Electrical Information Eng.*, p. 538, Oct. 2010.

[2] T. Nagayama, A. Sanada, T. Yamamoto, and H. Kubo, “On an operation of the invisible cloak,” *Proc. IEICE Gen. Conf. 2011*, p. 117, Mar. 2011.

[3] T. Nagayama, A. Sanada, H. Kubo, and T. Yamamoto, “On calculation method of the equivalent circuit parameters of 2D full-tensor anisotropic metamaterials,” *Conf. Record 2011 (62th) Chugoku-branch Joint Convention of Inst. of Electrical Information Eng.*, p. 382, Oct. 2011.

[4] T. Nagayama, A. Sanada, T. Yamamoto, and H. Kubo, “On coordinate transformations for invisible cloak design,” *Proc. IEICE Gen. Conf. 2012*, p. 123, Mar. 2012.

[5] T. Nagayama, A. Sanada, and H. Kubo, “On design of a carpet cloak of invisibility with equivalent circuit models of 2D full-tensor anisotropic metamaterials,” *Conf. Record 2012 (63th) Chugoku-branch Joint Convention of Inst. of Electrical Information Eng.*, p. 152, Oct. 2012.

[6] T. Nagayama and A. Sanada, “2D transmission line anisotropic metamaterials for transformation electromagnetics,” *Proc. IEICE Society Conf. 2013*, p. 108, Sep. 2013.

[7] T. Nagayama and A. Sanada, “Controlling resonant modes of a 2D resonator by transformation electromagnetics,” *Conf. Record 2013 (64th) Chugoku-branch Joint Convention of Inst. of Electrical Information Eng.*, p. 393, Oct. 2013.

[8] T. Nagayama and A. Sanada, “On 2D transmission line anisotropic metamaterials for transformation electromagnetics,” *IEICE Technical Report*, vol. 113, no. 307, pp. 41–45, Nov. 2013.

[9] T. Nagayama, K. Nobusue, and A. Sanada, “On a 2D coordinate transformation resonator based on transformation electromagnetics,” *Proc. IEICE Society Conf. 2014*, pp. S-32–S-33, Sep. 2014.

[10] T. Nagayama, K. Nobusue, and A. Sanada, “On the relation between resonant modes and boundary conditions of 2D coordinate transformation resonators,” *Conf. Record 2014 (65th) Chugoku-branch Joint Convention of Inst. of Electrical Information Eng.*, p. 343, Oct. 2014.

[11] T. Nagayama and A. Sanada, “On wavelength dependency of 2D transmission line anisotropic metamaterials for transformation electromagnetics,” *Conf. Record 2015 (66th) Chugoku-branch Joint Convention of Inst. of Electrical Information Eng.*, 10-15, Oct. 2015.

Awards

[1] 2010 Encouraging Award, IEEJ Chugoku-branch, Feb. 1, 2011.

[2] 2010 Encouraging Award, IEICE Chugoku-branch, May 20, 2011.

[3] 2013 Paper Presentation Award B, IEEJ Chugoku-branch, Dec. 16, 2013.

[4] 2013 Encouraging Award, IEICE Chugoku-branch, Mar. 7, 2014.

[5] 2013 Young Researcher’s Award, IEICE Society Conf., Mar. 19, 2014.

[6] 2014 Encouraging Award, IEICE Chugoku-branch, Feb. 27, 2015.